

PRECISION SCIENCE WITH EINSTEIN TELESCOPE

CLEANING GLITCHES AND ACCELERATING PARAMETER INFERENCE FOR
THE THIRD GENERATION OF GRAVITATIONAL WAVE DETECTORS

Harsh Narola

ISBN: 978-94-6496-537-7

DOI: <https://doi.org/10.33540/3429>

Printed by: Gildeprint – www.gildeprint.nl

Cover design: Harsh Narola

Copyright: © 2025 Harsh Narola

Nik|hef



Universiteit
Utrecht



This work originates as part of the research program of the Foundation for Fundamental Research on Matter (FOM), and falls as of April 1, 2017 under the responsibility of the Foundation for Nederlandse Wetenschappelijk Onderzoek Instituten (NWO-I), which is part of the Dutch Research Council (NWO).

Precision science with Einstein Telescope

Cleaning glitches and accelerating parameter inference for the third generation
of gravitational wave detectors

Precisiewetenschap met Einstein Telescoop

Het opschonen van storingen en het versnellen van parameterinferentie voor
de derde generatie gravitatiegolfdetectoren
(met een samenvatting in het Nederlands)

Proefschrift

ter verkrijging van de graad van doctor aan de Universiteit Utrecht op gezag van de rector
magnificus, prof. dr. ir. W. Hazeleger, ingevolge het besluit van het college voor promoties in het
openbaar te verdedigen op donderdag 12 februari 2026 des middags te 4.15 uur

door

Harsh Narola

geboren op 24 juli 1998

te Manvilas, India

Promotor:

Prof.dr. C.F.F. Van Den Broeck

Co-promotor:

Dr. A. Samajdar

Assessment Committee:

Prof.dr. S.C.M. Bentvelsen

Prof.dr. J.F.J. van den Brand

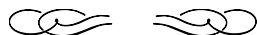
Dr. A. Ghosh

Dr. A. Grelli

Dr. M. Haney

Prof.dr. T. Peitzmann

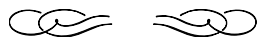
Prof.dr. S.J.G. Vandoren



Contents

Introduction	1
1 From general relativity to gravitational waves	3
1.1 Einstein's field equations	4
1.2 Linearising Einstein's field equations	5
1.2.1 Solutions in vacuum	6
1.2.2 Solutions far away from a source	7
1.3 Gravitational wave detectors	8
1.3.1 Current generation detectors	8
1.3.2 Importance of a <i>network</i> of GW detectors	9
1.3.3 Third generation detectors	10
2 Measuring the source parameters of gravitational wave signals	13
2.1 What counts as a measurement?	13
2.1.1 Bayesian analysis	14
2.1.2 Gravitational wave likelihood	14
2.1.3 Gaussian noise approximation	15
2.2 Waveforms	16
2.3 Nested sampling	17
2.3.1 Limitations of modelled reconstruction	20
3 Reconstructing generic excess of power from the data	23
3.1 Artefacts in Gaussian noise	23
3.2 Transdimensional Sampling Algorithms	24
3.2.1 Morlet-Gabor wavelets	25
3.2.2 Markov chain Monte Carlo	25
3.2.3 GW specific treatment for jumping between dimensions	27
3.3 Limitations and use-cases of the unmodelled reconstruction	29

4	A framework to utilize the triangular geometry of the Einstein Telescope for precision science	31
4.1	The null stream	32
4.2	<code>nijntje</code> : null-stream inspired noise transient elimination framework	33
4.3	Glitch mitigation in the absence of <code>nijntje</code> framework	35
4.4	Results of source parameter measurement: Triangle and 2L comparison	36
4.5	Outlook	38
5	A fast parameter estimation method for the current and next generation detectors	43
5.1	Mode-by-mode relative binning	43
5.1.1	Inclusion of higher order modes and precessing spins	45
5.1.2	Constructing the relative binning grid	47
5.2	Extension of the relative binning method	48
5.2.1	Extension to perform parameter estimation on the overlapping signals	49
5.2.2	Extension to perform strong lensing searches	49
5.3	Validation of the method by performing parameter estimation	52
5.3.1	Validation on simulated events: analysing GW signals in Gaussian noise	52
5.3.2	Validation on real data: analysing GW signals detected by LIGO-Virgo interferometers	52
5.3.3	Validation on the parameter estimation of 3G-era events	55
5.3.4	Validation on the strongly lensed events	58
5.4	Comparison of speed-up and accuracy	62
5.5	Conclusion and outlook	63
6	Constraints on modified propagation theories of GWs using strong lensing	65
6.1	Gravitational lensing and distance measurements	65
6.2	Modified propagation theories	67
6.3	Strongly lensed signals: A probe complementary to the binary neutron star signals	68
6.4	Measurements of model parameters	69
6.5	Results and conclusions	72
	Public summary	75
	Openbare samenvatting	77
	Curriculum vitae	81
	Acknowledgments	83
	Bibliography	84



List of Figures

1.1	A simplified schema for the L-shaped gravitational wave detector.	9
1.2	The antenna pattern functions of the Virgo detector	10
1.3	A simple layout of the triangular design of the Einstein Telescope.	11
2.1	The probability distribution of the prior, likelihood, and posterior	14
2.2	Sixteen seconds of whitened data segment of LIGO-Livingston detector	15
2.3	Gravitational wave waveforms in time domain	16
2.4	Progression of the nested sampling algorithm	18
3.1	The binary neutron star signal GW170817 and the glitch overlapping with it	23
3.2	A binary black hole signal and blip glitch side-by-side	24
3.3	Morlet-Gabor wavelet in time (left) and frequency (right) domain	25
3.4	A Markov chain progressing in the parameter space of $\vec{\theta}$	26
4.1	The formation of an inherent null stream in the Einstein Telescope	33
4.2	The workflow of the <code>nijntje</code> framework	34
4.3	Reconstructed glitch timeseries and its mismatch with the true glitch timeseries	36
4.4	Measurements of the distance, sky location, and total mass	38
4.5	Parameter recovery for different time separation between the glitch and the gravitational wave signal	39
5.1	Ratios of the proposal and fiducial waveform polarisations	45
5.2	A schema of two gravitational wave signals overlapping	48
5.3	A gravitational wave signal being strongly lensed and producing two images	50
5.4	Percentile-percentile plot to test the robustness of the parameter estimation method	54
5.5	Parameter estimation results for the signal GW190412	55
5.6	Parameter estimation results for the signal GW190814	56
5.7	Jensen-Shannon divergence values for the entire set	57
5.8	Simulated signal in the Einstein Telescope	59
5.9	Joint parameter estimation on two overlapping gravitational wave signals	60

5.10	Analysis of the strong lensing candidate GW191103–GW191105	61
5.11	Speed-up achieved by relative binning approximation	62
6.1	The effect on the time domain GW signal in each of the modified propagation models	67
6.2	Imprint on the observable quantity (Δ) as a function of source redshift (x-axis) and scale of deviation (y-axis)	69
6.3	Bounds on the model parameters for the three models	72



List of Tables

4.1	Impact of glitches on the LIGO-Virgo signals in comparison to the anticipated 3G signals.	32
4.2	Comparison ET- Δ and ET-2L configuration in context of glitch mitigation	40
5.1	Parameters and corresponding priors used to simulate individual GW signals and the pairs of lensed GW signals.	53
5.2	Table of simulated events analysed using relative binning method	58
6.1	Deviation parameter(s) for each theory and the corresponding prior probability distributions used in our analyses. The ranges of the prior are centered around the general relativistic value of the parameter and are chosen following the previous studies on modified propagation [1-3].	68



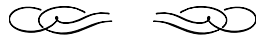
Preface

It may never cease to amaze one that we can now precisely measure a change in distance that is about 10,000 times smaller than the size of a proton. Such a technological feat was achieved in the quest to detect the gravitational waves, a prediction of Einstein's theory of relativity, which he believed to be too weak to be detectable. He may not have minded being corrected in 2015, about a century years after the theory of relativity was published, when a network of two Laser Interferometric Gravitational wave Observatories (LIGO) detected a gravitational wave signal.

Since the first detection in 2015, the network of two LIGO and Virgo detectors has detected about 300 gravitational wave signals, leading to several breakthroughs in fundamental physics and astronomy. Upgrades to the current generation (or second-generation) of detectors, the addition of new detectors such as LIGO-India and KAGRA in Japan, make the future even more promising. Going beyond the second-generation detectors, the third generation of gravitational wave detectors, such as the Einstein Telescope, Cosmic Explorer, and the space-based observatory LISA (Laser Interferometric Space Antenna), are anticipated to usher in an era of precision science measurements. A significant effort is invested in developing tools which can extract physics-related insights from the gravitational wave data. To make the best use of the data collected by the next-generation detectors, a next generation of data analysis tools is also required. With this thesis, we attempt to take a step in that direction.

This thesis is divided into two parts. The first part (chapters 1-3) delves into the pedagogy of gravitational waves. Here, I also lay down the foundation of the tools which are used in the second part of the thesis. The second part (chapters 4-6) contains the published results. Specifically, chapter 4 presents the `nijntje` – (null stream-based noise transient elimination) – framework. The framework can quickly and reliably remove a glitch that may be overlapping with a gravitational wave signal. Chapter 5 presents a fast method to infer the source properties of the gravitational wave signals. Chapter 6 contains simulations to demonstrate how we can use a strongly lensed gravitational wave signal to test a class of beyond general relativistic theories.

Chapter 1



From general relativity to gravitational waves

It is intuitive to think that if this thesis is dropped from the top of a tall building and if the earth's gravity is the only force acting on it, it will travel in a straight line. This trajectory can be determined using Newton's laws of motion [4]. The trajectory is also unique in the sense that it traces the shortest path between the start and end points in a flat space such as the one we are in (i.e. where the gravity is weak). The notion of straight lines in flat spaces can be generalized using geodesics, which represents the extreme path between the two points. For example, the geodesic between any two points on a spherical surface will trace the great circle passing through the two points. When travelling along the great circle from a fixed start and end point, we can take two different paths. One represents the shortest path and the other represents the longest path. In that sense, a geodesic represents the extreme path between two points.

Geodesics

In practice, the shortest path between two points in curved space is obtained by solving the geodesic equation [5],

$$\frac{d^2 x^\mu}{d\tau^2} + \Gamma_{\alpha\beta}^\mu \frac{dx^\alpha}{d\tau} \frac{dx^\beta}{d\tau} = 0, \quad (1.1)$$

where $\Gamma_{\alpha\beta}^\mu$ are called the Christoffel symbols of the second kind, and τ is the scalar parameter of motion also known as proper time. The indices μ, α, β vary from 0 to 3. If an index repeats in the same term of a tensor equation, it is summed over. This is known as Einstein's summation convention. For example, indices α and β are summed over since they repeat on the same term. Index μ also repeats but not in the same term so it is not summed over.

Intuitively, $\Gamma_{\alpha\beta}^\mu$ encodes the notion of force (e.g. gravity) of the Newtonian dynamics¹. For example, when an inertial frame of an object is described using the Cartesian coordinate system, $\Gamma_{\alpha\beta}^\mu$

¹Some accounts [6] hint that Newton initially struggled to settle on the word force, considering alternatives such as power, efficacy, vigour, strength, or virtue. However, the nuance may be lost in translation from Latin to English.

will be zero everywhere. Therefore, Eq. (1.1) reduces to Newton's second law of motion in the absence of any external force, $\ddot{x} = 0$.

1.1 Einstein's field equations

While Newton's theory of gravity attempts to quantify the gravitational force exerted by one body onto another, the explanation of what causes such a force was left to future work. General relativity refines the notion of gravitational force by establishing it as an effect caused by a massive object by curving the space around it [7]. In the form of Einstein's field equations, general relativity relates the distribution of matter to the curvature of the space-time continuum (also referred to as spacetime),

$$G_{\mu\nu} = 8\pi T_{\mu\nu} \quad (1.2)$$

where the Einstein tensor $G_{\mu\nu}$ encodes the information about the curvature. The density and flow of matter and energy are encoded in the stress-energy tensor $T_{\mu\nu}$. We use geometrised units, therefore the speed of light and universal gravitational constant in Eq. (1.2) are set to unity. Einstein's field equations form a set of coupled partial differential equations for the metric tensor $g_{\mu\nu}$, an unknown obtained by solving the equations for a given distribution of mass and energy density. Intuitively, the metric tensor introduces the notion of distance and angles on a surface with arbitrary curvature.

An infinitesimal line element ds can be given by $ds^2 = g_{\mu\nu}dx^\mu dx^\nu$. In the absence of any mass and energy density (in vacuum), it can be shown that the space is flat. The metric tensor and the infinitesimal line element for the flat space are

$$g_{\mu\nu} \equiv \eta_{\mu\nu} = \text{diag}(-1, 1, 1, 1), \quad (1.3)$$

$$ds^2 = \eta_{\mu\nu}dx^\mu dx^\nu = -dt^2 + dx^2 + dy^2 + dz^2. \quad (1.4)$$

The metric tensor for the flat space is also known as the Minkowski metric. There are other possible solutions to the field equations in vacuum, which will become clear later. Let us now turn to how the $g_{\mu\nu}$ is encoded in the field equations.

The Christoffel symbols, Riemann tensor, and Ricci tensor

Let us first revisit the Christoffel symbols $\Gamma_{\nu\mu}^\rho$. They are defined as:

$$\Gamma_{\nu\mu}^\rho = \frac{1}{2}g^{\rho\sigma} (\partial_\nu g_{\mu\sigma} + \partial_\mu g_{\nu\sigma} - \partial_\sigma g_{\nu\mu}). \quad (1.5)$$

They are expressed in terms of partial derivatives of metric tensor and they track how vectors change under parallel transport. Christoffel symbols are used to derive the Riemann tensor $R^\rho_{\mu\lambda\nu}$,

$$R^\rho_{\mu\lambda\nu} = \partial_\lambda \Gamma_{\nu\mu}^\rho - \partial_\nu \Gamma_{\lambda\mu}^\rho + \Gamma_{\lambda\sigma}^\rho \Gamma_{\nu\mu}^\sigma - \Gamma_{\nu\sigma}^\rho \Gamma_{\lambda\mu}^\sigma, \quad (1.6)$$

which tracks how tensors change when transported on a closed path, to determine the curvature of the surface. For a flat surface they do not change so the curvature is zero. Next, we define the Ricci tensor $R_{\mu\nu}$ which is the contraction of the Riemann tensor,

$$R_{\mu\nu} \equiv R^\lambda_{\mu\lambda\nu}. \quad (1.7)$$

The raising or lowering of an index is done using the metric tensor, i.e., $R^\rho_{\mu\lambda\nu} = g^{\rho\alpha} R_{\alpha\mu\lambda\nu}$. Next, we define the Ricci scalar (R);

$$R \equiv g^{\mu\nu} R_{\mu\nu}. \quad (1.8)$$

Finally, we can define the Einstein tensor using the Ricci tensor, the Ricci scalar, and the metric tensor:

$$G_{\mu\nu} \equiv R_{\mu\nu} - \frac{1}{2} g_{\mu\nu} R. \quad (1.9)$$

The Einstein's field equations are connected to the metric tensor in this manner.

Despite the apparent simplicity of Einstein's field equations, there are only a few cases where one can obtain an exact solution, e.g., vacuum solutions, Schwarzschild metric (also known as the non-spinning black holes), Kerr metric (also known as the spinning black holes).

1.2 Linearising Einstein's field equations

This section contains a discussion on linearising Einstein's field equations and their solutions. Specifically, I discuss the solutions in vacuum and far away from the source. I follow the treatment from commonly used textbooks on general relativity and gravitational waves [5, 8].

For simplicity, let us first attempt to solve for the metric tensor when gravity is weak. We expand $g_{\mu\nu}$ as a sum of flat spacetime metric and linear perturbation tensor $h_{\mu\nu}$ for some coordinate system, i.e.,

$$g_{\mu\nu} = \eta_{\mu\nu} + h_{\mu\nu}, \text{ for } |h_{\mu\nu}| \ll 1, \quad (1.10)$$

where $\eta_{\mu\nu}$ is the metric in the flat spacetime also known as the Minkowski metric

$$\eta_{\mu\nu} = \text{diag}(-1, 1, 1, 1). \quad (1.11)$$

Choosing a coordinate system to demand $|h_{\mu\nu}| \ll 1$ breaks the coordinate invariance of the theory, we address this issue later. Using the linearised metric of Eq. (1.10), we linearise Eqs. (1.9)- (1.5). Starting from the last equation, we linearise the Christoffel symbols,

$$\Gamma_{\mu\nu}^\rho = \frac{1}{2} (\partial_\mu h_\nu^\rho + \partial_\nu h_\mu^\rho - \partial^\rho h_{\mu\nu}) + \mathcal{O}(h^2), \quad (1.12)$$

then linearise the Riemann tensor,

$$R^\lambda_{\rho\mu\nu} = \frac{1}{2} (\partial_{\rho\mu}^2 h_\nu^\lambda - \partial_\rho \partial_\nu h_\mu^\lambda + \partial^\lambda \partial_\nu h_{\rho\mu} - \partial^\lambda \partial_\mu h_{\rho\nu}) + \mathcal{O}(h^2), \quad (1.13)$$

linearise the Ricci tensor and the Ricci scalar,

$$R_{\mu\nu} = \frac{1}{2} (\partial_\nu \partial_\lambda h_\mu^\lambda + \partial_\mu \partial_\lambda h_\nu^\lambda - \partial^\lambda \partial_\lambda h_{\mu\nu} - \partial_\mu \partial_\nu h_\lambda^\lambda) + \mathcal{O}(h^2), \quad (1.14)$$

$$R = \frac{1}{2} (\partial^\mu \partial^\nu h_{\mu\nu} - \partial^\mu \partial_\mu h_\nu^\nu) + \mathcal{O}(h^2), \quad (1.15)$$

and finally linearise the Einstein tensor,

$$G_{\mu\nu} = \frac{1}{2} (\partial_\lambda \partial_\mu h_\nu^\lambda + \partial_\lambda \partial_\nu h_\mu^\lambda - \partial_\mu \partial_\nu h - \square h_{\mu\nu} - \eta_{\mu\nu} \partial_\rho \partial_\lambda h^{\rho\lambda} + \eta_{\mu\nu} \square h), \quad (1.16)$$

where h is the trace of $h_{\mu\nu}$ and the box (\square) symbol represents $\eta^{\mu\nu}\partial_\mu\partial_\nu$, also known as the d'Alembert operator or box operator. We introduce the trace-reversed $\bar{h}_{\mu\nu} = h_{\mu\nu} - \frac{1}{2}\eta_{\mu\nu}h$ to simplify Eq. (1.16);

$$G_{\mu\nu} = \frac{1}{2} \left(\partial^\lambda \partial_\nu \bar{h}_{\mu\lambda} + \partial^\lambda \partial_\mu \bar{h}_{\nu\lambda} - \square \bar{h}_{\mu\nu} - \eta_{\mu\nu} \partial^\lambda \partial^\rho \bar{h}_{\lambda\rho} \right). \quad (1.17)$$

Since we chose a coordinate system in Eq. (1.10), the invariance of the theory is broken. We can partially restore it by allowing for transformations of the form:

$$x^\mu \rightarrow x'^\mu = x^\mu + \xi^\mu \text{ where } |\partial_\nu \xi^\mu| \lesssim |h_{\mu\nu}|. \quad (1.18)$$

The additional condition ensures that the perturbations remain small. Under the transformations proposed in Eq. (1.18), the trace-reversed metric perturbations transform as

$$\bar{h}_{\mu\nu} \rightarrow \bar{h}'_{\mu\nu} = \bar{h}_{\mu\nu} - (\partial_\mu \xi_\nu + \partial_\nu \xi_\mu - \eta_{\mu\nu} \partial_\sigma \xi^\sigma). \quad (1.19)$$

Such transformations do not change the tensor components so a solution of the linearised field equations remains a solution in every coordinate system obtained under this transformation. Therefore, when choosing a coordinate system, we have the freedom to work with the one that simplifies Eq. (1.17). Specifically, we can always find a ξ^ν for which

$$\partial^\nu \bar{h}'_{\mu\nu} = 0. \quad (1.20)$$

This choice is called the harmonic gauge. The ξ^ν for such a transformation is obtained by solving the following equation:

$$\square \xi_\nu = \partial^\mu \bar{h}_{\mu\nu}, \quad (1.21)$$

using an appropriate Green's function. The harmonic gauge leaves room for additional transformations which satisfy the equation $\square \xi^\nu = 0$. I will explain the consequences later. In harmonic gauge, the linearised field equation (1.17) further simplifies to

$$G_{\mu\nu} = -\frac{1}{2} \square \bar{h}_{\mu\nu} = 8\pi T_{\mu\nu}. \quad (1.22)$$

We dropped the prime mark in writing the above equation.

1.2.1 Solutions in vacuum

Next, we attempt to solve the linearised field equations in vacuum. The stress-energy tensor $T_{\mu\nu}$ is equal to zero in this case. Therefore, Eq. (1.22) reduces to

$$\square \bar{h}_{\mu\nu} = 0. \quad (1.23)$$

Eq. (1.23) is a wave equation as it admits plane-wave solutions,

$$\bar{h}_{\mu\nu} = A_{\mu\nu} \cos(k_\alpha x^\alpha), \quad (1.24)$$

which are the perturbation of a flat spacetime far away from the source or gravitational waves (GWs) in a vacuum. To satisfy the wave equation, $k_\alpha k^\alpha$ should be equal to zero, meaning GWs in vacuum travel at the speed of light. The harmonic gauge ensures that

$$k^\mu A_{\mu\nu} = 0, \quad (1.25)$$

so GWs are transverse, i.e., the polarisations of the waves are perpendicular to the direction of propagation.

Plus and cross polarisations

Let us now count the degrees of freedom of the metric perturbation $\bar{h}_{\mu\nu}$. We start with 16 which is the number of degrees of freedom of a 4×4 tensor. From 16, 6 are restricted due to $\bar{h}_{\mu\nu}$ being symmetric. From the remaining 10, 4 are restricted by harmonic gauge. As mentioned earlier, even after imposing the harmonic gauge, we can allow for the transformation of the form $\square\xi_\mu = 0$. This restricts 4 more degrees of freedom. Therefore, the metric perturbation in transverse-traceless (TT) gauge $\bar{h}_{\mu\nu}^{\text{TT}}$ has 2 degrees of freedom, which are called the plus and cross polarisations,

$$h_{\mu\nu}^{\text{TT}} = \begin{pmatrix} 0 & 0 & 0 & 0 \\ 0 & h_+ & h_\times & 0 \\ 0 & h_\times & -h_+ & 0 \\ 0 & 0 & 0 & 0 \end{pmatrix} \quad (1.26)$$

for a gravitational wave propagating along z -direction. The names follow from the phenomenon that if a gravitational wave passes by a ring of beads in a vacuum, the plus (cross) polarisation will periodically stretch and squeeze the ring in $+$ (\times) shape.

1.2.2 Solutions far away from a source

Moving on from the discussion on the vacuum solutions, we now consider a scenario where the stress-energy tensor is non-zero,

$$\square\bar{h}_{\mu\nu} = -16\pi T_{\mu\nu}. \quad (1.27)$$

Quadrupole radiation

Here, we can draw an analogy from the calculation of electromagnetic radiation from an arbitrary charge distribution at a distance. This calculation is usually done using multipole expansion. Each term in the series obtained from multipole expansion approximates the spatial distribution of the source and represents the contribution to far-field radiation in decreasing order. The first term (also known as the monopole term) in the expansion is simply the total charge. It does not contribute to electromagnetic radiation due to the law of conservation of electric charge. Therefore, the dominant contribution to electromagnetic radiation is due to the second term, also known as the dipole term.

Similarly, before attempting to solve Eq. (1.27), we can argue that the gravitational radiation does not have a contribution from the monopole term due to the law of conservation of mass. Unlike electromagnetic radiation, the lowest-order contribution to gravitational radiation is due to the quadrupole term. The mass dipole term ($\approx \Sigma_i m_i \vec{x}_i$) can be made zero by moving to the centre of the mass frame of the system. The same is not applicable in the case of electromagnetic radiation since charges (unlike mass) can be negative.

Next, we write down the formal solution for Eq. (1.27) using the retarded Green's function;

$$\bar{h}_{ij}^{\text{TT}}(t, \vec{x}) = 4\Lambda_{ijkl} \int d\vec{y} \frac{T^{kl}(t - |\vec{x} - \vec{y}|, \vec{y})}{|\vec{x} - \vec{y}|}. \quad (1.28)$$

here \vec{y} is contained within the source and Λ_{ijkl} is the projection operator to TT gauge. We impose boundary conditions such that there is no incoming radiation. Due to the far-field regime, our distance

to the source (\vec{x}) is much larger than the length scale of the source (d). Expanding the distance $|\vec{x} - \vec{y}|$,

$$|\vec{x} - \vec{y}| = r - \vec{y} \cdot \hat{n} + \mathcal{O}\left(\frac{d^2}{x}\right), \quad (1.29)$$

where \hat{n} is the unit vector along the direction $\vec{x} - \vec{y}$. Approximating the reciprocal term $\frac{1}{|\vec{x} - \vec{y}|} \approx \frac{1}{r}$ and expanding the the stress-energy tensor around $t - r$,

$$\begin{aligned} T^{kl}(t - r + \vec{y} \cdot \hat{n}, \vec{y}) &\approx T^{kl}(t - r, \vec{y}) + (y^a n_a) \partial_0 T^{kl}(t - r, \vec{y}) \\ &+ \frac{1}{2} (y^a n_a) (y^b n_b) \partial_0 \partial_0 T^{kl}(t - r, \vec{y}) + \dots \end{aligned} \quad (1.30)$$

Using Eq. (1.30), the solution in Eq. (1.28) to the leading order can be written down as

$$\bar{h}_{ij}^{\text{TT}}(t, \vec{x}) = \frac{4}{r} \Lambda_{ijkl} \int d\vec{y} T^{kl}(t - r, \vec{y}). \quad (1.31)$$

The momenta T^{kl} are the components of the stress-energy tensors. Using the conservation of stress-energy tensor ($\partial_\nu T^{\mu\nu} = 0$) and the fact that the source is confined in space, we can express Eq. (1.31) in terms of the mass quadrupole moment,

$$\bar{h}_{ij}^{\text{TT}}(t, \vec{x}) = \frac{2}{r} \Lambda_{ijkl} \frac{\partial^2}{\partial t^2} M^{kl}(t - r), \quad (1.32)$$

where $M^{kl} = \int d\vec{y} T^{00} y^k y^l$ is the mass quadrupole moment. It shows the leading order contribution to the far-field gravitational radiation. The mass and linear momentum is conserved only in the case of the linearised theory. A radiating body loses mass and linear momentum. However, the absence of monopole and dipole terms holds more generally. It can be derived in the full non-linear treatment of the field equation [8].

1.3 Gravitational wave detectors

Ground-based GW detectors such as LIGO, Virgo, and KAGRA, work on the principles of interferometry. By observing the constructive and destructive interference of two laser beams, they can measure very small changes in length. The configuration of ground-based detectors is that of a modified Michelson interferometer [9].

1.3.1 Current generation detectors

A schematic diagram of an L-shaped interferometer is shown in Figure 1.1. A laser beam is split into two and travels through two arms of equal length. The light bounces back from the mirror at the end of the arm. The laser travels an equal distance in each arm in the absence of external disturbances, e.g. absence of a gravitational wave. When a gravitational wave passes by, it periodically stretches and squeezes the arms so the light no longer travels the same distance in both arms. By observing the constructive and destructive interference pattern in the light collected by the photodiode, we can measure the strain of the gravitational wave signal. The strain denoted by $h(t)$ is equal to the relative change in arm length denoted by L ,

$$h(t) = \frac{\Delta L}{L}. \quad (1.33)$$

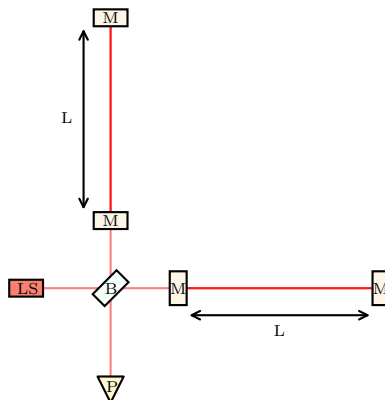


Figure 1.1: Simplified schematic diagram of an L-shaped GW detector. The labels denote the following objects. LS: Source of laser. B: Beam splitter. M: Mirror. P: Photodiode. The arm length is marked by L which is the distance between the input and output mirror in the given arm.

GW detectors are sensitive to the following linear combination of plus and cross polarisations of a GW signal:

$$h(t) = \frac{\Delta L}{L} = F_+ h_+(t) + F_\times h_\times(t). \quad (1.34)$$

Here, F_+ and F_\times are called antenna pattern functions of the detector. They enable the projection of the GW polarisations from the source frame to the detector frame. Unlike conventional electromagnetic telescopes, the GW detectors are not pointed in any particular direction. Their orientation changes only with the Earth's rotation. Their sensitivity around the sky indeed depends on the sky location and the polarisation angle of the gravitational wave. Each F_i is a function of four parameters

$$F_i := F_i(\alpha, \delta, \psi), \quad (1.35)$$

where α and δ denote the right ascension and declination, respectively. The polarisation angle is denoted by ψ . Their sensitivity is periodic over ~ 24 hours. The index i represents the two polarisations. The antenna pattern function for an L-shaped detector (opening angle of 90°) is [10],

$$F_+ = \frac{1}{2} (1 + \cos^2 \delta) \cos 2\alpha \cos 2\psi - \cos \delta \sin 2\alpha \sin 2\psi \quad (1.36)$$

$$F_\times = \frac{1}{2} (1 + \cos^2 \delta) \cos 2\alpha \sin 2\psi + \cos \delta \sin 2\alpha \cos 2\psi. \quad (1.37)$$

1.3.2 Importance of a *network* of GW detectors

Figure 1.2 shows the antenna pattern functions of the Virgo detector [11]. We plot the F_+ and F_\times over the whole sky by varying right ascension from -180° to 180° and declination to -90° to 90° , at the time of arrival of the first gravitational wave signal detected from the merger of two neutron stars also known as GW170817 [12] (signal arrived to Earth on 17th August 2017 hence the naming

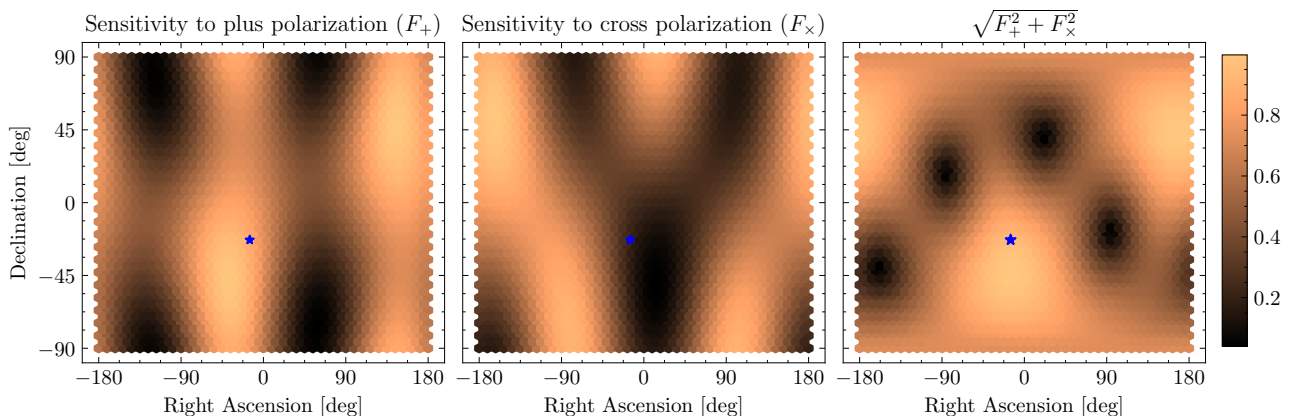


Figure 1.2: Individual and combined antenna pattern functions of the Virgo detector over the whole sky at the time of arrival of binary neutron star signal, GW170817 (blue star). The blue star specifically marks the location of the host galaxy of the binary, NGC 4993, near where the electromagnetic afterglow was found. The dark (bright) colour marks the regions of low (high) sensitivity. The marker shows the median value of the sky-location measurement of GW170817. We note that GW170817 is the closest to Earth and most precisely localised GW source to date (28 deg^2 for 90% confidence interval and 40_{-14}^{+8} Mpc). Such precise measurements are due to all three GW detectors, LIGO-Livingston, LIGO-Hanford, and Virgo, being online at the time of arrival of the signal. Such measurements may not have been possible without a *network* of GW detectors.

convention). We fix the polarisation angle to the median value of its polarisation angle of GW170817 while creating Figure 1.2.

All three GW detectors, LIGO-Livingston, LIGO-Hanford, and Virgo, were online at the time of arrival of GW170817, and indeed the signal was observed in all three of them. Such multi-detector observation led to precise sky location and distance measurement of GW170817. It was localised within a 28 deg^2 area with a 90% confidence interval and 40_{-14}^{+8} Mpc distance, making it the most precisely localised source to date. Such precise localisation allowed the identification of electromagnetic (EM) counterparts, marking this event the first multimessenger (GW+EM) observation in history. This discovery may not have been possible without a *network* of GW detectors. Decommissioning of one or more interferometers could severely harm our ability to make multimessenger discoveries such as this.

1.3.3 Third generation detectors

The two LIGO detectors [9], the Virgo detector [11], the KAGRA detector [13], and the upcoming detector in India [14] are collectively referred to as the current generation (at the time of writing of this thesis) or second generation (2G) detectors. While the current generation of GW detectors has opened a new window onto the Universe, the proposed third-generation (3G) detectors are expected to usher in an era of precision science. These include the Cosmic Explorer [15] and the Einstein Telescope (ET) [16,17]. Design and site-selection studies to maximise the scientific potential of 3G detectors are currently underway.

In particular, Figure 1.3 shows a simple layout of the proposed triangular design of the Einstein Telescope. The Einstein Telescope is a network of three V-shaped detectors with an opening angle of 60° , forming an equilateral triangle. Each detector is composed of a low-frequency and a high-frequency

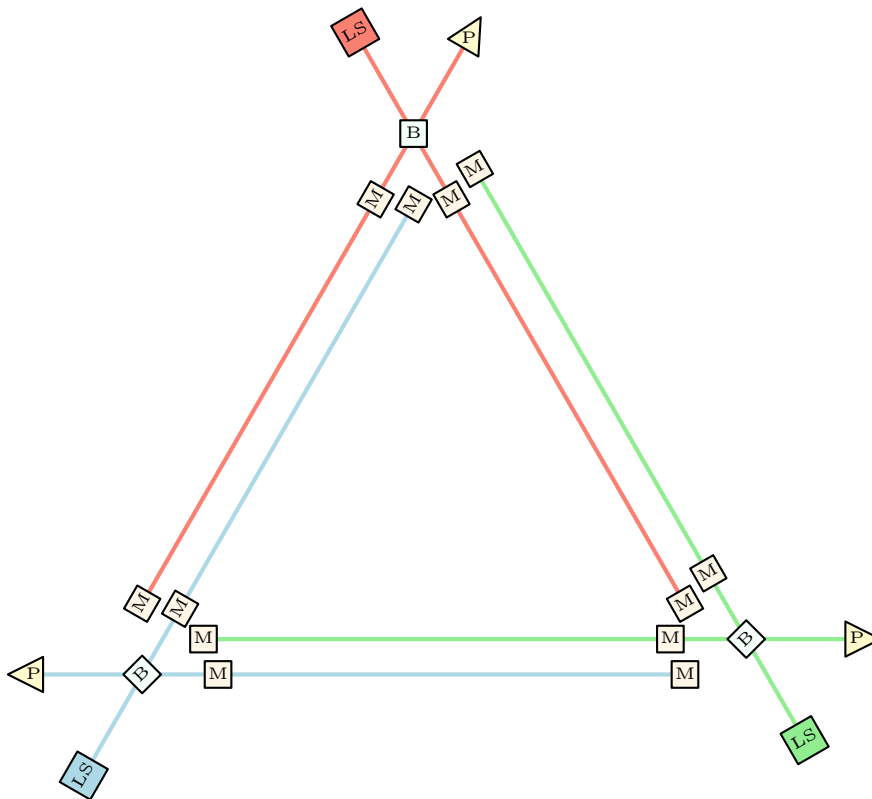


Figure 1.3: A simple layout of the triangular design of the Einstein Telescope. It consists of 3 V-shaped interferometers with an opening angle of 60° , forming an equilateral triangle with an arm length of 10 km. The object notations are the same as those shown in the L-shaped interferometer, namely, M denotes the mirrors, B denotes the beam splitters, LS denotes the laser sources, and P denotes the photodiodes.

interferometer (the “xylophone” setup). The proposed arm length is 10 km, and the infrastructure is expected to be 250 to 300 meters below the ground. The antenna pattern functions for an opening angle of 60° is [18],

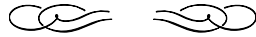
$$\begin{aligned}
 F_+^1 &= -\frac{\sqrt{3}}{4} [(1 + \cos^2 \delta) \sin 2\alpha \cos 2\psi + 2 \cos \delta \cos 2\alpha \sin 2\psi], \\
 F_\times^1 &= +\frac{\sqrt{3}}{4} [(1 + \cos^2 \delta) \sin 2\alpha \sin 2\psi - 2 \cos \delta \cos 2\alpha \cos 2\psi],
 \end{aligned}
 \tag{1.38}$$

where the index 1 arbitrarily denotes any one of the three detectors of the triangle. The antenna pattern functions of the second and the third detector is given by $\alpha \rightarrow \alpha \pm 120^\circ$. Though the individual antenna pattern functions of a V-shaped detector are a factor of $\sqrt{3}/2$ smaller than an L-shaped detector with the same arm-length, the Einstein Telescope with a network of three V-shaped detectors does not have any blind spot in the sky [19]. Moreover, the geometry of the triangle gives rise to an inherent null stream in Einstein Telescope. We discuss more about the null stream and how

we can leverage it for precision science measurements in chapter 4.

At the time of writing this thesis, the proposed sites for the ET include the Euregio Meuse-Rhine (EMR) located near the border of the Netherlands, Belgium, and Germany, the Sardinia island located in the south-west of Italy, and the Lusatia region in Saxony. Alternate proposals for the configuration of ET include two distant L-shaped detectors (Figure 1.1) with 15-kilometre arm-length located in Sardinia and EMR region each [20].

Chapter 2



Measuring the source parameters of gravitational wave signals

Gravitational wave signals emitted by the merger of two compact objects are routinely detected by the current generation of GW detectors. Such a GW signal can typically be modelled using 15 parameters. Eight of them are considered intrinsic parameters; two for the masses and six for the three-dimensional spins of the two objects. The rest of them, e.g. sky location and distance, are considered extrinsic parameters. If one of the compact objects is a neutron star, an additional intrinsic parameter is added to model its tidal deformability. Measurement of these parameters is a key step which enables various physics-related insights from the data, e.g. testing the prediction of general relativity, constraining the neutron star equation of state. Following the well-established method of Bayesian parameter inference [21, 22], I illustrate how the parameters of merging binary black holes and/or neutron stars are measured from a GW signal.

2.1 What counts as a measurement?

Measuring the parameters of a GW source amounts to treating each parameter as a random variable and estimating its probability distribution which is conditioned on the observed data. For the sake of the argument, let's say we are interested in measuring the luminosity distance (D_L) to the source. Before the signal is observed, the measurement cannot be made or we can say that all values of D_L are equally likely or the *prior* probability distribution of the random variable is uniform. After the data is collected i.e. a GW signal is observed, we can update the prior probability distribution using the data to obtain the *posterior* probability distribution. The posterior probability distribution or the *measurement* of the parameter can be thought of as the probability distribution which is conditioned on the observed data.

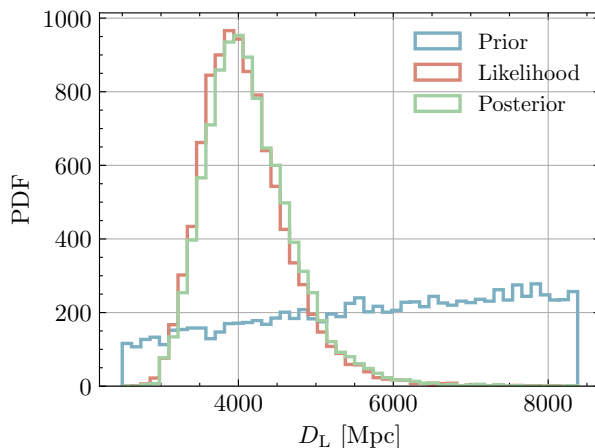


Figure 2.1: An illustration of the probability distribution of the prior (blue), likelihood (red), and posterior (green) of the luminosity distance D_L . Measuring a source parameter amounts to transforming the prior distribution to the posterior distribution using the likelihood of the parameter at the given value. The prior on the luminosity distance is assumed to be uniform in comoving volume therefore its values increase with D_L .

2.1.1 Bayesian analysis

We formalize the problem of converting the prior probability distribution to the posterior probability distribution using the Bayes theorem. We aim to estimate the posterior distribution $p(\vec{\theta}|\vec{d})$ where p denotes the probability distribution function, $\vec{\theta}$ denotes the set of GW source parameters, and \vec{d} denotes the data. Using Bayes' theorem we can invert the conditional probability $p(\vec{\theta}|\vec{d})$ as,

$$p(\vec{\theta}|\vec{d}) = \frac{\pi(\vec{\theta}) p(\vec{d}|\vec{\theta})}{p(\vec{d})}, \quad (2.1)$$

where $\pi(\vec{\theta})$ is the prior probability distribution of $\vec{\theta}$ which is typically assumed to be uniform. The factor $p(\vec{d}|\vec{\theta})$ is the likelihood of observing data given the parameters $\vec{\theta}$. The factor $p(\vec{d})$ can be treated as the normalization factor for the time being. This factor is typically known as the evidence if we use Bayes's theorem to test competing hypotheses. Figure 2.1 shows an illustration of the prior probability distribution (blue) and the posterior probability distribution (red) of the parameter (D_L) where the latter is obtained by updating the prior weights by the weight of likelihood (green) for the corresponding value.

2.1.2 Gravitational wave likelihood

While the Bayesian framework described above is conceptually easy, it is a computationally challenging task to do parameter estimation due to the dimensionality of the space of $\vec{\theta}$ (typically 15 to 17), length of the \vec{d} , and complexity of simulating of GW signal models. Before diving into how we tackle these issues, let us define a few standard quantities used during the computation, starting with the likelihood function $p(\vec{d}|\vec{\theta})$ itself;

$$\ln p(\vec{d}|\vec{\theta}) = -\frac{1}{2} \left\langle \vec{d} - \vec{h}(\vec{\theta}) | \vec{d} - \vec{h}(\vec{\theta}) \right\rangle, \quad (2.2)$$

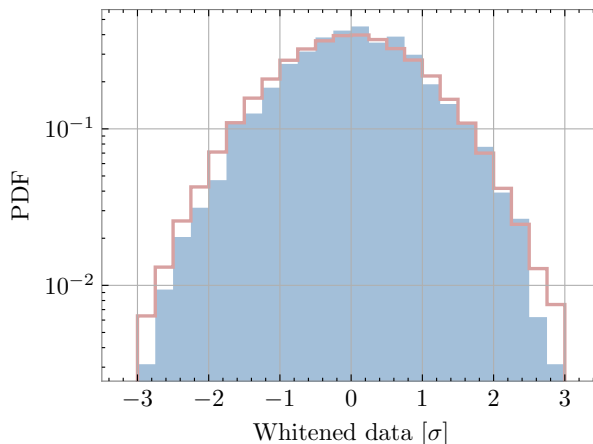


Figure 2.2: To test the Gaussian-stationary nature, we compare the distribution of 16-seconds of whitened data segment of LIGO-Livingston (blue histogram) with the normal distribution (red outline). The PSD is generated using 2048 seconds of data near the segment.

where \vec{h} denotes the GW signal as a function of the source parameters $\vec{\theta}$, in the detector frame. The brackets $\langle . | . \rangle$ denote the noise weighted inner product;

$$\langle \vec{a} | \vec{b} \rangle = \frac{4}{T} \sum_f \frac{\tilde{a}(f) \tilde{b}^*(f)}{S_n(f)}, \quad (2.3)$$

where T is the duration of segment \vec{d} we want to analyse, \tilde{b}^* denotes the complex conjugate of the Fourier transform of time domain vector \vec{b} , and f is the frequency. The factor $S_n(f)$ is the variance of the noise at frequency f , also known as the power spectral density (PSD). The sum is over the evenly distributed discrete frequencies. The lower frequency cutoff for LIGO-Virgo is typically 20 Hz, and the upper frequency cutoff is typically 1024 Hz. The expression for the log likelihood in Eq. (2.2) is for one detector. For a network of detectors, it turns into a sum of log likelihoods over the detectors in the network. We define two more quantities which are used in the latter chapters, the matched filter signal-to-noise ratio (SNR) and the optimal SNR:

$$\rho_{\text{mf}}^2 = \frac{4}{T} \sum_f \frac{\tilde{d}(f) \tilde{h}^*(f)}{S_n(f)} \quad \text{and} \quad \rho_{\text{o}}^2 = \frac{4}{T} \sum_f \frac{\tilde{h}(f) \tilde{h}^*(f)}{S_n(f)}. \quad (2.4)$$

2.1.3 Gaussian noise approximation

The expression of the likelihood function is inspired by the so-called Whittle likelihood which is typically used to analyse Gaussian and stationary time series. While the data \vec{d} cannot be expected to be Gaussian and stationary at all times, for the short stretches of data that we analyse, it can be approximated with a Gaussian distribution with zero mean and known variance, making the Whittle likelihood a suitable choice. The likelihood expression in Eq. (2.2) is simply the product (or sum when operated with natural logarithm on both sides) of Gaussian distributions with zero mean and variance equal to $S_n(f)$ for each frequency. We show a qualitative test of the Gaussian and stationary nature of the data in Figure 2.2. The distribution of the whitened data $\frac{\vec{d}}{\sqrt{S_n}}$ tends to follow the normal

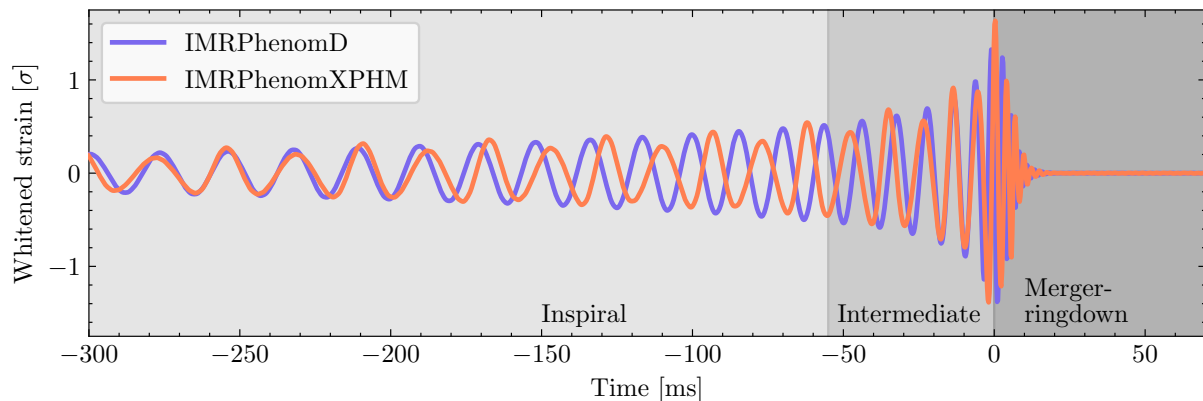


Figure 2.3: The whitened detector frame waveform corresponding to the maximum likelihood parameters of GW190814. We show two waveforms of the phenomenological family, IMRPhenomD (blue) and IMRPhenomXPHM (red). The former only contains the dominant mode and aligned spin description. The latter presents a more complete description, i.e. contribution from dominant and higher-order modes and all three spin components. The shades of grey approximately show different regimes in which different methods are used to compute the phase and amplitude.

distribution. The data segment used to make this plot lies near the GW150914 signal, the first direct detection of a GW signal from the merger of two black holes. We also note that the detectors routinely encounter noise artefacts which make the noise distribution non-Gaussian and/or non-stationary, as will become clear in the next chapter.

2.2 Waveforms

Waveforms are the solutions to Einstein’s field equations. They describe how the spacetime evolves during the coalescence of two compact objects. A solution to the field equation that describes the complete phenomena of coalescence, i.e. inspiral, merger, and ringdown (IMR), cannot be obtained analytically. One typically resorts to numerical relativity simulations (see for a review [23]). Ideally, we would like to have waveforms obtained from the numerical relativity simulation for the entire parameter space of $\vec{\theta}$. However, these simulations are computationally expensive, which makes them unsuitable for parameter inference, where we need to simulate a large number of ($\approx 10^6$ to 10^7) waveforms per analysis. Various methods have been developed over the past decade to address this challenge, which in turn give rise to different waveform families.

In the latter chapter of this thesis, I use the IMRPhenom waveform family. It is a family of phenomenological waveforms that contains a complete description of the coalescence of a compact binary. The phenomenological waveforms are constructed using different ansatzes for phase and amplitude of the waveforms in different regimes (see Figure 2.3). The waveforms are phenomenological in the sense that the parameters appearing in the ansatz are phenomenological in nature [24, 25]. The phenomenological parameters are calibrated against a set of numerical relativity simulations. This approach produces accurate and computationally inexpensive waveforms, suitable for parameter inference.

In the case of binary black holes (BBHs), we typically need 15 parameters describe the phenomena; two for the masses of the two black holes, six for the three dimensional spins for the two black

holes, three for the volume localisation (right ascension, declination, and luminosity distance w.r.t to the detector), zenith angle between line of sight and total angular momentum (also known as the inclination angle), polarisation angle, phase at the time of coalescence, and time of coalescence. If there is a binary neutron star, we need to add a parameter to account for the tidal deformability of the object. The IMRPhenomD waveform of the phenomenological family describes the systems with aligned (or anti-aligned) spins and with the dominant mode contribution [26,27]. The dominant mode here corresponds to the mass quadrupole moment. The multipole expansion of the gravitational wave strain can be decomposed in terms of spherical harmonics h_{lm} as [28]

$$h(t, \iota, \phi; \vec{\theta}) = \sum_{l=2}^{\infty} \sum_{m=-l}^l h_{lm}(t, \vec{\theta}) Y_{lm}^{-2}(\iota, \phi), \quad (2.5)$$

where Y_{lm}^{-2} are the spin-weighted spherical harmonics with weight 2, (ι, ϕ) are two angles describing the direction of the GW radiation in the frame of the source, and $\vec{\theta}$ denote the remaining parameters of the binary system. The mode corresponding to $l = 2$ and $m = 2$ is the dominant mode, also known as the (2, 2) mode. Though the amplitude of the higher order mode is usually suppressed by the dominant mode, they become non-negligible for a specific range of values of inclination angle and mass ratio [29]. A more complete description of the gravitational wave strain is provided by the IMRPhenomXPHM waveform, which describes a system with precessing spins (all three spin components) and with contributions from dominant as well as higher order modes [30]. A comparison of the time domain representation of IMRPhenomD and IMRPhenomXPHM waveforms is shown in Figure 2.3.

2.3 Nested sampling

When performing parameter estimation, we need to explore the likelihood function on large parameter space. For example, if we choose only 10 points along each dimension of the parameter space, we need to perform about 10^{15} to 10^{17} likelihood evaluation where each evaluation takes $\mathcal{O}(10)$ milliseconds. Indeed, 10 points may be too sparse to cover each dimension. Therefore, we rely on various sampling algorithms to efficiently explore a large parameter space. Here, I explain nested sampling, an algorithm routinely used for parameter estimation and also the one used to obtain the majority of the results in the later chapters of this thesis.

The nested sampling algorithm was introduced in 2004 by John Skilling [31] and it was first applied to analyse GW signals by Veitch and Vecchio [32]. The name derives from the fact that the progression of the algorithm relies on *nested* contours of likelihood (Figure 2.4 (left)) and not the individual likelihood values. The algorithm aims to compute the evidence Z ,

$$Z = \int d\vec{\theta} \pi(\vec{\theta}) p(\vec{d}|\vec{\theta}) \quad (2.6)$$

where the integrand on the right-hand side is simply the product of the likelihood and the prior defined in Eq. (2.1), i.e., Z is the normalization constant from $p(\vec{d})$ that equation. The posterior distribution on the model parameters, $p(\vec{\theta}|\vec{d})$, is obtained as a byproduct. In this sense, nested sampling is an algorithm to perform multidimensional integral.

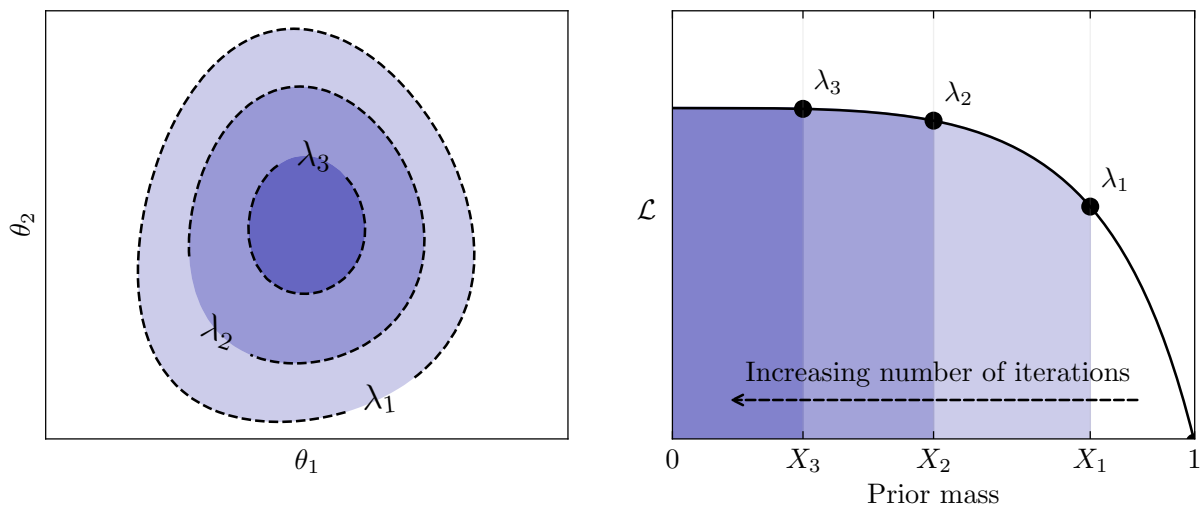


Figure 2.4: *Left*: Constant likelihood surfaces for a two dimensional parameter space $\vec{\theta} = \{\theta_1, \theta_2\}$, illustrating the nested contours. *Right*: Evolution of the prior mass (X) enclosed by the constant likelihood surfaces shown in the left plot.

Typically, one can divide the parameter space of $\Delta\vec{\theta}$ into smaller cubes such that the integrand nearly remains constant over the cube and then sum over the whole space to obtain Z . However, this approach quickly becomes intractable. Here, we instead divide the space into contours created by constant likelihood surfaces (Figure 2.4). For simplicity let us denote the likelihood factor $p(\vec{d}|\vec{\theta})$ by $\mathcal{L}(\vec{\theta})$. Let us define $X(\lambda)$ as,

$$X(\lambda) = \int_{\mathcal{L}(\vec{\theta}) > \lambda} \pi(\vec{\theta}) \, d\vec{\theta}, \quad (2.7)$$

which is the prior mass obtained by integrating $\pi(\vec{\theta})$ over the region of parameter space where $\mathcal{L}(\vec{\theta}) > \lambda$. Since the prior is a normalized probability distribution, its integration over the entire space spanned by $\vec{\theta}$ is 1, therefore the maximum value of X is also 1. As λ increases, X tends to zero as the volume over which prior needs to be integrated grows smaller and smaller (Figure 2.4). Using Eq. (2.7), we can convert the multidimensional integral of Eq. (2.6) into one dimensional integration,

$$Z = \int_0^1 dX \hat{\mathcal{L}}(X), \quad (2.8)$$

where $\hat{\mathcal{L}}$ is the inverse of $X(\lambda)$,

$$\hat{\mathcal{L}}(X(\lambda)) \equiv \lambda.$$

We can approximate the integral in Eq. (2.8) with the Riemann sum to obtain

$$Z \approx \sum_{k=0}^N \left(\frac{\hat{\mathcal{L}}_k + \hat{\mathcal{L}}_{k+1}}{2} \right) \Delta X_k \equiv \sum_{k=0}^N w_k. \quad (2.9)$$

Once we calculate Z , the posterior probability of point $\vec{\theta}_k$ can be computed by

$$p(\vec{\theta}_k|\vec{d}) = \frac{\pi(\vec{\theta}_k)\mathcal{L}(\vec{\theta}_k)}{Z} = \frac{w_k}{\sum_{k=0}^N w_k}, \quad (2.10)$$

Algorithm 1: Nested Sampling

Input : Likelihood function $\mathcal{L}(\vec{\theta})$, prior distribution $\pi(\vec{\theta})$, and number of live points K **Output:** Evidence estimate Z and posterior samples $p(\vec{\theta}|\vec{d})$

// Initialise the algorithm

Choose K live points $\{\vec{\theta}_1, \vec{\theta}_2, \dots, \vec{\theta}_K\}$ from the prior $\pi(\vec{\theta})$, compute likelihoods $\{\mathcal{L}_k = \mathcal{L}(\vec{\theta}_k)\}$,
set initial prior volume $X_0 = 1$, iteration $i = 0$, and $Z = 0$;

// Starting main loop

while *termination criterion not met* **do** Identify the point $\vec{\theta}_i$ corresponding lowest likelihood, $\mathcal{L}_i = \min\{\mathcal{L}_k\}$; **if** $i == 0$ **then** | Draw X_i from $\mathcal{B}(K, 1)$; **else** | Draw t from $\mathcal{B}(K, 1)$; | $X_i = tX_{i-1}$; **end** Discard the $\vec{\theta}_i$ as a *dead* point, collect the tuple (\mathcal{L}_i, X_i) corresponding to $\vec{\theta}_i$; Increase Z
 by adding $\Delta Z = \frac{1}{2} (\mathcal{L}_i + \mathcal{L}_{i-1}) (X_i - X_{i-1})$;

Evaluate termination criterion;

if *criterion not met* **then** | Sample a new point from the prior such that its likelihood is higher than the point
 | that was just discarded. Add it to the set of live points so that the number of live
 | points is equal to K again; | $i = i + 1$; **else**

| criterion met

end**end**

as mentioned near the beginning of this sub-section.

Although we have defined prior mass X , we have so far not specified how it is calculated once the sampling starts. The quantity X is non-increasing in nature and its value ranges from 1 to 0. Treating it as a random variable, its probability distribution can be approximated with the uniform distribution,

$$X \sim U(0, 1) \quad (2.11)$$

and the corresponding cumulative distribution function is,

$$F(X) = \int_0^X dX' = X. \quad (2.12)$$

The probability that a random variable χ is greater than the prior masses from the full set of prior masses $\{X_i\}$ is

$$P(\chi > \{X_i\}) = \prod_{i=0}^N F(X_i = \chi) = \chi^K, \quad (2.13)$$

where we assume that the samples are independent of each other. The probability density $p(\chi)$ is then given by

$$p(\chi) = \frac{d}{d\chi} P(\chi > \{X_i\}) = K\chi^{K-1}. \quad (2.14)$$

The above equality suggests that random variable χ indeed follows the Beta distribution with

$$\chi \sim B(K, 1). \quad (2.15)$$

We have assumed that X and χ range from 0 and 1. However, as the algorithm progresses, the prior mass X and, in turn, χ shrinks. Let's say they have an upper bounded of X^* , then we can define a shrinkage ratio $t \equiv \chi/X^*$ where

$$t \sim B(K, 1). \quad (2.16)$$

We provide the pseudocode of how the nested sampling progresses in Algorithm block 1. The pseudocode is generalized for K number of live points. For a typical parameter estimation run, one uses $\mathcal{O}(10^3)$ live points.

Terminating criterion

Since the aim of the nested sampling algorithm is to accumulate the evidence Z in small increments of ΔZ , it may be terminated when the increment is smaller than a user-specified number ϵ ,

$$\ln(Z_i + X_i \mathcal{L}_{\max}) - \ln(Z_i) < \epsilon, \quad (2.17)$$

where \mathcal{L}_{\max} is the maximum value of likelihood encountered during sampling.

2.3.1 Limitations of modelled reconstruction

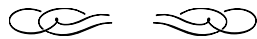
While the nested sampling has become the preferred choice of sampling algorithm for parameter estimation of GW signals [33, 34], it certainly still has some aspects that can be improved upon;

1. Sampling over a variable-dimensional parameter space, i.e., when the dimension of the model itself is an unknown parameter, is not straightforward.

2. The stopping criteria of the algorithm are somewhat arbitrary.
3. The algorithm scales poorly as the dimensions of the model increase.

Despite the limitations, it remains the widely used algorithm for the parameter estimation of GW signals. We use the same to obtain our results in the latter chapters.

Chapter 3



Reconstructing generic excess of power from the data

When reconstructing GW signals to measure source parameters, we typically rely on a *modelled* approach i.e. relying on GW signal models obtained by solving the field equations. However, there are cases where theoretical models either do not exist or are expensive to simulate. For such scenarios, it becomes important to be able to perform *unmodelled* reconstruction. Here, we review how unmodelled reconstruction is done, particularly in a case where robust theoretical models do not exist.

3.1 Artefacts in Gaussian noise

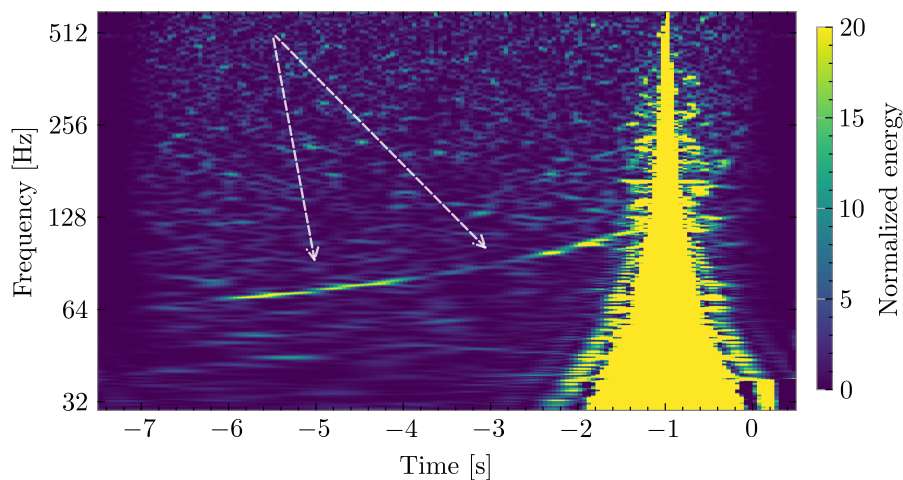


Figure 3.1: Time-frequency spectrogram of a loud glitch overlapping with the binary neutron star signal, GW170817, in the LIGO-Livingston interferometer. Dashed white arrows are added to help the reader trace the signal.

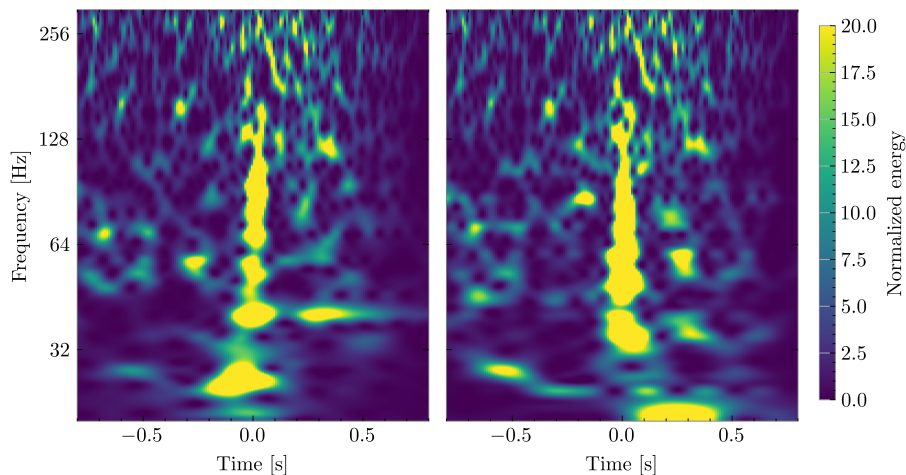


Figure 3.2: *Left*: A GW signal emitted by a BBH merger with a total mass of $176M_{\odot}$. *Right*: An isolated blip glitch.

A case where theoretical models do not exist can be made for instrumental noise transients or *glitches* [35–38]. While the background noise in the GW detectors is often assumed to be Gaussian and stationary (see Eq. (2.2)), the occurrence of a glitch violates this assumption. As most of our physics inferences hinge on the assumption that background noise is Gaussian-stationary, a violation of it could corrupt the inferences. Depending on the time of occurrence, glitches can be problematic in two ways,

- *Glitches overlapping with a GW signal.* Glitches occurring near a GW signal could corrupt the measurements of its source parameters. Therefore, it becomes necessary to carefully subtract the glitch without contaminating the signal, *before* we measure the source parameters. The first detection of a GW signal from the merger of two neutron stars (GW170817) is an example of this kind (Figure 3.1).
- *Glitches in isolation.* Glitches not overlapping with a GW signal increase the false alarm rate of GW detections since some glitches look similar to a signal. For example, Figure 3.2 shows the time-frequency evolution of a GW signal from high-mass BBH mergers (left) and the time-frequency evolution of an isolated blip glitch (right). It becomes important to identify and veto glitchy data from the analyses to reduce false alarms [39, 40].

Glitches could be caused by instrumental (control systems, scattered light) or environmental (earthquakes, wind, anthropogenic) factors, though their origins often remain unknown in many cases [41, 42]. Therefore, it is not possible to devise a theoretical model for glitches in most cases. We need to rely on the unmodelled approach to reconstruct and subtract glitches.

3.2 Transdimensional Sampling Algorithms

When performing unmodelled reconstruction, the dimensionality of the parameter space of $\vec{\theta}$ is unknown, in contrast to the modelled reconstruction explained in chapter 2. While the Bayesian frame-

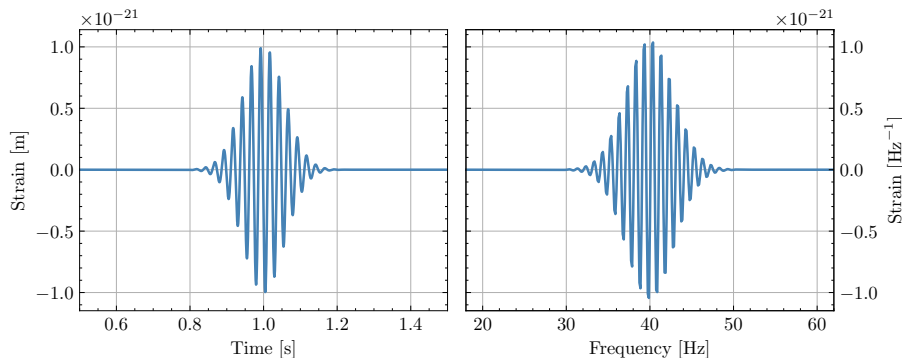


Figure 3.3: Morlet-Gabor wavelet in time (left) and frequency (right) domain

work, GW likelihood, and Bayesian approximation remain robust, the Nested sampling algorithm from the previous chapter is not suitable for the problem at hand. Here, I briefly explain a framework that is routinely used to explore a variable dimensional parameter space [43].

3.2.1 Morlet-Gabor wavelets

When performing unmodelled reconstruction, we use Morlet-Gabor wavelets as base functions. They can be expressed in the time domain as:

$$\vec{\psi}(t; A, Q, t_0, f_0, \phi_0) = A e^{-\frac{(t-t_0)^2}{2\tau^2}} \sin(2\pi f_0(t - t_0) + \phi_0), \quad (3.1)$$

where t denotes time, A denotes amplitude, $\tau = Q/(2\pi f_0)$ denotes the quality factor that controls the spread of the wavelet, ϕ_0 denotes initial phase, t_0 and f_0 respectively correspond to time and frequency at the peak of the amplitude. In Figure 3.3, we show a time (left) and frequency (right) domain representation of a wavelet with parameters $Q = 20$, $t_0 = 1$ second, and $f_0 = 40$ Hz.

Morlet-Gabor wavelets are suitable for the problem at hand because glitches (\vec{g}) we want to reconstruct can be approximated by a linear combination of N wavelets [43],

$$\vec{g}(t; \vec{\theta}) = \sum_{k=0}^N \vec{\psi}_k(t; \vec{\theta}_k), \quad (3.2)$$

where $\vec{\theta}$ is set of $N \times 5$ parameters since each $\vec{\psi}_k$ needs 5 model parameters shown in Eq. (3.1). A desirable feature is that Morlet-Gabor wavelets preserve shape when switching between time-frequency domains and they have a simple analytic expression in both domains.

Besides $\vec{\theta}$, here N itself is an unknown parameter therefore the dimensionality of the parameter space we want to explore is also unknown. The transdimensional algorithm used to tackle this problem is an extension of the Markov chain Monte Carlo methods.

3.2.2 Markov chain Monte Carlo

Markov chain Monte Carlo (MCMC) is a subclass of Monte Carlo methods, a class of computational methods that rely on repeated random sampling. Markov chain in particular refers to an iterative

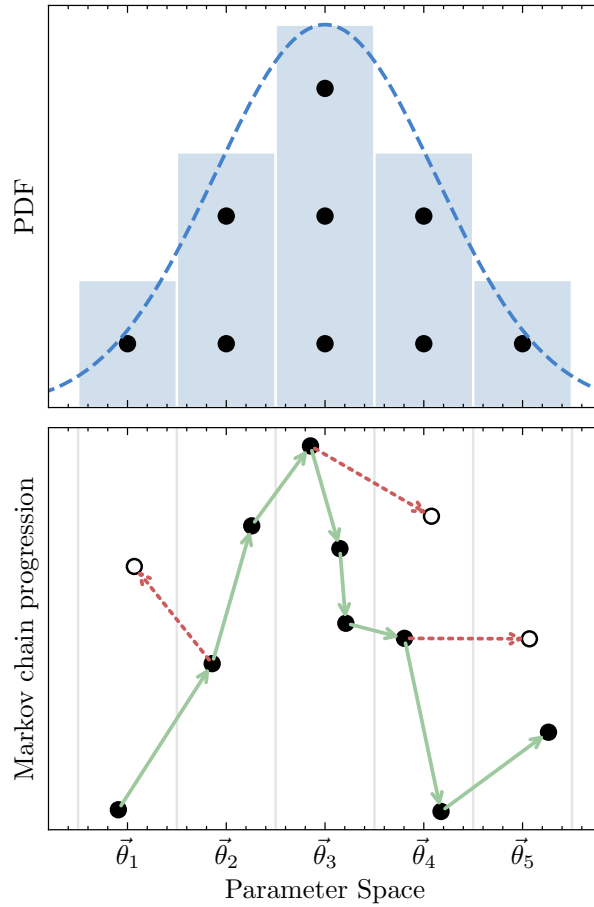


Figure 3.4: *Bottom:* Progression of a Markov chain in the parameter space of $\vec{\theta}$. Each arrow represents an iteration, solid black dots represent accepted proposals and empty dots represent rejected proposals. *Top:* Posterior probability distribution constructed from the accepted samples of the Markov chain of the bottom plot.

process where the probability of accepting a proposal at t^{th} iteration depends only on the point from the previous iteration. If we denote the probability by p_t ,

$$p_t(\vec{\theta}^t) = \int d\vec{\theta}_{t-1} T(\vec{\theta}^t, \vec{\theta}_{t-1}) \vec{\theta}_{t-1}, \quad (3.3)$$

where $\vec{\theta}^t$ is the proposed point, $\vec{\theta}_{t-1}$ is the point from previous iteration, and T is the transition probability.

Traditional MCMC algorithms aim to obtain the samples from posterior probability distribution which is in contrast to the Nested sampling algorithm where the aim is to compute the evidence and posterior distributions are the byproduct. Obtaining the evidence after an MCMC algorithm is terminated requires additional computations. Nevertheless, here we outline one such MCMC algorithm called the Metropolis-Hastings algorithm.

Metropolis-Hastings algorithm

Metropolis-Hastings algorithm makes use of a proposal density function (Q) to determine whether a proposal point $\vec{\theta}'$ should be accepted. The probability that $\vec{\theta}'$ is accepted is then given by α

$$\alpha = \min \left\{ 1, \frac{p(\vec{\theta}'|\vec{d})}{p(\vec{\theta}_{t-1}|\vec{d})} \frac{Q(\vec{\theta}_{t-1}|\vec{\theta}')}{Q(\vec{\theta}'|\vec{\theta}_{t-1})} \right\}. \quad (3.4)$$

Where $p(\vec{\theta}|\vec{d})$ is the posterior probability distribution (already defined in the chapter 2). If the proposal is accepted, $\vec{\theta}'$ is updated to $\vec{\theta}_t$ and the steps are repeated. The quantity Q can be a Gaussian distribution or any distribution from which we know how to draw samples. Figure 3.4 shows an illustration of the progression of a Markov chain (bottom) and posterior distribution constructed from the accepted samples (top).

3.2.3 GW specific treatment for jumping between dimensions

A general treatment of switching dimensions was proposed in 1995 by Peter Green [44]. The method was initially proposed to determine which distribution fits the data best among various competing distributions. Additionally, two competing distributions do not need to have the same number of model parameters and the algorithm can jump back and forth between different dimensions. Therefore, it is commonly known as the reversible jump Markov chain Monte Carlo (RJMCMC) method. Since its inception, this sampling method has been applied to various use cases in gravitational wave data analysis. Here, I discuss its application in the context of reconstructing any excess of power, i.e., the excess of power can be due to GW signals or glitches. Jumping between the dimensions in this case means,

- *Birth move* – addition of new wavelet
- *Death move* – removal of an existing wavelet
- *Stationary move* – swapping an existing wavelet for a new wavelet.

The stationary move is trivial and the same as the Metropolis-Hastings algorithm. The birth and death moves are typically the most complicated ones.

Before explaining the steps required to perform birth and death moves let us define a few standard quantities. Let us denote the current state by $\vec{\theta}$ and a proposal state by $\vec{\theta}'$. Let us say that state $\vec{\theta}$ has N wavelets and $\vec{\theta}'$ has N' wavelets. Since each wavelet needs 5 model parameters (Eq (3.1)), the vector $\vec{\theta}$ has $5 \times N$ dimensions and the vector $\vec{\theta}'$ has $5 \times N'$ dimensions. We denote the dimensions of $\vec{\theta}$ ($\vec{\theta}'$) by D (D'). Now we can rewrite the acceptance ratio α from Eq (3.4) as,

$$\alpha = \min \left\{ 1, \frac{p(\vec{\theta}', D'|\vec{d})}{p(\vec{\theta}, D|\vec{d})} \frac{Q(\vec{\theta}, D|\vec{\theta}', D')}{Q(\vec{\theta}', D'|\vec{\theta}, D)} \right\}. \quad (3.5)$$

From Lower to Higher dimension

Let's say we want to jump from a one-wavelet state $\vec{\theta}$ to a two-wavelet state ($\vec{\theta}'$). So $\vec{\theta}'$ will have five (ten) dimensions. Since the current state has fewer dimensions than the proposed state, we need two additional quantities to account for the missing dimensions:

- An auxiliary probability distribution (\vec{p}_{aux});
- A bijective and continuously differentiable function i.e. a diffeomorphism (h);

The user may choose any auxiliary probability distribution from which it is easy to sample as long as the dimensions match

$$\dim[\vec{\theta}] + \dim[\vec{p}_{\text{aux}}] = \dim[\vec{\theta}']. \quad (3.6)$$

Let \vec{p}_{aux} be a five-dimensional uniform distribution and let the bijective function be an exponential so the logarithmic function will be its inverse.

For simplicity of the notation, we write down only the wavelet amplitude parameters (see Eq. (3.1)) of the current state (A_1) and the proposed state (A'_1, A'_2). Let w be a sample from \vec{p}_{aux} ;

$$(A_1, w) \xrightarrow{f} (A_1, e^w) := (A'_1, A'_2). \quad (3.7)$$

We choose an f mapping A_1 to A'_1 and w to e^w . Now, the dimension of the current state matches the dimensions of the proposed state. Another remaining factor is the determinant of the Jacobian,

$$\left| \frac{\partial(A'_1, A'_2)}{\partial(A_1, w)} \right| = \begin{vmatrix} \frac{\partial A'_1}{\partial A_1} & \frac{\partial A'_1}{\partial w} \\ \frac{\partial A'_2}{\partial A_1} & \frac{\partial A'_2}{\partial w} \end{vmatrix} = e^w, \quad (3.8)$$

which accounts for the change of variables. The acceptance ratio can now be written as,

$$\alpha = \min \left\{ 1, \frac{p(\vec{\theta}'|\vec{d}) \vec{p}_{\text{aux}}(w) p(D'|D) \left| \frac{\partial(A'_1, A'_2)}{\partial(A_1, w)} \right|}{p(\vec{\theta}|\vec{d}) p(D|D')} \right\}. \quad (3.9)$$

If we assume that all states are equally likely i.e. $p(D|D') = p(D'|D)$, and substitute the value of the determinant from Eq.(3.8),

$$\alpha = \min \left\{ 1, \frac{p(\vec{\theta}'|\vec{d})}{p(\vec{\theta}|\vec{d})} \vec{p}_{\text{aux}}(w) e^w \right\}. \quad (3.10)$$

From higher to lower dimension

When going from high dimensions to low dimensions, it is incorrect to simply do;

$$\text{Incorrect : } (A'_1, A'_2) \rightarrow (A_1). \quad (3.11)$$

We need to define the inverse of f . The inverse will be a logarithmic function since we chose f to be the exponential function. Let us denote the inverse by f' , then when going from higher dimension to lower dimensions,

$$(A'_1, w') \xrightarrow{f'} (A_1, \ln w'), \quad (3.12)$$

where w' is either chosen from another auxiliary distribution \vec{p}'_{aux} and it may or may not be the same as the previous auxiliary distribution \vec{p}_{aux} . The Jacobian and acceptance ratio in this case will turn out to be;

$$\left| \frac{\partial(A_1, A_2)}{\partial(A'_1, w')} \right| = \begin{vmatrix} \frac{\partial A_1}{\partial A'_1} & \frac{\partial A_1}{\partial w'} \\ \frac{\partial A_2}{\partial A'_1} & \frac{\partial A_2}{\partial w'} \end{vmatrix} = 1/w' \quad (3.13)$$

$$\alpha = \min \left\{ 1, \frac{p(\vec{\theta}|\vec{d})}{p(\vec{\theta}'|\vec{d})} \vec{p}_{\text{aux}}(w') \frac{1}{w'} \right\} \quad (3.14)$$

3.3 Limitations and use-cases of the unmodelled reconstruction

Although the unmodelled reconstruction discussed in this chapter has some important use cases, it has a few limitations.

1. In contrast to Nested sampling, the aim here is to obtain the posterior probability distribution. Additional computations are required to obtain the evidence.
2. The rate of convergence in the case of RJMCMC depends on the choice of auxiliary distribution and bijective functions. A universal choice that works for all use cases in GWs is difficult to determine. It has a larger number of tuning parameters compared to the fixed dimension reconstruction done by Nested sampling.
3. The termination criteria are not well defined.
4. The lack of orthogonality of Morlet-Gabor wavelets may also reduce the rate of convergence.

Despite the limitation, it remains the state-of-the-art approach to reconstruct instrumental glitches, noise power spectral density, and reconstruction of signals which are costly to simulate, such as GWs from the core-collapse of supernova and the post-merger phase of a BNS signal. Specifically, the methodology for unmodelled reconstruction described in this chapter makes the core of the `BayesWave` codebase [43, 45]. We will discuss more about this in the next chapter.

Chapter 4



A framework to utilize the triangular geometry of the Einstein Telescope for precision science

While the third-generation detectors are anticipated to push the accuracy and precision of our measurements to unprecedented levels, they will also be subject to new kinds of challenges compared to the current generation detectors. Here, I specifically compare the impact of glitches on GW signals detected by LIGO-Virgo interferometers and by 3G interferometers.

When occurring in the vicinity of a GW signal, glitches (or transient noises) can corrupt the signal. Such signal-overlapping glitches must be carefully removed before analysing the signal. From the 90 confident events detected across three observation runs by LIGO-Virgo interferometers, about 20 were contaminated by glitches and required some form of glitch mitigation [46]. This number will continue to increase as the interferometers collect more data. A detailed study on how the physical interpretation of a GW signal may vary, depending on how a glitch in its proximity is removed, was conducted in the context of GW191109 [47]. Specifically, it was argued that the interpretation of the spins of black holes may be affected.

While glitch mitigation is an active area of research for current generation detectors, it is yet to receive similar attention in the context of 3G detectors. In Table 4.1, we compare the problem posed by glitches for the LIGO-Virgo and the 3G interferometers. Glitches could be a major bottleneck in transitioning to the precision science era. In this chapter, we introduce the `nijntje` – a null stream inspired noise transient elimination framework that is inexpensive, accurate, and scalable against the increasing computational cost of data analysis in the 3G-era. Through `nijntje`, we demonstrate a clear edge that the null stream, inherent in the triangular configuration of the Einstein Telescope, provides for the precision science era.

4.1 The null stream

LIGO-Virgo interferometers	Third-generation interferometers
1. Detection rate of $\mathcal{O}(1)$ signal per week	1. Detection rate of $\mathcal{O}(1)$ signal per minute
2. A GW signal is in-band for $\mathcal{O}(1)$ second to $\mathcal{O}(1)$ minute. Therefore, nearly every segment of data contains only noise.	2. A GW signal is in-band for $\mathcal{O}(1)$ minute to $\mathcal{O}(1)$ hour. Therefore, nearly every segment of data is expected to contain a signal.
3. Glitch rate of $\mathcal{O}(1)$ per minute across three observation runs.	3. Glitch rate is unknown. Let's assume the same as LIGO-Virgo interferometers.
4. <i>Almost</i> all glitches occur in isolation due to a smaller in-band duration and smaller detection rate of GW signals.	4. <i>Almost</i> all glitches will overlap with a GW signal due to a larger in-band duration and larger detection rate.
5. Almost all glitches can be vetoed (excluded from the analyses) without incurring a significant loss of GW signals.	5. Very few glitches may be vetoed without losing GW signals.

Table 4.1: Impact of glitches on the LIGO-Virgo signals in comparison to the anticipated 3G signals.

By definition, the null stream is a linear combination of strain data from a network of GW detectors such that the signal (if present in the strain) cancels out. For the triangular configuration of the Einstein Telescope (ET- Δ), the null stream can be constructed by summing the strain data from three detectors. Let us denote the data from i^{th} detector by \vec{d}_i ,

$$\vec{d}_i = F_{+,i}\vec{h}_+ + F_{\times,i}\vec{h}_\times, \quad (4.1)$$

where i varies from 1 to 3, $F_{+,i}$ and $F_{\times,i}$ are the antenna pattern functions of i th interferometer. The notations h_+ and h_\times represent the GW polarisations, defined in chapter 1. The null stream is then constructed by;

$$\vec{d}_{\text{null}} = \frac{1}{\sqrt{3}} \sum_{i=1}^3 \vec{d}_i, \quad (4.2)$$

where the prefactor of $1/\sqrt{3}$ ensures that the noise's power spectral density of the null stream equals the average of those of the individual detectors.

The null stream is a geometric feature of the triangle configuration of ET. It comes about from the fact that the sum of antenna pattern functions is individually zero,

$$\sum_{i=1}^3 F_{+,i} = 0 \quad \text{and} \quad \sum_{i=1}^3 F_{\times,i} = 0. \quad (4.3)$$

We note that individual antenna pattern functions do vary over the whole sky (see Eq. (1.38)). But

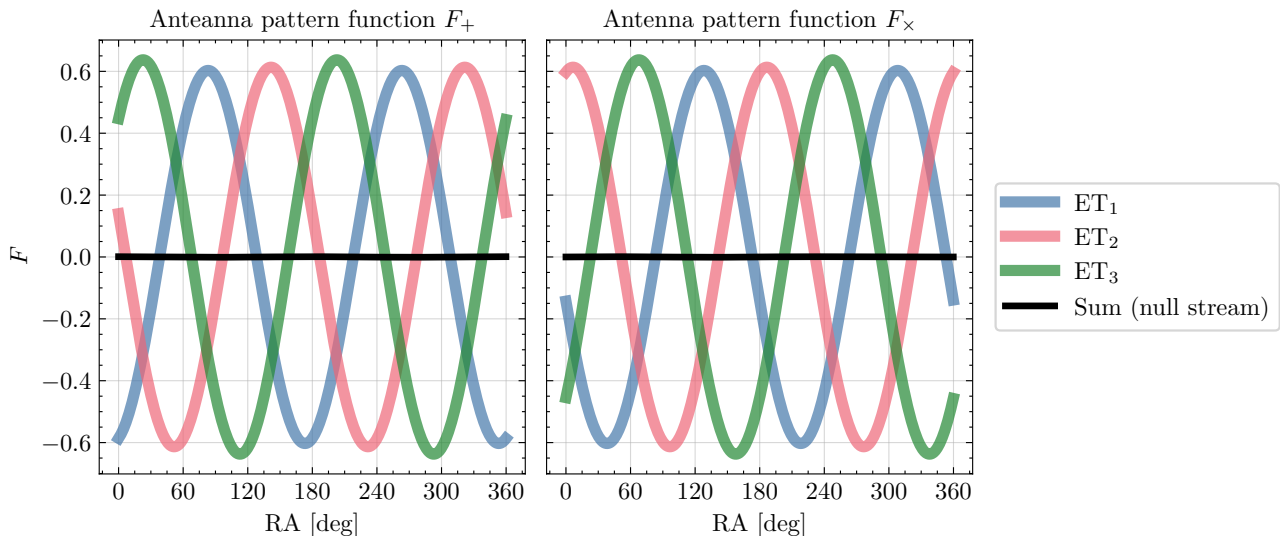


Figure 4.1: Illustration of how the null stream of ET- Δ comes about. Projection of plus (left) and cross (right) antenna pattern functions along the right ascension (RA) coordinate. Blue, red, and green lines show the antenna pattern functions of ET₁, ET₂, and ET₃, respectively. The black line, which is equal to zero for all values of RA, is obtained by summing the three. For simplicity, I only shown the projection along RA. The sum of the three is zero at all sky locations. This feature gives rise to an inherent null stream in the triangular configuration of ET.

the equalities presented in Eq. (4.3) hold for the whole sky. As an illustration, we show the projection of antenna pattern functions along the right ascension (RA) coordinate in Figure 4.1.

4.2 *nijntje*: null-stream inspired noise transient elimination framework

The null stream of the triangular ET enables a novel framework to remove signal-overlapping glitches. For brevity, we refer to it as *nijntje* – null-stream inspired noise transient elimination – framework. Figure 4.2 shows the workflow of the *nijntje* framework. In this section, we explain the setup of our simulations and the operations within the *nijntje* framework.

Setup of the simulation

We consider a typical scenario where a glitch overlaps with a GW signal. While the glitches exhibit a range of morphologies, here we choose a morphology that is ubiquitous in the data, i.e., the blips [48]. For the sake of the example, we assume that the only interferometer encounters the glitch. The rest of the two interferometers of the triangle contain a GW signal in Gaussian noise. The GW source is placed at a redshift of 2, where the merger rate distribution of BBH peaks, making it a typical source. The source frame masses of the two black holes are $38 M_\odot$ and $33 M_\odot$. We use the IMRPhenomD waveform model for our analysis. These configuration choices results in a GW signal with a network optimal (SNR) of 83 divided equally among three interferometers (see Eq. (2.4) for the definitions of SNR). The starting frequency of our analysis is 20 Hz, the sampling frequency is 2048 Hz, and we use

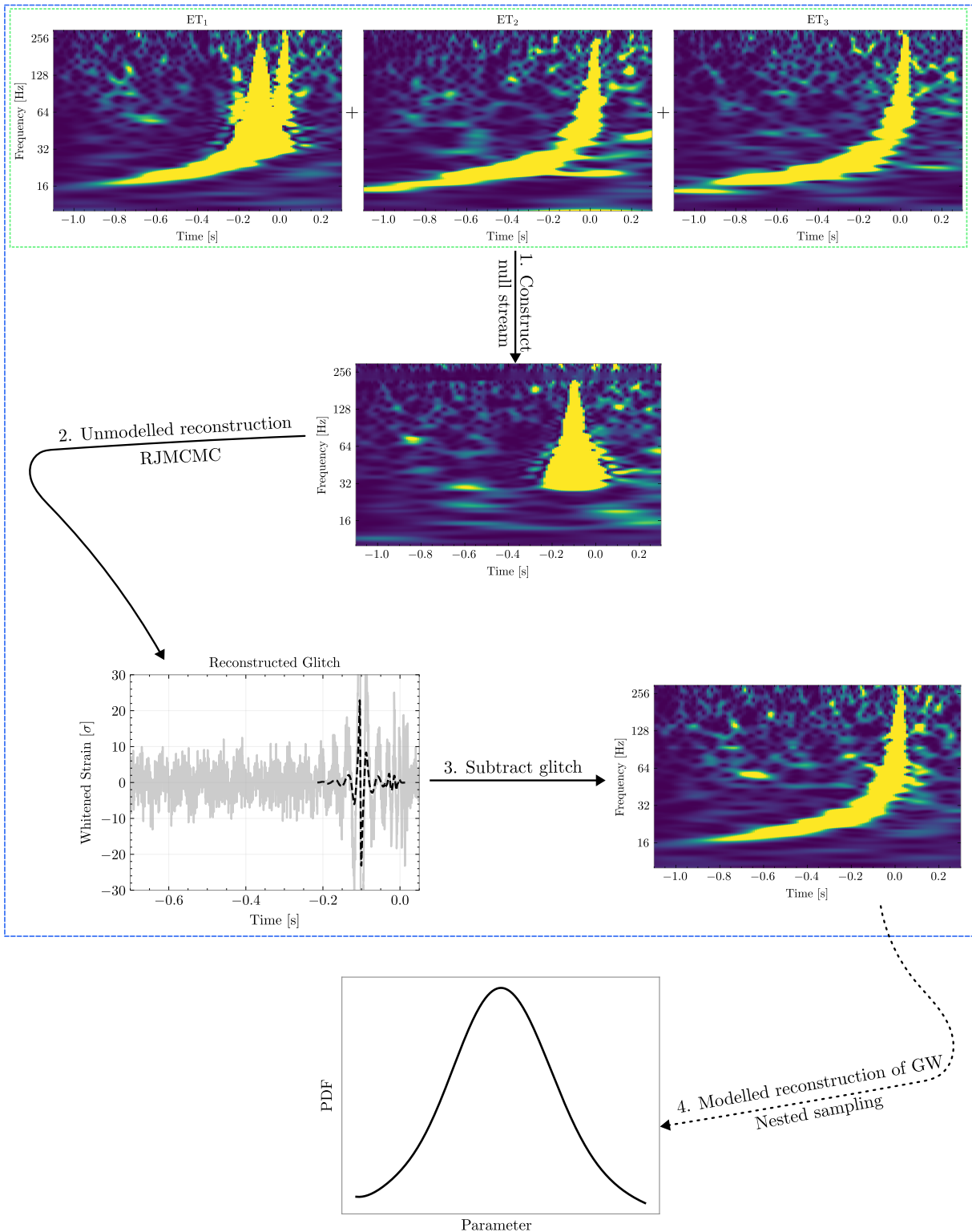


Figure 4.2: The blue box outlines the workflow of `nijtje` framework. *Step 1:* Construct the null stream by summing the strain data from three interferometers. *Step 2:* Using the null stream data and an RJMCMC method, perform an unmodelled reconstruction of the glitch time series. *Step 3:* Subtract the glitch time series from ET_1 data to obtain the *cleaned* data. *Step 4 (Optional):* Perform parameter estimation of the GW signal using the cleaned data from ET_1 , and the existing data from ET_2 and ET_3 to verify the accuracy of glitch mitigation.

ET-D power spectral density (PSD) to simulate Gaussian noise. The ET-D PSD is currently the best prediction for what the noise PSD of ET may look like [49]. Each arm of the triangle is 10km long. We inject a blip glitch in the ET₁ interferometer that overlaps with the GW signal. We ensure that the SNR of the glitch is similar to the SNR of the GW signal in ET₁, i.e., $83/\sqrt{3} \sim 47$. Thanks to recent developments in machine learning based methods, it is now possible to simulate glitches. For example, the `gengli` codebase can generate blip glitches akin to the ones observed during the second observing run of Advanced LIGO and Virgo [50, 51]. An illustration of this setup is shown in the top panel of Figure 4.2. In our setup, the glitch is only in ET₁ interferometer, the rest of the two interferometers contain the GW signals in Gaussian noise.

Executing the steps of *nijntje* framework

Following the steps outlined in Figure 4.2, we formulate the null stream in step 1. By construction, the null stream does not contain any signal. It only contains the glitch and the sum of Gaussian noise from three interferometers. To subtract the glitch, we first want to obtain the corresponding time series. We do this using the unmodelled reconstruction method described in chapter 3. Indeed, we do not need to be concerned about the possible leakage from the GW signal while performing the glitch reconstruction using the null stream.

In step 2, we reconstruct the glitch from the null stream. Specifically, we obtain the time series corresponding to the median parameters of the posterior samples. In step 3, we subtract it from the ET₁ interferometer data, making sure that it is scaled by a factor of $\sqrt{3}$ and the glitch onsets are aligned. This completes our step 3, and we finally *cleaned* the glitch from ET₁.

Next, to verify that our glitch mitigation is accurate, i.e., we have not removed part of the signal or we have not left behind a part of the glitch, we perform modelled reconstruction (also known as parameter estimation) on the GW signal, as described in chapter 2. We can compare the parameter measurements obtained by analysing the cleaned data with the one obtained from the data when we do not introduce any glitch. The latter serves as the benchmark for our comparison. Indeed, the parameter estimation step can be used to test the quality of glitch mitigation only in a simulated setting. In reality, we do not have a benchmark for comparison.

4.3 Glitch mitigation in the absence of *nijntje* framework

The framework *nijntje* is unique to the triangular geometry of the ET (ET- Δ). To compare ET- Δ with an alternate configuration, we consider a network of two, distant L-shaped interferometers (referred to as ET-2L) located in Sardinia and the EMR region. In the absence of the *nijntje* framework, we perform a joint reconstruction of the GW signal and the glitch using the data from both interferometers. The joint modelling is prone to leakage, i.e, part of the glitch could be mismodelled as part of the signal and vice versa. Therefore, as introduced in Chatziioannou *et al.* [52], instead of modelling the GW signal itself with sine-Gaussian wavelets, a realistic signal model is employed with the expectation of reducing the mismodelling.

The setup of the simulation for the ET-2L network remains similar to the one described in section 4.2. The GW signal parameters and the glitch morphology are the same as ET- Δ , leading to a

GW network SNR of 124, with the Sardinia and EMR interferometers contributing SNRs of 90 and 85, respectively. The arm length of each interferometer is 15 km, and the power spectral density (ET-D) is scaled accordingly, resulting in a higher GW signal SNR compared to ET- Δ . The glitch is introduced in the Sardinia interferometer, whose SNR matches the glitch SNR in ET₁. For this setup, we perform a glitch mitigation using the BayesWave codebase – a routinely used tool to perform joint modelling of the GW signal and glitch coherently across the detector network [43, 45, 52, 53]. To reiterate, the GW signal here is modelled using the signal model (i.e. the IMRPhenomD model) and the glitch is modelled using wavelets.

One can model both the signal and the glitch using wavelets. This approach does not require prior knowledge of the GW signal model and, therefore, may seem ideal. However, this approach increases the amount of mismodelling and is hence not preferred [52].

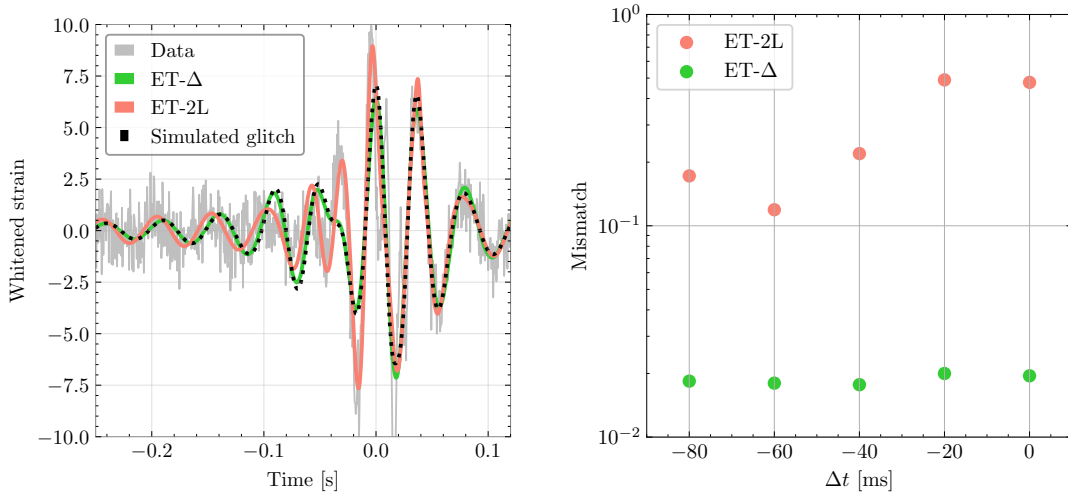


Figure 4.3: *Left:* Green (red) indicates the glitch reconstructed using ET- Δ null stream (ET-2L) for the $\Delta t = 0$ case. Grey shows the strain, and black shows the simulated glitch. The null stream helps avoid glitch mismodelling, resulting in much closer agreement with the simulated glitch. *Right:* Quantifying the *mismatch* between the reconstructed glitch and the true glitch for various time separations between the glitch onset and GW merger. The triangular configuration leads to consistently lower mismatches (green dots) compared to the ET-2L configuration (red dots).

4.4 Results of source parameter measurement: Triangle and 2L comparison

For each configuration, ET- Δ and 2L, we consider nine different scenarios. All settings are kept identical across these scenarios except the time interval between the GW merger and glitch onset. The top left plot inside the green panel in Figure 4.2 represents an instance when glitch onset is ≈ 100 ms away from the merger. The nine scenarios that we analyse include instances where the glitch onset is away from the merger as well as coinciding with the merger. For ET- Δ , we perform glitch mitigation using `nijntje` to obtain the cleaned data. For ET-2L, in the absence of the `nijntje` framework, we perform glitch mitigation by doing joint signal plus glitch modelling. After the glitch is removed, we

perform parameter estimation to quantify the accuracy of glitch mitigation. If the glitch mitigation is precise, the measurement should be similar to a scenario where a glitch is not introduced to the data.

Before we present the parameter estimation results, we showcase the results of glitch mitigation, i.e., how close the reconstructed glitch is to the true glitch. This serves as a precursor to the parameter estimation results since accurate glitch mitigation leads to accurate parameter measurement of GW. A visualisation of the glitch reconstruction is presented in Figure 4.3. Specifically, the left plot of Figure 4.3 shows the results of glitch reconstruction when the GW merger coincides with the glitch onset. We find that the ET triangle configuration, due to the null stream, achieves a more accurate glitch reconstruction by avoiding mismodeling from the GW signal. In contrast, for the ET-2L configuration, inevitably, some additional features from the signal are incurred.

To quantify how close the reconstructed glitch is to the truth, we calculate the mismatch,

$$\mathcal{M} \equiv 1 - \frac{\langle h_1|h_2 \rangle}{\sqrt{\langle h_1|h_1 \rangle \langle h_2|h_2 \rangle}} \quad (4.4)$$

between the reconstructed glitch and the true glitch. The inner products $\langle .|. \rangle$ are defined in chapter 2. We find that glitch reconstruction without the null stream consistently leads to higher mismatches (see right plot of Figure 4.3). A large mismatch may imply erroneous glitch mitigation, leading to erroneous GW parameter estimation.

Glitch onset coinciding with the GW merger

Next, we turn to the results of parameter estimation when the glitch onset precisely coincides with the GW merger. Figure 4.4 presents a comparison of the posterior distributions of the GW signal parameters after the glitch is mitigated, for $\Delta t = 0$. For all parameters shown, glitch mitigation with null stream for ET- Δ results in posteriors that demonstrate high consistency and closely align with the benchmark results, where “benchmark” refers to a scenario when no glitch is introduced to the data.

For the ET-2L configuration, though the total mass M_{total} posterior shows clear signs of widening, it recovers the true value. This can be attributed to the SNR in the glitch-free interferometer, enabling intrinsic parameter recovery. In contrast, posteriors for extrinsic parameters, namely luminosity distance and sky location, are inconsistent with the benchmark’s posteriors and miss the true value.

Glitch onset away from the GW merger

Finally, we turn to the scenarios when the glitch does not coincide with the merger. Figure 4.5 shows that the characteristics of extrinsic parameter recovery remain consistent across different Δt values. A negative (positive) value of Δt implies that the glitch onset falls before (after) the GW merger. We show the measurements of distance (D_L) and sky localisation (Ω). The sky localisation contours are constructed from the right ascension and declination measurements.

For all time intervals considered, the ET- Δ configuration yields measurements where the true distance and sky location lie within 3σ and closely align with the no-glitch benchmark. In contrast, with the ET-2L configuration, the resulting measurements are wider or generally exclude the true

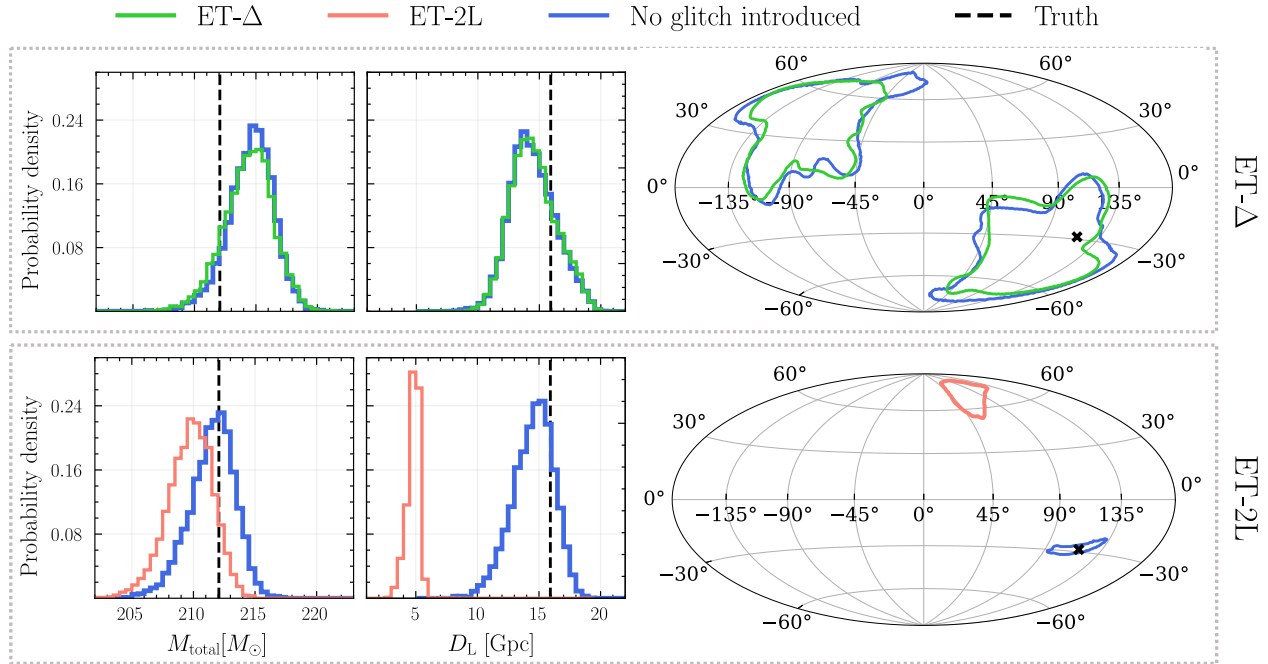


Figure 4.4: Measurement of detector-frame total mass M_{total} , luminosity distance D_L , and sky localisation. Green (red) colour represents posterior distributions when the glitch is removed using the ET- Δ null stream (ET-2L). Blue colour shows the measurements when no glitch is introduced, serving as a benchmark for comparison, and dashed black lines indicate the true values. The green posteriors accurately recover the true parameter values and show high consistency with the benchmark. Though the red posterior for the total mass M_{total} recovers the true value, it shows clear signs of bias and widening. In contrast, the measurements of luminosity distance and sky location are biased and miss the true values.

values, except when the glitch onset is 100 ms before or 20 ms after the merger. We infer that at those values of Δt , the glitch is far enough from the GW signal to cause any biases.

4.5 Outlook

The null stream provides us with an extra piece of information in the form of Eq. (4.2). For the first time, we quantitatively show how this information can be used to address a pressing problem in GW related measurements. Further, in the table 4.2, we summarise the comparison between the ET- Δ and ET-2L configuration in the context of glitch mitigation.

Implication on the science cases

In the absence of the null stream, the sky location and luminosity distance measurements of the GW source are subject to significant biases due to mismodeling of glitches, even if the signal model is accurately known. Such biases could be harmful to science cases measuring cosmological parameters, in particular the “dark siren” method, which relies on three-dimensional volumetric matching between GW detections and galaxy catalogs [54–60]; the null stream will be of help here.

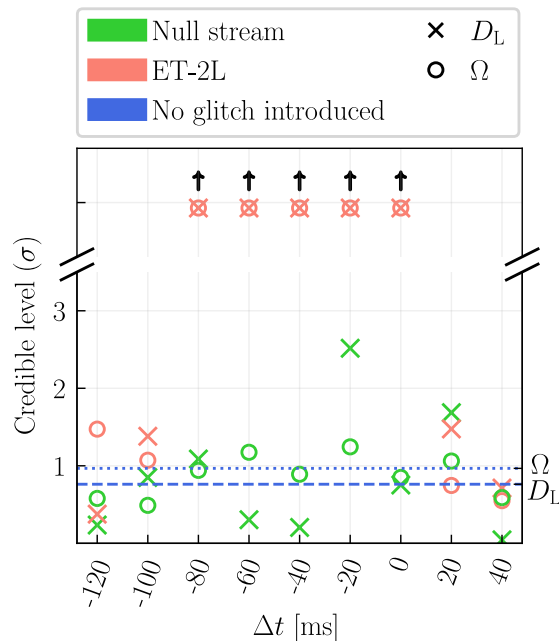


Figure 4.5: A comparison of the credible level of the true parameter value relative to the posterior distributions for various time intervals Δt between glitch onset and GW merger. Credible levels are in standard deviation units σ , following a standard normal distribution. The parameters considered are luminosity distance D_L and sky location Ω . Green (red) markers denote credible levels for the ET- Δ null stream (ET-2L) based measurements, and the blue lines provide credible levels in the absence of a glitch as a benchmark (dotted for Ω , dashed for D_L). For the null stream-based approach, the credible levels closely align with the benchmark, indicating accurate measurements. The posteriors for ET-2L lead to wider credible levels and generally exclude the true value, except for the edge cases where the glitch is sufficiently distant in time from the GW merger.

Similarly, ET is anticipated to reconstruct the merger rate distributions as a function of redshift. This is achieved by converting the GW distance measurements to a redshift using a cosmological model [20]. This science case will benefit from the null stream.

Einstein Telescope is also expected to provide a unique opportunity to perform multimessenger astronomy. By producing early warning alerts, i.e., information about the sky localisation of the GW signal before they merge, ET can help observe any electromagnetic emission associated with the GW merger [61, 62]. An incorrect or biased sky localisation due to glitches may hinder our ability to produce early warning alerts.

Searches for strong lensing of GW signals look for overlaps between the parameters of two GW signals [63]. The reconstruction of the lens galaxy also relies on accurate measurements of GW parameters, including distance and sky localisation. Biases in these measurements due to glitches could be harmful to strong lensing searches and follow-up lens reconstruction [64–66].

Searches for anomalous dispersion of gravitational waves due to violations of general relativity also require accurate distance measurements [67]. Biases caused in the distance measurements due to glitches could be harmful here as well. Another science cases that require accurate distance measurements is the search for anomalous propagation of gravitational waves, discussed in more detail in chapter 6.

Glitch mitigation using ET-2L	Glitch mitigation using ET- Δ
<ol style="list-style-type: none"> 1. Biases expected in the measurements. 2. The signal model needs to be known <i>a priori</i>. Biases expected to worsen if the signal model is not known or incorrect. 3. Difficult to scale to meet the demands of 3G-era. Specifically, to analyse the long, loud, and overlapping signals of the 3G-era. $\mathcal{O}(10)$ hours per analysis. 4. Biases worsen when two interferometers have unequal SNRs, i.e, the signal is in the blind spot of one L but bright spot of another. 	<ol style="list-style-type: none"> 1. Quality of measurements is nearly identical to the scenario when glitches are not introduced. 2. Does not require any prior knowledge of the signal model. 3. Enables an inexpensive, accurate, and easily scalable framework <code>nijntje</code>. A ready-to-use tool to analyse the long, loud, and overlapping signals using ET-Δ. The framework can be scaled to $\mathcal{O}(1)$ second per analysis. 4. Individual interferometer SNRs do not matter. Blind spots do not play a role.

Table 4.2: Comparison ET- Δ and ET-2L configuration in context of glitch mitigation

We note that in studies where information from multiple GW sources is combined, it will often be a relatively limited set of loudest signals that drive the combined result (tests of general relativity being a clear example [67]). If measurements on even a small fraction of these events are corrupted, it could adversely affect inference on the population as a whole.

Future work

Our simulations illustrate that the triangular configuration of the Einstein Telescope outperforms the 2L configuration in terms of glitch mitigation. Accurate glitch mitigation subsequently enables accurate measurements of gravitational wave parameters. However, we acknowledge that further analysis is required to present a more complete comparison. Specifically, we plan to analyse 1 year of simulated data with realistic GW signals and glitches for both configurations of the Einstein Telescope.

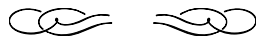
Before we carry out such a comparison, we need to develop certain building blocks which are missing at the time of writing this thesis. Specifically, our knowledge about glitches, i.e., their morphologies, rates, and SNR distribution, is largely based on the glitches of LIGO and Virgo interferometers. It is possible that the glitches in the 3G era do not follow similar distributions. Additionally, the low frequency regime (5 to 20 Hz) and the high frequency regime (above $\approx 10^3$ Hz) are of special interest in the 3G era. However, the distribution of glitches in these regimes is relatively unknown and may be difficult to determine until the 3G detectors become operational. These frequency regimes are currently

outside of typical LIGO-Virgo bandwidths. Moreover, the codebase to perform glitch mitigation for the 2L configuration (i.e. BayesWave) is tuned to analyse the LIGO-Virgo data. Though in our work we have made the best use of this state-of-the-art framework, a next-generation of BayesWave or a similar tool is required to perform glitch mitigation for the 2L configuration. Specifically, a tool that can remove glitches contaminating the long, loud, and overlapping signals of the 2L configuration is needed to perform a complete comparison.

Inspired by the seminal work of Dooney *et al.* [68], the integration of a deep learning based noise mitigation tool into the `njntje` framework is already underway. This feature will enable the `njntje` framework to run on GPUs, leading to a real-time glitch mitigation ($\mathcal{O}(1)$ second per glitch) and overall a sustainable approach for computation. This feature also makes `njntje` ready to analyse realistic GW signals and glitches in the triangular configuration of the Einstein Telescope.

The problem posed by glitches to the current and next-generation GW detectors is a pressing one. It could hinder our transition to the precision science era. The comparison presented in this chapter shows a clear edge that the null stream inherent in the triangular configuration has to offer over the alternate configuration.

Chapter 5



A fast parameter estimation method for the current and next generation detectors

Bayesian inference discussed in chapter 2 is the key to achieving a wide range of scientific insights from gravitational wave signals. The cost of the inference increases with the complexity of the signal model and the signal’s duration. Currently, parameter inference on one signal takes $\mathcal{O}(1)$ days. Additionally, for the third-generation detectors, due to the longer duration and increased detection rate of the signal, the cost of parameter inference could quickly become intractable. To address these issues, we present a fast parameter estimation method that includes higher-order modes and precession using relative binning. These effects are important in the context of GW signals from binary black hole mergers, as the inclusion of them provides a more complete description of the phenomenon. Additionally, we extend the method to analyse isolated signals as well as overlapping signals in the 3G era. We also adapt our method to perform strong lensing searches. Indeed, a fast parameter estimation method has a wide range of applications. Specifically, using our method, we analyse

1. A set of simulated BBH signals covering the full parameter space to establish validity.
2. Two LIGO-Virgo events with significant contribution from higher order modes: GW190412 [69] and GW190814 [70].
3. A set of simulated GW signals for the 3G-detectors, isolated as well as overlapping.
4. The event pair GW191103–GW191105 as well as a set of simulated pairs, to investigate the strong lensing hypothesis.

5.1 Mode-by-mode relative binning

When performing the Bayesian parameter inference on a GW signal, we need to simulate a large number ($\approx 10^6$ to 10^7) of waveforms. This is the most expensive part of the process. Each waveform

is generated on a uniform frequency grid whose minimum and maximum frequencies depend on the bandwidth (typically 20 Hz to 2048 Hz) of the GW detectors. The resolution of the frequency grid is set to $1/T$, where T is the duration of the signal. Generating a large number of waveforms on a uniform grid increases the computational cost. The relative binning method seeks to address this issue by generating the waveform on a sparse frequency grid and interpolating on the remaining points in such a way that the accuracy of the analysis has a negligible effect. The usage of the sparse frequency grid leads to a speed up.

From chapter 2, let us recall the (log) likelihood function,

$$\ln \mathcal{L}(\vec{\theta}) = -\frac{1}{2} \langle \vec{d} - \vec{h}(\vec{\theta}) | \vec{d} - \vec{h}(\vec{\theta}) \rangle, \quad (5.1)$$

where $\vec{h}(\vec{\theta})$ represents the GW waveform as a function of the source parameters $\vec{\theta}$ and $\langle . | . \rangle$ denotes the noise-weighted inner product defined in chapter 2 (Eq. (2.3)). Expanding the inner product in Eq. (5.1), we get:

$$\ln \mathcal{L}(\vec{\theta}) = \langle \vec{d} | \vec{h} \rangle - \frac{1}{2} \langle \vec{h} | \vec{h} \rangle - \frac{1}{2} \langle \vec{d} | \vec{d} \rangle. \quad (5.2)$$

Likelihood-based inference involves calculating the inner products for a large number of values for $\vec{\theta}$ to explore the parameter space, which is computationally expensive. A rapid way to compute these quantities could enable a faster inference.

Let us introduce the notations:

$$\ln \mathcal{L}_{dh} \equiv \langle \vec{d} | \vec{h} \rangle, \quad (5.3)$$

$$\ln \mathcal{L}_{hh} \equiv \langle \vec{h} | \vec{h} \rangle, \quad (5.4)$$

to rewrite Eq. (5.2) as;

$$\ln \mathcal{L}(\vec{\theta}) = \ln \mathcal{L}_{dh} - \frac{1}{2} \ln \mathcal{L}_{hh}. \quad (5.5)$$

Note that we dropped the last term of Eq. (5.2) in the equation above. It is also known as the noise log likelihood. Since it does not depend on the source parameters, it needs to be computed once for the data.

Dominant mode and aligned spin

When performing parameter estimation, we are interested in knowing the shape of the likelihood around its peak. In other words, we want to evaluate the likelihood for waveforms that are *similar* to the waveform at which the likelihood peaks. If we choose a fiducial value of $\vec{\theta}$ which is close enough to the peak, we can approximate the likelihood by expanding it around the fiducial value. Let us denote the fiducial source parameters by $\vec{\theta}'$ and the waveform at the fiducial parameters by \vec{h}' . For any proposal waveform \vec{h} , under the assumption that \vec{h} and \vec{h}' are close enough, we can find frequency bins $b = [f_{min}, f_{max}]$ such that the ratio \vec{h}/\vec{h}' can be linearly approximated as:

$$\frac{h}{h'}(f) = r_1(b) + r_2(b)(f - f_c(b)) + \mathcal{O}(f^2), \quad (5.6)$$

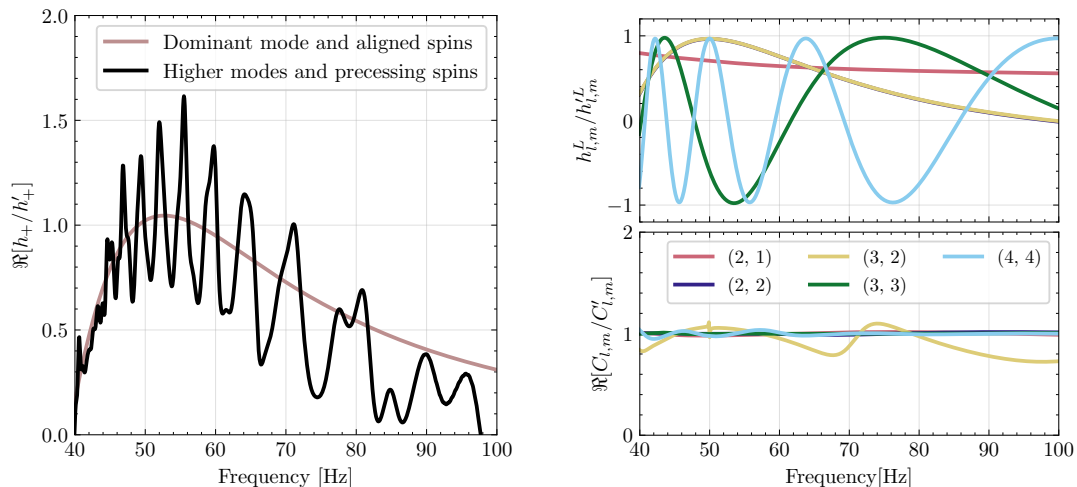


Figure 5.1: *Left*: Ratio of the real part of the proposal to the fiducial waveform for the plus polarisation as a function of frequency. The waveform model corresponding to the brown curve contains only the dominant mode and the aligned spins description of the system. Whereas the one corresponding to the black curve presents a more complete description, including contributions from higher-order modes and allowing for precessing spins (referred to as IMRPhenomXPHM). The ratio for the latter fluctuates more due to the increased complexity of the model. *Right*: Decomposition of IMRPhenomXPHM waveform into the component modes in the co-precessing frame (top right) and precession coefficients (bottom right). Each mode is marked with a different colour. The decomposition makes the ratios smoother, allowing for an efficient implementation of the relative binning method.

within a given bin, where $r_1(b)$ and $r_2(b)$ are expansion coefficients and f_c denotes the central value of the frequency bin b .

The approximation made in Eq. (5.6) performs better for the waveforms that only include the dominant mode, also known as the (2, 2) mode, and aligned spins description. In the phenomenological waveform family, they are known as IMRPhenomD waveforms. For more complete waveforms, i.e. the ones including the effects of higher order modes and precessing spins (known as IMRPhenomXPHM), the ratio \vec{h}/\vec{h}' fluctuates rapidly as a function of frequency (see left plot of Figure 5.1). When using the IMRPhenomD waveform, a few bins are sufficient to make the linear expansion from Eq. (5.6) precise in each bin. When using the IMRPhenomXPHM waveform, as the ratio is subject to more fluctuation, we need to consider a larger number of bins, increasing the waveform generation cost which is the most expensive operation in the calculation of $\ln \mathcal{L}_{dh}$ and $\ln \mathcal{L}_{hh}$.

5.1.1 Inclusion of higher order modes and precessing spins

To make the approximation in Eq. (5.6) robust for precessing waveforms with higher order modes, let us express the detector frame waveform for given $\vec{\theta}$ into its component modes [30];

$$h(f) = \sum_{l,m} (F_+ C_{l,m}^+(f) + F_\times C_{l,m}^\times(f)) h_{l,m}^L(f). \quad (5.7)$$

Here, F_+ and F_\times are the antenna pattern functions of the interferometer, which depend only on extrinsic parameters; \vec{h}^L denotes the waveform in the co-precessing frame (also known as the L -frame);

and the indices l and m label the different modes. The L -frame is the frame whose z -axis is chosen along the orbital angular momentum of the system. The coefficients $C_{l,m}^+$ and $C_{l,m}^\times$ account for the *twisting-up* procedure, which transforms the waveform from a co-precessing frame to the inertial (or observer) frame [30]. The benefit of handling each mode in the L -frame separately is that the ratio of a fiducial $\vec{h}'_{l,m}$ to a proposal $\vec{h}_{l,m}$ oscillates less compared to the ratio of the full waveforms \vec{h}/\vec{h}' . This can be seen by comparing the left plot of the Figure 5.1 with the two plots in the right panel of it. Therefore, a linear expansion similar to the one in Eq. (5.6) can be made using the ratio $\vec{h}_{l,m}^L/\vec{h}'_{l,m}$ instead of \vec{h}/\vec{h}' and will require a lower number of frequency bins;

$$\frac{h_{l,m}^L}{h'_{l,m}}(f) = r_{1,l,m}(b) + r_{2,l,m}(b)(f - f_c(b)) + \mathcal{O}(f^2), \quad (5.8)$$

Now, let us denote the factors $(F_+ C_{l,m}^+(f) + F_\times C_{l,m}^\times(f))$ in Eq. (5.7) by $\vec{C}_{l,m}$. We can perform similar expansions on the ratios $\vec{C}_{l,m}/\vec{C}'_{l,m}$:

$$\frac{C_{l,m}}{C'_{l,m}}(f) = s_{1,l,m}(b) + s_{2,l,m}(b)(f - f_c(b)) + \mathcal{O}(f^2). \quad (5.9)$$

Below, the expansion coefficients will collectively be denoted $\mathcal{R} = \{\vec{r}_1, \vec{r}_2, \vec{s}_1, \vec{s}_2\}$. For now, we assume we can find frequency bins such that the piece-wise linear interpolations in Eq. (5.8) and Eq. (5.9) are valid. I explain how we construct such bins in section 5.1.2.

Once the frequency bins are made based on a fiducial waveform, we can pre-compute some *summary data* which is useful for the computation of the inner products in Eq. (5.5) [71]. Specifically, the expressions for the summary data are:

$$\begin{aligned} W_{l,m}(b) &= \frac{4}{T} \sum_{f \in b} \frac{d(f) h_{l,m}^{\prime L*}(f) C_{l,m}^{\prime*}(f)}{S_n(f)}, \\ X_{l,m}(b) &= \frac{4}{T} \sum_{f \in b} \frac{d(f) h_{l,m}^{\prime L*}(f) C_{l,m}^{\prime*}(f)}{S_n(f)} (f - f_c(b)), \\ Y_{l,m,\bar{l},\bar{m}}(b) &= \frac{4}{T} \sum_{f \in b} \frac{h_{l,m}^{\prime L}(f) C'_{l,m}(f) h_{\bar{l},\bar{m}}^{\prime L*}(f) C_{\bar{l},\bar{m}}^{\prime*}(f)}{S_n(f)}, \\ Z_{l,m,\bar{l},\bar{m}}(b) &= \frac{4}{T} \sum_{f \in b} \frac{h_{l,m}^{\prime L}(f) C'_{l,m}(f) h_{\bar{l},\bar{m}}^{\prime L*}(f) C_{\bar{l},\bar{m}}^{\prime*}(f)}{S_n(f)} (f - f_c(b)). \end{aligned} \quad (5.10)$$

Note that the summary data, collectively denoted by $\mathcal{D} \equiv \{W_{l,m}, X_{l,m}, Y_{l,m,\bar{l},\bar{m}}, Z_{l,m,\bar{l},\bar{m}}\}$ need to be computed only once per analysis, and they depend only on the choice of the fiducial parameters $\vec{\theta}'$. On the other hand, the coefficients \mathcal{R} need to be computed for every proposal waveform as they depend on $\vec{\theta}$ and $\vec{\theta}'$.

Using the summary data \mathcal{D} and the coefficients \mathcal{R} , we can estimate $\ln \mathcal{L}_{dh}$ and $\ln \mathcal{L}_{hh}$ in Eq. (5.5)

for given $\vec{\theta}$ as,

$$\ln \mathcal{L}_{dh} = \Re \sum_{(l,m)} \sum_b \left\{ W_{l,m}(b) \left[r_{1,l,m}^*(b) s_{1,l,m}^*(b) \right] + X_{l,m}(b) \left[r_{1,l,m}^*(b) s_{2,l,m}^*(b) + r_{2,l,m}^*(b) s_{1,l,m}^*(b) \right] \right\}, \quad (5.11)$$

$$\begin{aligned} \ln \mathcal{L}_{hh} = \Re \sum_{(l,m),(\bar{l},\bar{m})} \sum_b \left\{ Y_{l,m,\bar{l},\bar{m}}(b) \left[r_{1,l,m}(b) s_{1,l,m}(b) r_{1,\bar{l},\bar{m}}^*(b) s_{1,\bar{l},\bar{m}}^*(b) \right] \right. \\ \left. + Z_{l,m,\bar{l},\bar{m}}(b) \left[r_{1,l,m}(b) r_{1,\bar{l},\bar{m}}^*(b) \left(s_{1,\bar{l},\bar{m}}^*(b) s_{2,l,m}(b) + s_{1,l,m}(b) s_{2,\bar{l},\bar{m}}^*(b) \right) \right] \right. \\ \left. + s_{1,l,m}(b) s_{1,\bar{l},\bar{m}}^*(b) \left(r_{1,\bar{l},\bar{m}}^*(b) r_{2,l,m}(b) + r_{1,l,m}(b) r_{2,\bar{l},\bar{m}}^*(b) \right) \right\}, \quad (5.12) \end{aligned}$$

which together with Eq. (5.5) enables us to approximate the likelihood. Provided the number of bins is reduced compared to the exact method, this approach should offer a rapid likelihood evaluation, leading to a faster parameter inference.

5.1.2 Constructing the relative binning grid

The objective of the bin selection step is to identify a minimal set of frequency bins in which the ratios of proposal waveform components. ($\vec{h}_{l,m}^L$ and $\vec{C}_{l,m}$) to fiducial waveform components are linear to a sufficient approximation. We refer to a set of frequency bins which satisfy this condition as an RBGrid. The RBGrid is used to compute the summary data \mathcal{D} , and, once the sampling begins, to compute coefficients \mathcal{R} for the points in parameter space proposed by the sampler.

To initialise the bin selection algorithm, we need the following quantities: a uniform frequency grid with spacing $\Delta f = 1/T$, where the time T is sufficiently long to accommodate the length of the signal easily; a fixed value of “total error” on log likelihood, ϵ ; an initial value N_0 for the total number of frequency bins; a set of fiducial waveform parameters; and a set of test parameters. For definiteness, we set $\epsilon = 0.01$ and $N_0 = 200$. In simulations, the fiducial parameters are set to the injection parameters, while for real events, they are set to the maximum likelihood parameters obtained from earlier analyses. To choose a set of test parameters, we perturb the chirp mass and the mass ratio of the fiducial parameters by a random relative value in a $[-10\%, 10\%]$ interval, and the rest of the parameters are kept the same.

Using the quantities described in the paragraph above, we construct the RBGrid as follows. We start from the first bin of the uniform frequency grid. We merge the first bin with the next one and calculate the partial relative binning log likelihoods $\ln \mathcal{L}_{dh}$ and $\ln \mathcal{L}_{hh}$ defined in Eq. (5.11) and Eq. (5.12), using as test quantities the edges of the combined frequency bin, and the fiducial waveform parameters. We also compute the corresponding exact partial likelihoods obtained by using all frequencies within the bins and not just the edges. If the absolute difference between the partial relative binning likelihoods and the exact partial likelihoods is less than $\epsilon/\sqrt{N_0}$, we add a subsequent bin into it and repeat. If the difference is larger than that, we do not add any more bins and move to the next bin and repeat. This continues until the maximum frequency of the uniform grid is reached. The value of N_0 is then updated to the total number of bins obtained through the above process, and the same procedure is started again with the same ϵ but with the updated N_0 . The algorithm terminates when N_0 ceases to change, and the edges of the merged bins in the final iteration become the RBGrid.

The choice of ϵ controls the trade-off between speed and accuracy, where a larger value increases speed but reduces accuracy. By contrast, we have verified that the bin selection procedure is not very sensitive to the initial value of N_0 ; it mainly affects the convergence rate of the algorithm. Setting N_0 equal to the length of the uniform grid would eliminate the need for this additional tuning parameter, but this would slow down the bin selection algorithm as a whole.

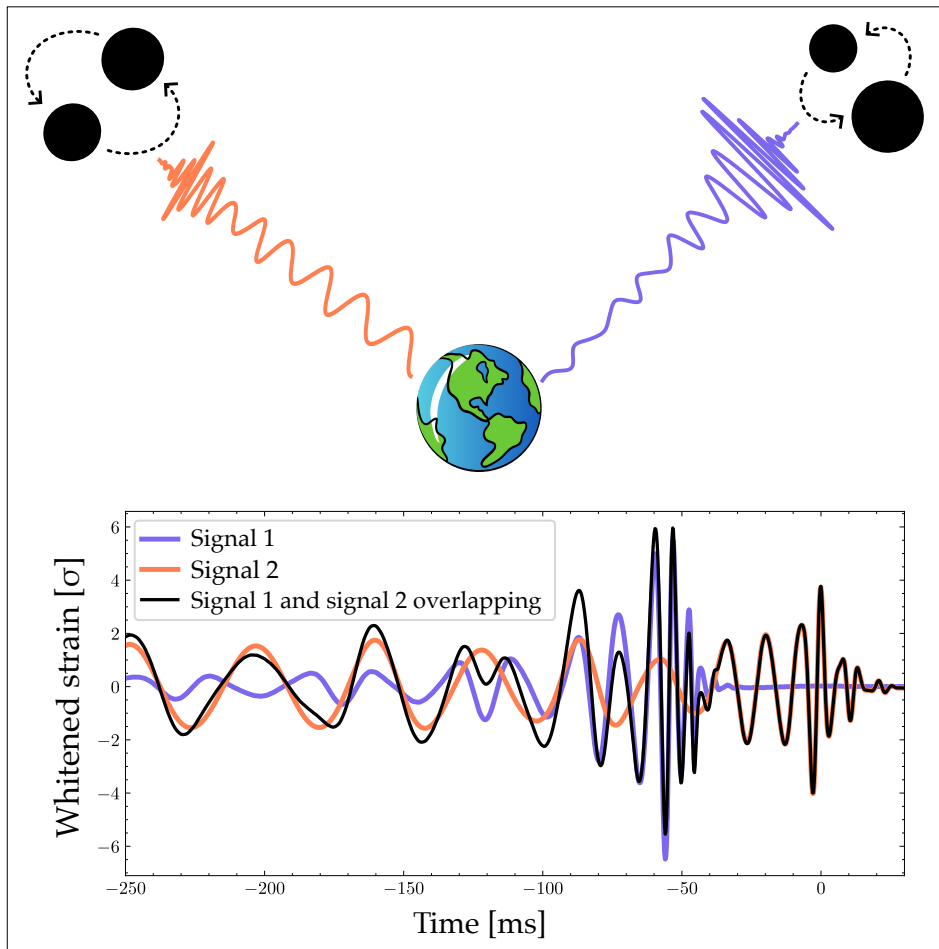


Figure 5.2: An illustration of two gravitational wave signals (blue and orange) arriving at the Earth at nearly the same time. At the Earth based GW detector, we can only measure the sum of the two (black line).

5.2 Extension of the relative binning method

A fast parameter estimation method has a wide range of applications. Here, we focus on two of them, overlapping signals analysis and strong lensing searches. Specifically, we extend the relative binning method to perform parameter estimation on overlapping signals and to perform strong lensing searches. The two applications are similar in the sense that they both require a framework that can perform *joint* parameter estimation on two signals.

5.2.1 Extension to perform parameter estimation on the overlapping signals

Overlapping signals refer to a phenomenon where the arrival times of two (or more) GW signals are close to each other. Figure 5.2 shows an illustration of two overlapping GW signals. While such scenarios are less likely for the LIGO-Virgo interferometers, they may occur frequently for 3G detectors. Due to their increased baseline sensitivity, the 3G detectors are expected to detect ≈ 1 signal per minute, with longer in-band duration of the signals. These two factors, increased detection rate and increased in-band duration, may cause GW signals to overlap with each other. Current rate estimates suggest that we may see up to 20,000 cases per year where two GW signals are overlapping within ≈ 1 second of each other [72]. If the two signals are close to each other, we may need to analyse them jointly to measure their source parameters, i.e., we may need to perform *joint* parameter estimation on them. Indeed, the joint parameter estimation on two signals can be computationally more expensive compared to analysing a single signal since the dimension of the space is doubled. Here, we demonstrate how relative binning can be used to speed up joint parameter estimation.

We account for two signals in the signal model by replacing \vec{h} by $\vec{h}_1 + \vec{h}_2$ in the expression of the likelihood (see Eq. (5.1)). This leads to;

$$\ln \mathcal{L}(\vec{\theta}_1, \vec{\theta}_2) = -\frac{1}{2} \left\langle \vec{d} - \vec{h}_1(\vec{\theta}_1) - \vec{h}_2(\vec{\theta}_2) \middle| \vec{d} - \vec{h}_1(\vec{\theta}_1) - \vec{h}_2(\vec{\theta}_2) \right\rangle, \quad (5.13)$$

where the set $\{\vec{\theta}_1, \vec{\theta}_2\}$ now represent a 30 dimensional parameter space. Following the steps from Eq. (5.1)-(5.5), we can factorise the likelihood into;

$$\begin{aligned} \ln \mathcal{L}(\vec{\theta}) &\approx \left\langle \vec{d} \middle| \vec{h}_1 \right\rangle - \frac{1}{2} \left\langle \vec{h}_1 \middle| \vec{h}_1 \right\rangle + \left\langle \vec{d} \middle| \vec{h}_2 \right\rangle - \frac{1}{2} \left\langle \vec{h}_2 \middle| \vec{h}_2 \right\rangle, \\ &= \ln \mathcal{L}_{dh_1} - \frac{1}{2} \ln \mathcal{L}_{h_1h_1} + \ln \mathcal{L}_{dh_2} - \frac{1}{2} \ln \mathcal{L}_{h_2h_2}. \end{aligned} \quad (5.14)$$

where we have ignored the overlaps between \vec{h}_1 and \vec{h}_2 under the assumption that the two signals are sufficiently different, resulting in negligible overlaps. Each term in the factorised likelihood expression of Eq. (5.14) can be calculated using the relative binning approximation. To construct the RBGrid, we repeat the bin selection algorithm from section 5.1.2 two times; once for each signal.

5.2.2 Extension to perform strong lensing searches

When gravitational waves encounter a massive object in their path, they may undergo gravitational lensing, i.e., suffer a deflection from their original path. In the case of strong lensing, the GW signal is split into multiple time-separated copies (referred to as images), which may be observed at the detectors. Figure 5.3 gives an illustration of a GW signal being strongly lensed by a massive object and producing two images. Each image produced by strong lensing may be (de-)magnified, may suffer a constant phase shift (also known as the Morse phase [73]), and may arrive at Earth at different times. Strong lensing does not affect the frequency evolution of the source. Therefore, we can perform strong lensing searches by quantifying how similar any two signals are, i.e., by jointly analysing two signals to measure the coherence between their source parameters.

Similar to the joint parameters estimation of the overlapping signals, we need to account for two images, \vec{h}_1 and \vec{h}_2 . However, we do not simply replace \vec{h} by $\vec{h}_1 + \vec{h}_2$. The two images are copies of

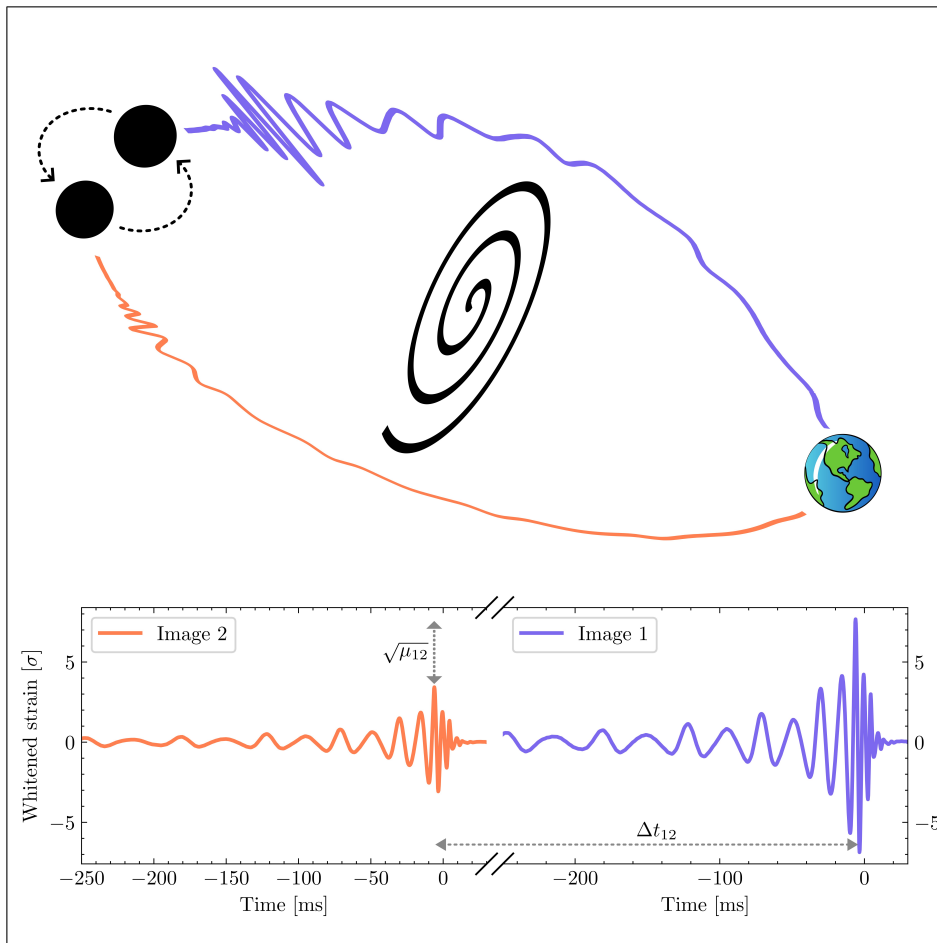


Figure 5.3: An illustration of a gravitational wave signal that is strongly lensed by a heavy object in its path and producing two images. Each image may be (de-)magnified and arrive at the Earth at different times. The fiducial time separation between the two images is marked by Δt_{12} , and relative (de-)magnification is marked by μ_{12} . The precise values of them depend on the relative configuration of the GW source and the lens.

the same GW signal; we expect that the source parameters are identical between the two, except for the arrival time at Earth, apparent luminosity distance, and Morse phase. Therefore, we only need to introduce three additional parameters. We denote them by $\vec{\theta}_L \equiv \{\Delta t_{12}, \mu_{12}, \Delta n_{12}\}$. The signal model corresponding to the second image \vec{h}_2 can be expressed in terms of the \vec{h}_1 and $\vec{\theta}_L$ as

$$\vec{h}_2(\vec{\theta}, \vec{\theta}_L) = \sqrt{\mu_{12}} \vec{h}_1(\vec{\theta}) e^{2i\pi f \Delta t_{12} - i\Delta n_{12} \pi}, \quad (5.15)$$

where the set $\{\vec{\theta}, \vec{\theta}_L\}$ now represent a 18 dimensional parameter space. The factorisation of the likelihood expression is slightly different from the case of overlapping signals since we need to incorporate two data segments, \vec{d}_1 and \vec{d}_2 , one for each image. The full likelihood expression becomes [74];

$$p(\vec{d}_1, \vec{d}_2 | \vec{\theta}, \vec{\theta}_L) = p(\vec{d}_1 | \vec{\theta}) p(\vec{d}_2 | \vec{\theta}, \vec{\theta}_L), \quad (5.16)$$

which holds since two data segments are disjoint and \vec{d}_1 do not depend on the relative lensing param-

eters $\vec{\theta}_L$. We can factorise it into

$$\begin{aligned}\ln \mathcal{L}(\vec{\theta}, \vec{\theta}_L) &= \langle \vec{d}_1 | \vec{h}_1 \rangle - \frac{1}{2} \langle \vec{h}_1 | \vec{h}_1 \rangle + \langle \vec{d}_2 | \vec{h}_2 \rangle - \frac{1}{2} \langle \vec{h}_2 | \vec{h}_2 \rangle, \\ &= \ln \mathcal{L}_{d_1 h_1} - \frac{1}{2} \ln \mathcal{L}_{h_1 h_1} + \ln \mathcal{L}_{d_2 h_2} - \frac{1}{2} \ln \mathcal{L}_{h_2 h_2}.\end{aligned}\quad (5.17)$$

The overlaps between \vec{h}_1 and \vec{h}_2 do not appear here, unlike the overlapping signals analysis. Next, we construct the RBGrid only for image 1 and use the same grid to generate image 2 waveform (see Eq. (5.15)). We use the RBGrid to generate the summary data, and then, using the summary data, we can approximate the likelihood.

Now, we have all the ingredients to perform parameter estimation on the isolated signals, overlapping signals, and strongly lensed signals using the relative binning method. Our aim here is to demonstrate that the relative binning approximation significantly decreases the computation cost without compromising on the accuracy. Before we perform the analysis and present the results let us discuss the quantities used to compare the accuracy of the exact method with the relative binning method.

Checking the efficiency

Reweighting the relative binning posterior samples: Ideally, we want to compare the posterior samples obtained using exact likelihood and the relative binning likelihood. However, there may be cases when the exact computation is too expensive to carry out and we can only perform the analysis with relative binning likelihood. For such cases, we reweight the posterior samples produced using relative binning to produce the samples which may be obtained with the exact likelihood computations. This step helps test the method's efficiency. Let us denote the likelihood evaluated for the posterior samples produced by the relative binning method by $\mathcal{L}^{\text{RB}}(\vec{\theta})$, where $\vec{\theta}$ stands for the posterior samples; and the probability for $\vec{\theta}$ according to the relative binning samples by $p^{\text{RB}}(\vec{\theta})$. To perform the reweighting, for each posterior sample $\vec{\theta}$, we compute the likelihood according to the exact method, which we denote by $\mathcal{L}^{\text{X}}(\vec{\theta})$. Using $\mathcal{L}^{\text{RB}}(\vec{\theta})$, $\mathcal{L}^{\text{X}}(\vec{\theta})$, we reweigh $p^{\text{RB}}(\vec{\theta})$ to obtain the probability for $\vec{\theta}$ according to the exact method:

$$p^{\text{X}}(\vec{\theta}) = \frac{\mathcal{L}^{\text{X}}(\vec{\theta})}{\mathcal{L}^{\text{RB}}(\vec{\theta})} p^{\text{RB}}(\vec{\theta}). \quad (5.18)$$

Jensen-Shannon divergence: Once we have the posterior samples from the exact method (either by performing exact analysis or by reweighting), we quantify the similarities between the two using the Jensen-Shannon (JS) divergence [75]. The JS divergence yields a finite value between 0nat and 1nat. A value closer to 0nat corresponds to greater similarity between two distributions. If we denote the two distributions we want to compare by p and q , then the JS divergence is given by

$$\text{JS}(p||q) = \frac{1}{2} (D(p||m) + D(q||m)), \quad (5.19)$$

where D is the Kullback-Leibler divergence [76] and m is the pointwise mean of p and q . The JS divergence is symmetric in p and q .

Kolmogorov-Smirnov test: Alternatively, we also use the Kolmogorov-Smirnov (KS) test to perform sanity checks [77]. This test is useful to determine if the parameter estimation on a large set

of simulated GW signals is not biased in any particular direction. If the parameter estimation on a large set of simulated signals is not biased, the percentile at which the true value is found should follow a uniform distribution over the population. In this regard, the KS test helps determine if the distribution of percentiles follows a uniform distribution. The KS test returns a p -value which can be used to reject the null hypothesis, i.e., the percentiles follow a uniform distribution. We use the standard routines from SciPy codebase to calculate the JS divergence and KS statistic.

5.3 Validation of the method by performing parameter estimation

Next, we demonstrate the speed and accuracy with which our method can perform parameter inference. We analyse a large set of GW signals consisting of simulated signals, signals detected by LIGO-Virgo, lensed signals, and overlapping signals.

5.3.1 Validation on simulated events: analysing GW signals in Gaussian noise

For a parameter estimation method to be trustworthy, it should recover the injected parameters within a given confidence interval for a corresponding fraction of injections; the extent to which it does so can be assessed using a so-called P-P plot [21,22]. To this end, we simulate a population of 70 BBH signals by sampling the appropriate source parameters from the prior distributions specified in Table 5.1. We adjust the luminosity distance in such a way that each event has a network SNR above 13. The network consists of the two LIGO and the Virgo interferometers at their design sensitivity [78]. We perform parameter estimation on each event and show the collective results in Figure 5.4, representing a P-P plot for our relative binning framework. Ideally, each coloured line should trace the diagonal; however, some fluctuations are expected due to a finite number of signals being analysed and the presence of noise. We perform a KS test as a measure of the consistency between each coloured line and the diagonal line. We quote the p -value of this test for each parameter in the bracket. Additionally, we also test if the distribution of all p -values quoted in the brackets follows a uniform distribution. The combined p -value for this test is 0.6625, which is expected. To further quantify this consistency, we can define a binomial random variable X as the number of times the injected value is recovered within a confidence interval corresponding to a value on the horizontal axis. For this binomial distribution, the shape parameter N equals 70 and p equals the confidence corresponding to the x -axis. The shaded regions in Figure 5.4 cover 1σ , 2σ , and 3σ confidence intervals of the binomial probability distribution in decreasing order of opacity. As all the plotted curves for the different parameters fall within the 3σ boundary and the accompanying p -values indicate good consistency with the diagonal, we conclude that our method is robust.

5.3.2 Validation on real data: analysing GW signals detected by LIGO-Virgo interferometers

Next, we turn to parameter estimation on the events detected by LIGO-Virgo. We choose GW190412, GW190814, GW191103, and GW191105. The first two events are chosen as they consist of BBHs with highly asymmetric masses. This feature allows for a significant contribution from the higher

Parameter	Population Prior
Chirp mass (\mathcal{M}_c)	Uniform($5M_\odot, 100M_\odot$)
Mass ratio (q)	Uniform(0.1, 10)
Dimensionless spin of the i^{th} black hole (a_i)	Uniform(0, 1)
Zenith angle between the spin and orbital angular momentum for i^{th} black hole (θ_i)	Sine(0, π)
Difference between the azimuthal angles of the individual spin vector projections onto the orbital plane ($\Delta\phi$)	Uniform(0, 2π)
Difference between total and orbital angular momentum azimuthal angles (ϕ_{JL})	Uniform(0, 2π)
Right Ascension (RA)	Uniform(0, 2π)
Declination (DEC)	Cosine($-\pi/2, \pi/2$)
Angle between the line of sight and total angular momentum (θ_{JN})	Sine(0, π)
Polarization angle (ψ)	Sine(0, π)
Phase of coalescence (ϕ_c)	Uniform(0, 2π)
Luminosity distance (d_L)	UniformSourceFrame(0.1 Gpc, 5 Gpc)
Time of coalescence (t_c)	Uniform(0s, 86400s)
Morse factor for image 1 (n_1)	Uniform{0, 0.5, 1}
Magnification of image 2 w.r.t image 1 (μ_{12})	Uniform(0, 10)
Delay in arrival time between two images (Δt_{12})	Uniform(0s, 86400s)
Difference in Morse factor (Δn_{12})	Uniform{0, 0.5, 1}

Table 5.1: Parameters and corresponding priors used to simulate individual GW signals and the pairs of lensed GW signals.

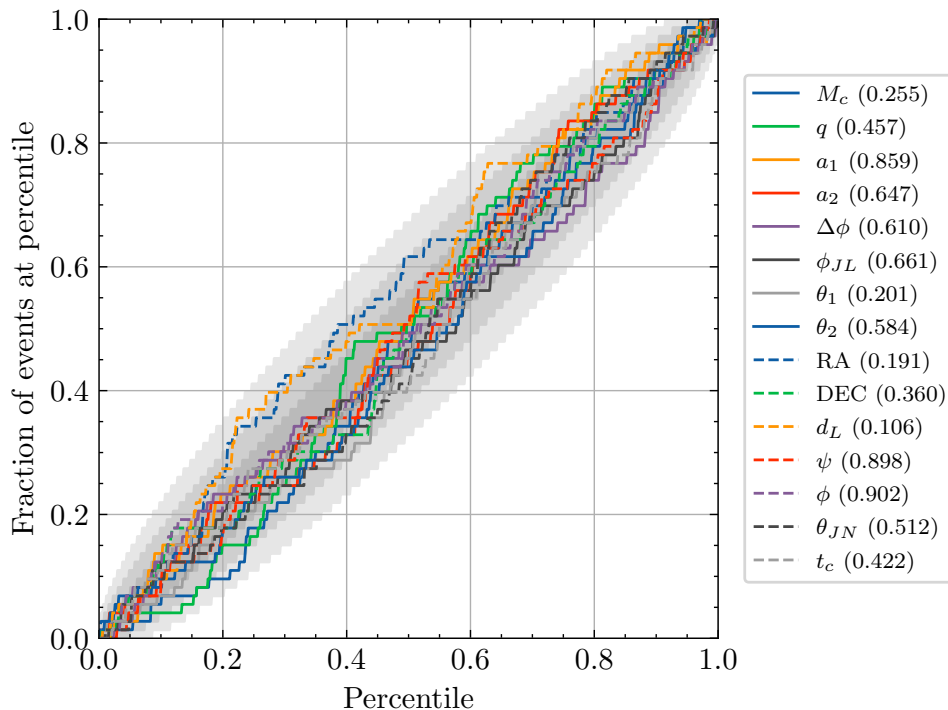


Figure 5.4: Percentile-percentile showcasing the robustness of the relative binning method on simulated BBH signals. Each line traces the diagonal, indicating that the parameter corresponding to it is recovered with expected accuracy. The numbers in the brackets of the legend show the p-values of the KS tests. The combined p-value of all parameters is 0.6625, consistent with the hypothesis that individual p-values were derived from a uniform distribution as expected. The shaded regions show 1σ , 2σ , and 3σ confidence intervals in decreasing order of opacity.

harmonics [69], enabling us to stress-test our framework. The remaining two events were chosen because they were part of a candidate event pair from the strong lensing searches [63, 79].

For GW190412 and GW190814, a truncated corner plot showing posterior distributions for selected parameters is presented in Figures 5.5 and Figure 5.6, respectively. The blue (grey) curves represent the results of parameter estimation with (without) relative binning. The grey curves are generated by using the posterior samples provided in the public data release of the LVK collaboration [80, 81]. Figures 5.5 and 5.6 show a qualitative agreement between the posterior distributions obtained by the exact method (without making any approximation) and the relative binning method. Similarly, we analysed GW191103 and GW191105 with the relative binning method, which led to a comparable agreement with the exact method.

To quantify the mismatch between the posterior samples obtained using the relative binning method and the ones obtained with the exact method, we use the JS divergence. We do not perform an exact parameter estimation run due to the computational cost. Instead, we reweigh the posterior samples obtained using the relative binning method to obtain the posterior samples for the exact method as discussed in the next paragraph. We repeat this step for all four events, GW190412, GW190814, GW191103, and GW191105, and plot the JS divergence between the relative binning samples and the exact samples for each parameter in Figure 5.7. Each event is represented by a

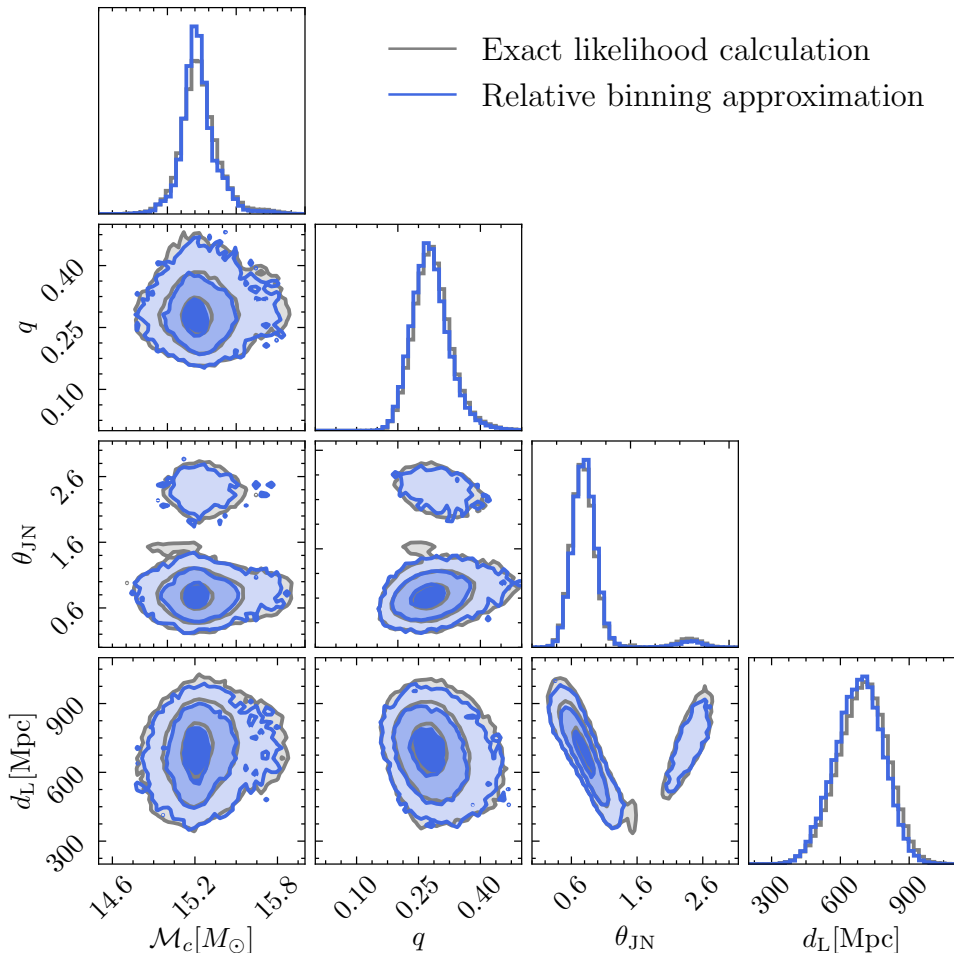


Figure 5.5: The parameter measurements obtained using the relative binning framework (blue curves) are consistent with the ones reproduced from the public data release of the LVK collaboration (grey) for GW190412.

different coloured marker. To determine a heuristic threshold value for statistical indistinguishability (represented by the dashed line in Figure 5.7), we compute the JS statistic for 2000 pairs of sets of 10^5 samples taken from Gaussian distributions. We then use the 99th percentile of the obtained values as the heuristic threshold for indistinguishability. The JS divergence for each parameter remains well below the threshold, indicating that the posterior distributions produced by the relative binning method and the exact method are statistically indistinguishable. As an additional validation test, we use the posterior samples obtained through the relative binning method on the GW190412, GW190814, GW191103, and GW191105 events to compute the exact likelihoods (i.e. Eq. (5.5)). The standard deviation of the absolute difference between the exact and the relative binning likelihoods turns out to be ≤ 0.1 , which indicates that the error incurred by the relative binning likelihood is sufficiently small to not impact the posterior distribution [71].

5.3.3 Validation on the parameter estimation of 3G-era events

To further test our method, we analyse a subset of LIGO-Virgo events as they would appear in 3G interferometers. We also analyse an example of overlapping signals.

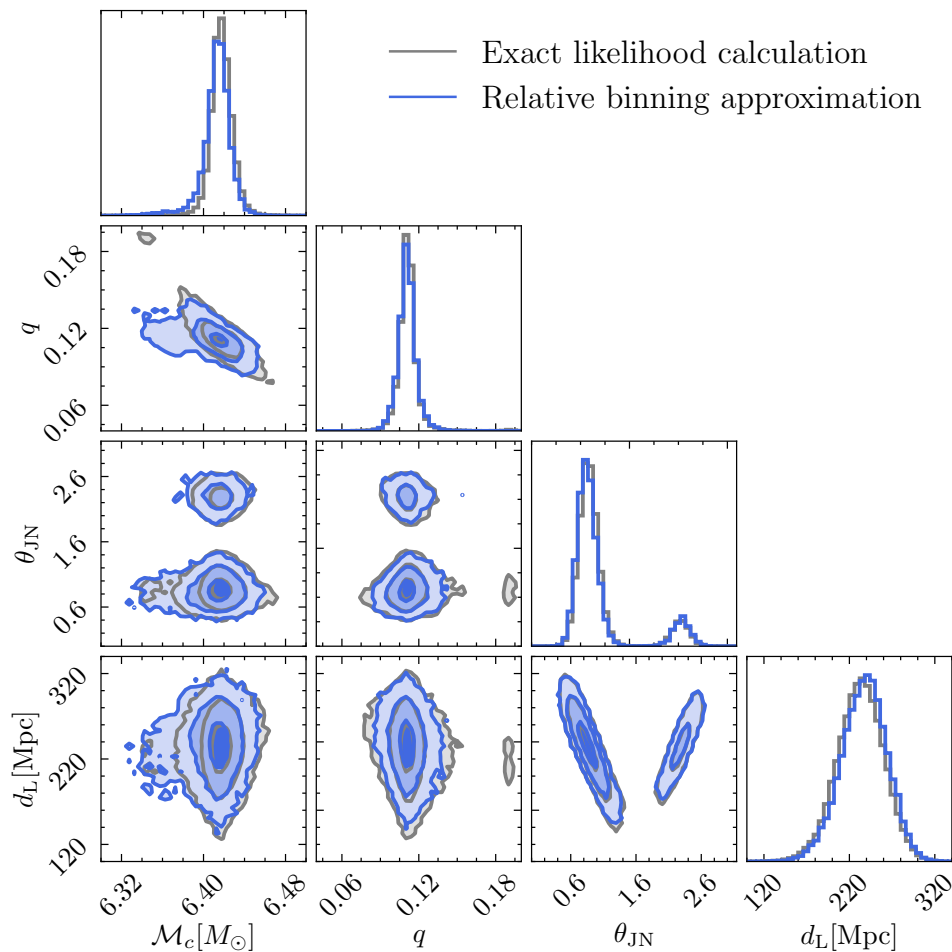


Figure 5.6: The parameter measurements obtained using the relative binning framework (blue curves) are consistent with the ones reproduced from the public data release of the LVK collaboration (grey curves) for GW190814.

Specifically, for the isolated signals, we use the maximum likelihood parameters obtained from the posterior samples of the LIGO-Virgo events. We then simulate a GW signal using the maximum likelihood parameters and add it to the simulated Gaussian noise of the 3G interferometers. The high sensitivities of the 3G interferometers lead to significantly louder SNRs. We then analyse the simulated data with the relative binning framework. We arbitrarily choose six events with varying total masses, specified in Table 5.2.

Our detector network consists of a triangular ET with an arm length of 10 km [20] and one L-shaped CE with an arm length of 40 km [15]. The noise curves and detector configurations are obtained from [82]. The starting frequency for our analysis is 5 Hz. A representative, truncated corner plot for this analysis is shown in Figure 5.8 for the GW200220_061928 event. The black lines in the plot show the injected parameter values. The 1σ , 2σ , and 3σ confidence contours are indicated by the blue shading, in order of decreasing opacity. As can be seen from the plot, all injected parameters have been recovered well.

To quantify the accuracy of our method for the 3G scenario, we again reweigh the posterior

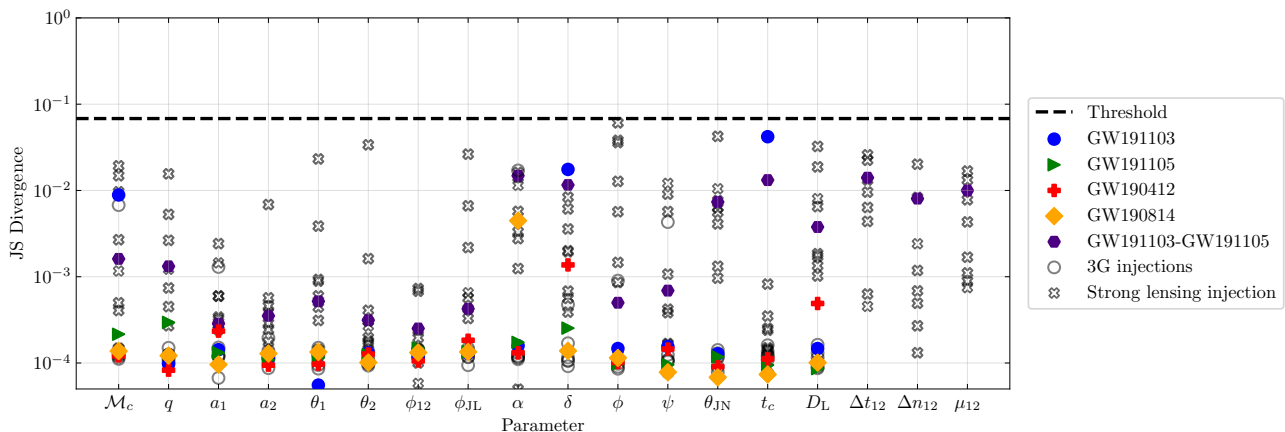


Figure 5.7: JS divergence values to quantify if the measurements made using the relative binning method are in agreement with the ones made using exact computation. The black line marks the JS divergence below which the two measurements are indistinguishable. The plot contains the JS divergence values for all parameters for all signals, simulated as well as real, analysed in this chapter. For compactness, we use the same marker for the set of 3G signals (circles) and for the set of lensed signals (crosses). We use different coloured markers for LIGO-Virgo events. All JS divergence values remain below the threshold, indicating that measurements obtained using the relative binning method are reliable.

samples obtained using the relative binning method following the reweighting procedure discussed in Section 5.2.2. Then, we calculate the JS divergence between the reweighted samples and the relative binning samples. This process is repeated for each of the six events and the results are shown in Figure 5.7. For compactness, we use the circle makers for all events and all parameters since our aim here is to test if JS divergences for any of them crosses the threshold. Again, the JS divergence for each parameter remains well below the threshold, indicating that the posterior distributions produced by the relative binning method and the exact method are statistically indistinguishable.

Overlapping signals example

We collectively present the results for overlapping signals analysis in Figure 5.9. Let us refer to the two signals as signal A and signal B. The red (green) lines in the top (bottom) plot show how accurately we can recover signal A (signal B) when they are in isolation. This establishes the benchmark for accuracy. The black lines in the plot show the injected value of the parameters. For this example, we chose two signals with chirp mass of around $22 M_{\odot}$ and $47 M_{\odot}$. The injected value of the remaining parameters can be gauged from the black lines. The blue lines in both plots show the results of joint parameter estimation using the relative binning framework, i.e., how well the parameters of the two signals are recovered when they are overlapping. The agreement of the blue curves with the green and red curves suggests that our relative binning framework can be reliably extended to perform joint parameter estimation when two (or more) GW signals are overlapping.

Event	Total Mass (M_{\odot})	Network SNR
GW191126_115259	26.51	192.52
GW200306_093714	62.10	326.02
GW200112_155838	78.10	1103.53
GW191127_050227	138.71	260.33
GW191230_180458	144.69	383.10
GW200220_061928	282.50	224.91

Table 5.2: Table of events analysed in the context of 3G detectors. The second column shows the maximum likelihood values of the total mass obtained from the public data release of LVK. The third column shows the respective network SNRs if they were observed by a network of 3G detectors. The events were detected by LIGO-Virgo interferometers during their third observation runs, and the naming convention follows the pattern GWYYMMDD_HHMMSS.

5.3.4 Validation on the strongly lensed events

We analyse eight simulated lensed pairs and, additionally, the GW191103–GW191105 event pair to test the relative binning framework for joint parameter estimation. The latter event pair is of interest as it was followed up by strong lensing searches because it showed some prototypical features of galaxy lensing, such as a mild posterior overlap and a short time delay between two images [63, 79]. On the other hand, the simulated pairs were generated by sampling the relevant source parameters from the priors shown in Table 5.1. We adjust the luminosity distance and the relative magnification of each lensed pair to ensure that the network SNR of each image is above 13.

Again, we compute the JS divergence between the posterior distributions obtained using the exact and relative binning methods; see Figure 5.7. Note that, for the lensed injections, we do not use reweighting as was done for the individual parameter estimation cases. Instead, we carry out joint parameter estimation using the exact likelihood [83]. All crosses are below the threshold value, suggesting that the posterior distributions obtained using the exact and relative binning frameworks are statistically indistinguishable. For compactness, we use the cross marker for all 8 pairs and all parameters, since our aim here is to check if the JS divergences remain below the threshold.

Now let us look at joint parameter estimation results for the GW191103–GW191105 pair. In this analysis, GW191103 is treated as image 1, and GW191105 as image 2. The left plot of Figure 5.10 shows a truncated corner plot of the common parameters between the two images, while the right one presents the corner plot of the relative lensing parameters, connecting images 1 and 2. To quantify the accuracy of our results, we follow the same reweighting steps mentioned towards the end of Section 5.2.2 to calculate the JS divergence between the relative binning samples and the exact samples for each parameter. The JS divergences are marked with a hexagon marker in Figure 5.7, which remain all below the threshold.

Besides the JS divergence, we could also check for the overlap between the joint posterior distribution of GW91103–GW191105 obtained using different methods. Specifically, we can compare the joint posterior distribution obtained using the relative binning method and the exact method. The

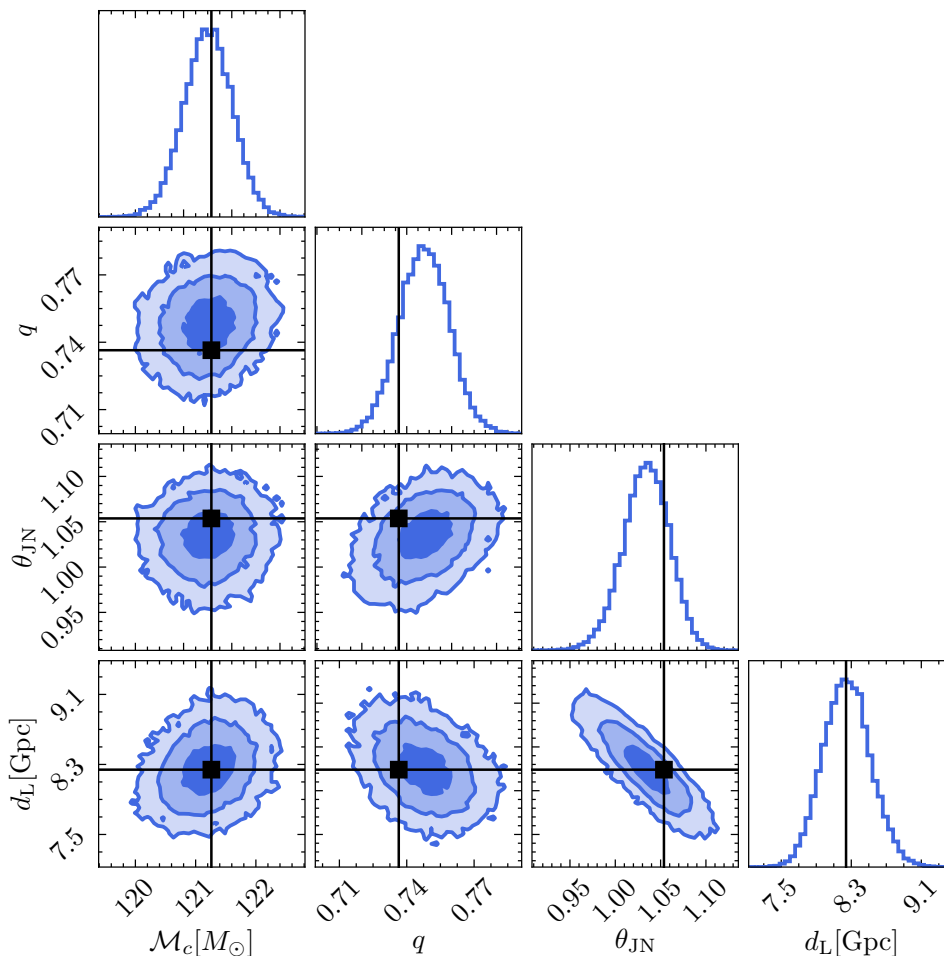


Figure 5.8: A representative corner plot showing the results of parameter estimation on GW200220_061928 using relative binning. The event was observed by LIGO-Virgo interferometers in the third observation run. Here, we analyse a simulated equivalent of it as if it were observed by a network of 3G detectors. The black lines show the true values of the parameters. The blue contours correspond to 1σ , 2σ , and 3σ confidence, in order of decreasing opacity, indicating that all parameters are recovered with expected accuracy.

overlap is quantified using the coherence ratio which is defined as [74, 84]

$$\mathcal{C}_{\text{Unlensed}}^{\text{Lensed}} = \frac{p(\vec{d}_1, \vec{d}_2 | \vec{\theta}, \vec{\theta}_L)}{p(\vec{d}_1 | \vec{\theta}_1) p(\vec{d}_2 | \vec{\theta}_2)}. \quad (5.20)$$

Namely, it is the ratio of evidence (Eq. 2.6) when the data from two images (\vec{d}_1, \vec{d}_2) are jointly analysed under lensed hypothesis to evidence when each event is analysed separately under the unlensed hypothesis. Finally, we report that the (log) of coherence ratio obtained for the GW191103–GW191105 pair is 4.5 [74, 83, 84]. The value is comparable to the one reported by the lensing follow-up searches [79]. Despite the high degree of overlap, the investigations on the pair being strongly lensed remained inclusive due to a large false alarm rate [79].

5.4 Comparison of speed-up and accuracy

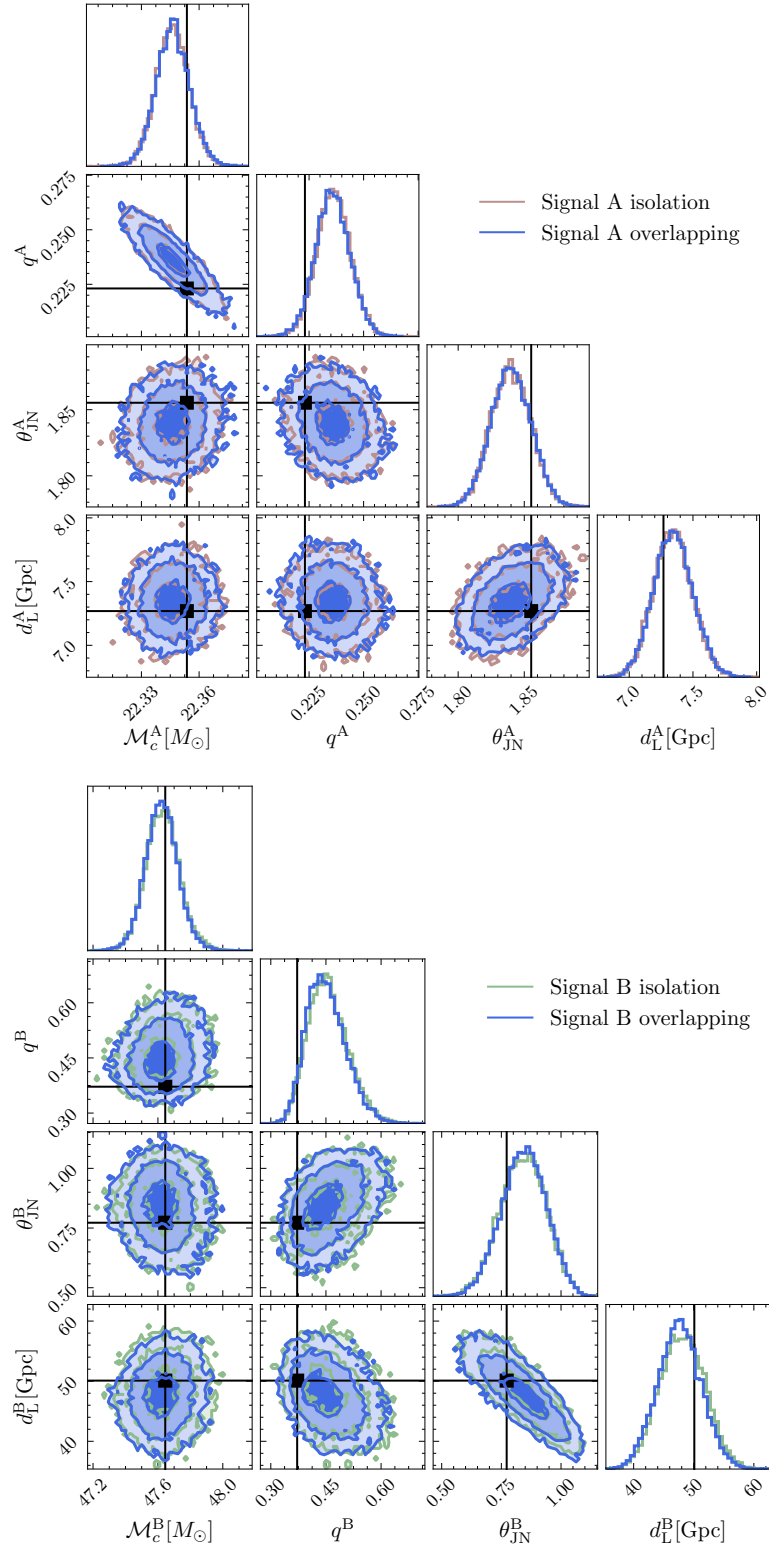


Figure 5.9: Comparison of parameter estimation results when two signals are in isolation and when two signals are overlapping.

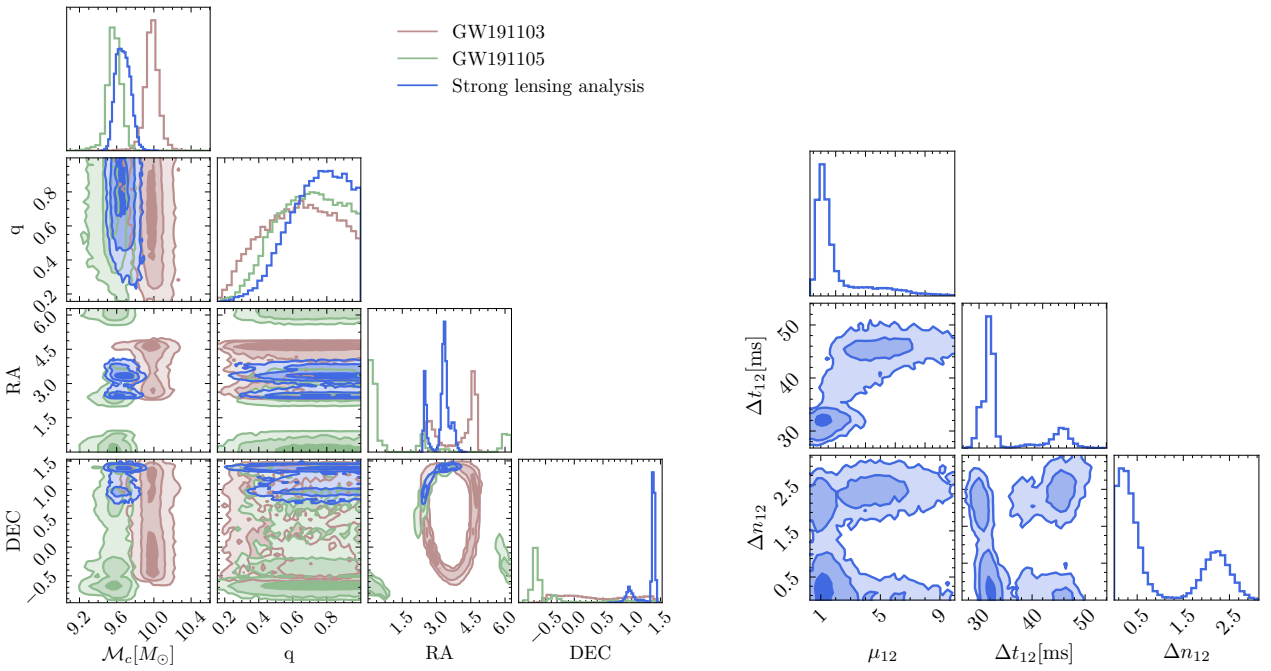


Figure 5.10: Analysing the pair, GW191103 (red) and GW191105 (green), under strong lensing hypothesis (blue) using the relative binning method. The left plot shows the measurements of the common parameter between the two events, when analysed individually and when analysed under strong lensing hypothesis. The right plot shows the measurements of the lensing parameters (only available when analysed under strong lensing hypothesis). The event pair was of great interest for strong lensing searches due to significant overlaps in the posterior distributions of individual events, though the analyses turned out to be inconclusive.

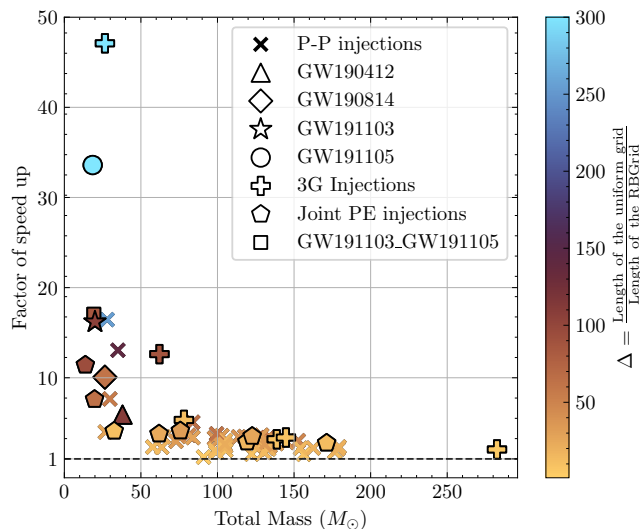


Figure 5.11: The speed-up achieved by the relative binning framework in relation to the total mass. The colourbar shows the reduction in the frequency points on which one needs to generate the waveform. The plot contains the comparison of run time for all events analysed using the relative binning framework in this chapter. The cross markers represent the P-P plot injections, the plus markers represent the 3G-injections, and the hexagon markers represent the lensing analyses. The remaining markers are for LIGO-Virgo events. The median value of the factor of speed-up is ~ 10 for total masses below $50M_{\odot}$. The low total mass signals typically have more cycles in-band, so they are more expensive to analyse with standard methods. Hence, the speed-up obtained by the relative binning method is precisely in the region where it is highly desirable.

The speed-up achieved by the relative binning method can be broadly attributed to two factors. First, every proposal waveform is generated on fewer frequency nodes – provided by the RBGrid – compared to the exact method, reducing the time required to generate the waveforms during sampling. Second, as the summary data are pre-computed, the summation in Eqs. (5.11)- (5.12) needs to be computed at fewer frequency points, reducing the number of operations. The first point is the more significant contributor to the overall speed-up. With this, the total speed-up for relative binning mainly depends on how coarse the RBGrid is compared to the corresponding uniform grid. The reduction in frequency nodes depends on the signal characteristics such as the duration, SNR, fiducial parameters, and also the total error chosen to generate the RBGrid.

Here, we use the comprehensive parameter estimation analyses performed in previous sections to assess the speed-up obtained by the relative binning compared to the exact method. Figure 5.11 shows the speed-up achieved by the relative binning method over the exact method in relation to the total mass of the systems. The colourbar shows the ratio of the length of the uniform frequency grid to the length of the corresponding RBGrid. We denote the ratio by Δ . For the instances where we performed parameter estimation runs with exact likelihood and relative binning approximation, we report the ratio of the run times of the two. For the instances where we only performed relative binning runs, we show the ratio of the average single likelihood evaluation time taken between the two methods calculated over a set of 10^4 points. The latter is an approximation, but it allows us to assess the speed-up factor given by relative binning without having to do the exact parameter estimation runs.

Still, for our various tests, the number of likelihood evaluations done for the relative binning and exact methods is in the same ballpark, so that this is a reasonable approximation to make.

We observe that the relative binning runs are up to a factor of ~ 34 faster for the LIGO-Virgo interferometers and up to a factor of ~ 47 faster for the 3G interferometers. The speed-up increases as the total mass of the system decreases. This is a highly desirable feature of the relative binning method since the low mass systems are typically more computationally expensive. The cost can be attributed to the large number of inspiral cycles in-band. Relative binning helps place a coarse frequency grid for such signals, which speeds up the analysis. Thus, the speed up achieved by relative binning is precisely in the region of the parameter space where it is needed, i.e., the low total mass region.

Additionally, the 3G detectors have a lower starting frequency, meaning they can observe a longer inspiral of the GW compared to the LIGO-Virgo interferometers. Consequently, we find that the relative binning framework provides a larger speed-up in the 3G scenario compared to similar systems as seen in LIGO-Virgo. This trend is also visible in Figure 5.11.

Joint parameter estimation reports a similar speed-up as individual parameter estimation. Here, we note that the lensing joint parameter estimation framework used in this work generates the first waveform and the subsequent images are obtained by scaling the first one. The scaling helps bypass the additional waveform generation steps, which saves computational cost. However, this is not the case in all strong lensing search methods, i.e., when the method is designed to generate all waveforms independently. In comparison to such methods, we expect a larger speed-up factor for relative binning framework.

5.5 Conclusion and outlook

In this chapter, we have presented a relative binning framework to perform fast parameter estimation. We have shown the robustness of the method by performing parameter estimation on a large set of simulated as well as real events. We have also extended the method to perform parameter estimation on overlapping signals and to perform strong lensing searches. This marks the first instance where the relative binning method has been tested in such a comprehensive manner. Our implementation of the relative binning framework can be found in the Github repository at [85].

To streamline the relative binning framework, we still need to address a couple of challenges. The performance of our method depends on the choice of the fiducial waveform. In this work, we have assumed that the fiducial waveform is either the same as the injected waveform for simulations or the maximum likelihood waveform for real events. However, the method can be seeded more realistically by using the best-fitting template reported by the template-based searches or maximum likelihood estimator routines can be used to determine the fiducial waveforms' parameters. We plan to work on the choice of the fiducial waveform and understanding how it can impact the performance of our method in the future. We also leave it to future work to implement the detector calibration parameters in the relative binning framework.

While the relative binning method is shown to work well in the joint parameter estimation of the overlapping signals, it is crucial to devise a recipe to determine when such a joint parameter estimation is required, i.e., if the signals are sufficiently apart, they can be analysed separately, which

may help reduce the cost of the analysis. This question was addressed in the comprehensive analysis performed by Baka *et al* [86]. The codebase presented in this chapter served as a building block for it.

The detection rates of gravitational wave signals and consequently the amount of computational resources needed to perform parameter estimation will increase with the upgrades to the current detectors. There is also a growing concern about the challenges posed by the increasing cost of parameter inference and data analysis tools in general in the 3G era. The relative binning framework presented in this chapter marks a step towards addressing these challenges.

Chapter 6



Constraints on modified propagation theories of GWs using strong lensing

General relativity predicts

- Gravitational waves are non-dispersive, i.e., all frequency components travel at the same speed.
- They travel at the speed of light.
- Their amplitude is inversely proportional to the distance to the source.

The non-dispersive nature has been a part of a suite of testing GR analyses carried out by the LVK collaboration [67]. The multimessenger detection of GW170817 helped place stringent constraints on the difference between the speed of GWs and the speed of light. Specifically, it was measured that the difference between the speed of GWs and light is between -3×10^{-15} and 6×10^{-16} times the speed of light [87]. Modifications to the distance-amplitude relation were investigated with the help of GW170817 and its electromagnetic counterpart [88]. According to GR, the relation is

$$\text{Amplitude} \propto \frac{1}{\text{Distance to the source}}. \quad (6.1)$$

However, these constraints remain relatively poor, as will become clear later. When discussing modified propagation theories, we specifically refer to the ones that predict a different distance-amplitude relation than GR. In this chapter, we demonstrate how the detection of a strongly lensed GW signal can significantly improve upon the bounds on the beyond-GR theories which allow for a modified GW propagation. This chapter contains results from our recent work on this topic [89].

6.1 Gravitational lensing and distance measurements

First, I briefly recapitulate the discussion on the gravitational lensing of gravitational waves from chapter 5. When GWs encounter a massive object in their path of propagation, they may deviate

from their original path. This phenomenon is known as gravitational lensing of gravitational waves. The precise effect of the lensing on the GWs depends on the relative configurations of the lens mass, the GW source, and their length scales.

Specifically, when the length scale of the lens is much larger than the wavelength of the GW signals, we are in the so-called geometric optics regime. Such a scenario could produce multiple copies of the GW signal (known as images), and each copy may be observable by the detectors as repeated GW signals from the same source. This phenomenon is referred to as the strong lensing of a gravitational wave signal. As the detectors can observe the same source multiple times, we can combine the information from multiple images to improve our measurements of the source parameters, especially, we can significantly improve our measurements of sky-localisation.

Electromagnetic distance

When a GW source is lensed, we can expect that the electromagnetic (EM) radiation coming from its host galaxy is also lensed, as is widely assumed in cosmography studies [56–58, 90, 91]. A joint GW+EM analysis can help locate the source’s host galaxy once its location is narrowed down to a few square degrees using only GW data. In this step, one reconstructs all the lenses in the region provided by the GW data to find which lens could best produce an image with properties similar to the ones observed; the galaxy that is undergoing lensing by this particular lens is then likely to be the host galaxy of the GW event. This methodology was first proposed in [65, 66]. For the scenarios where strong lensing produces four images (a quadruplet), we can narrow down the host of the GW source to one or a few galaxies. Various lensing rate estimates find that we may observe ≈ 1 strongly lensed event per year with a network of the LIGOs, Virgo, and KAGRA detector operating with 100% duty cycle [92–94]. The rates can be subject to uncertainties introduced by the merger-rates, detection thresholds, and detector duty cycles. The rate estimates also find that $\sim 30\%$ of all strong lensing scenarios will produce a quadruplet, making this a fairly likely scenario.

Once the host galaxy is known, a dedicated spectroscopic or photometric follow-up can yield a precise estimate of the redshift of the source. By combining the source’s redshift with a cosmological model, we can estimate the source’s luminosity distance [95]. Let us refer to this distance as the electromagnetic distance D_L^{EM} to the source.

Gravitational wave distance

Besides the electromagnetic distance (D_L^{EM}), we can have another independent measurement of the source’s luminosity distance from the GW data as explained in chapter 2. Let us refer to this distance as the gravitational wave distance D_L^{GW} to the source. The D_L^{GW} distance measurement may carry an imprint of the anomalous propagation of gravitational GWs while D_L^{EM} may not. Therefore, by comparing the two distances, D_L^{GW} and D_L^{EM} , the anomaly in the gravitational wave propagation can be discovered or bounded.

6.2 Modified propagation theories

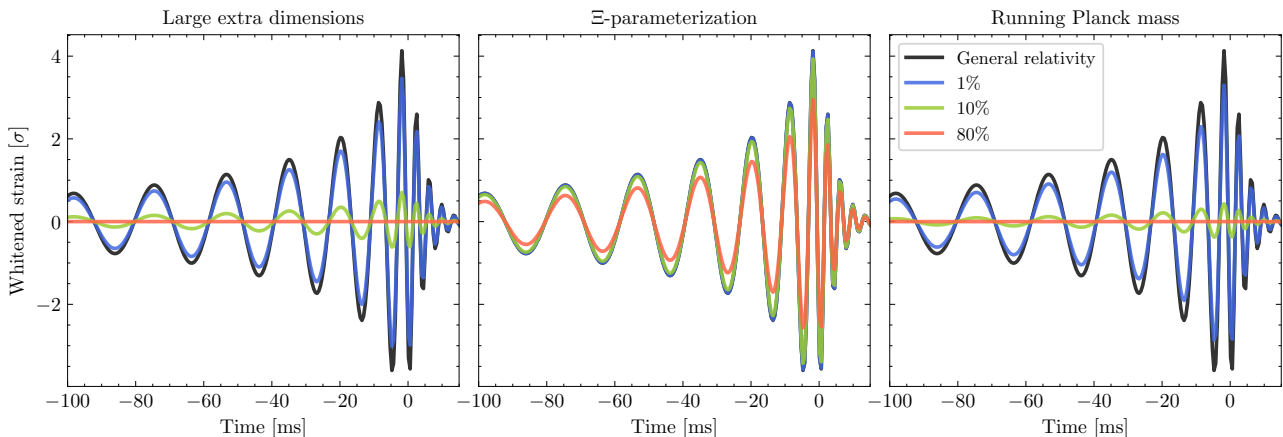


Figure 6.1: The effect on the time domain GW signal in each of the modified propagation models. For each model, the GR waveform is shown in black colour and deviation from it, by different amounts, is shown in different colours. In these examples, the GW source is assumed to be at ~ 5 Gpc and the masses of the source are similar to GW150914 [96]. For the running the Planck mass model, the deviation is absolute since one has $c_M = 0$ in GR. For large extra dimensions and Ξ -parametrisation, we consider the percentage deviation in the parameters D and Ξ_0 , taking the fiducial values to be $D = 4$ and $\Xi = 1$, respectively. For the Ξ -parametrisation, we arbitrarily choose $n = 1$ and keep it fixed in making the plot above.

When discussing modified propagation theories, we refer to those theories that predict a different GW distance-amplitude relation from GR. In the specific modified gravity models we consider – large extra dimensions, Ξ -parametrisation, and varying Planck mass – there is a non-trivial relationship between D_L^{GW} and D_L^{EM} . The relationships depend on the parameter(s) related to the deviation from GR and on the cosmological parameters. Let us briefly discuss what these relationships look like for our three models.

Large extra dimensions

In theories of gravity with large extra dimensions, there is the possibility of some energy of the GWs leaking into them [88, 97, 98], while EM radiation is confined to the usual three spatial dimensions. This would make the detected signal appear weaker, leading to larger measured values for D_L^{GW} than would otherwise be the case. For definiteness, we will work with the following simple phenomenological ansatz for the relation between D_L^{GW} and D_L^{EM} , based on conservation of integrated flux [3]:

$$\frac{D_L^{\text{GW}}}{\text{Mpc}} = \left(\frac{D_L^{\text{EM}}(z_s, H_0)}{\text{Mpc}} \right)^{\frac{D-2}{2}}, \quad (6.2)$$

where D is the number of spacetime dimensions and z_s is the source redshift¹. We will allow D to be a real number, with the GR value $D = 4$ as a fiducial value. An illustration of the effect of extra dimensions on a GW signal is given in the left plot of Figure 6.1.

¹Cardoso *et al.* [99] arrive at a similar scaling between D_L^{GW} and D_L^{EM} as Eq. (6.2) for a D -dimensional space time, apart from a frequency dependent factor. The frequency dependent factor determines the length scale of the effect based on the frequency of the GW signal whereas Eq. (6.2) presents a simplified ansatz, i.e., without a frequency dependence, following [3].

Theory	Parameter	Priors
Large extra dimension	D	Uniform(3, 5)
Ξ -parametrisation	Ξ_0	Log Uniform(0.01, 100)
	n	Uniform(0, 10)
Running Planck mass	c_M	Uniform(-150, 150)

Table 6.1: Deviation parameter(s) for each theory and the corresponding prior probability distributions used in our analyses. The ranges of the prior are centered around the general relativistic value of the parameter and are chosen following the previous studies on modified propagation [1–3].

The Ξ -parametrisation

Another parametrisation was proposed in [100], where the link between D_L^{GW} and D_L^{EM} is expressed as

$$D_L^{\text{GW}} = D_L^{\text{EM}}(z_s, H_0) \left[\Xi_0 + \frac{1 - \Xi_0}{(1 + z_s)^n} \right]. \quad (6.3)$$

The free parameters of the model are (Ξ_0, n) . This parameterisation is phenomenological, but as shown in [101], it can be related to a large class of modified gravity theories, including Horndeski [102] theories, Degenerate Higher Order Scalar-Tensor theories (DHOST) [103], and theories with nonlocally modified gravity [104–106]. When $z \ll 1$, $D_L^{\text{GW}} \simeq D_L^{\text{EM}}$. Therefore, similar to the extra dimension theories, we expect to observe a departure from GR only at large distances ($z \gtrsim 1$). For GR, $\Xi_0 = 1$ and n is degenerate. In Figure 6.1, middle plot, one can see an illustration of the effect of this modification on a GW signal.

Time-varying Planck mass

A time-varying Planck mass is another possible cause for modified GW propagation. Following [2], the relation between D_L^{GW} and D_L^{EM} can be expressed as

$$D_L^{\text{GW}}(z) = D_L^{\text{EM}}(z_s, H_0) \times \exp \left(\frac{c_M}{2\Omega_\Lambda} \ln \frac{1 + z_s}{(\Omega_m(1 + z_s)^3 + \Omega_\Lambda)^{1/3}} \right), \quad (6.4)$$

where c_M is a constant that relates the rate of change of the Planck mass to the fractional dark energy density in the Universe. For GR, $c_M = 0$. The right plot of Figure 6.1 illustrates the effect on a GW signal.

6.3 Strongly lensed signals: A probe complementary to the binary neutron star signals

Studying modified propagation theories in the context of strongly lensed and localised BBH signals is attractive because such events can help probe higher redshift regimes compared to BNS signals. In the past, modified propagation theories have been tested using GW signals from a binary neutron star merger (GW170817) with an identifiable EM counterpart [1–3, 88]. However, by cosmological standards, the GW170817 signal travelled only a small distance before it reached the detectors, carrying

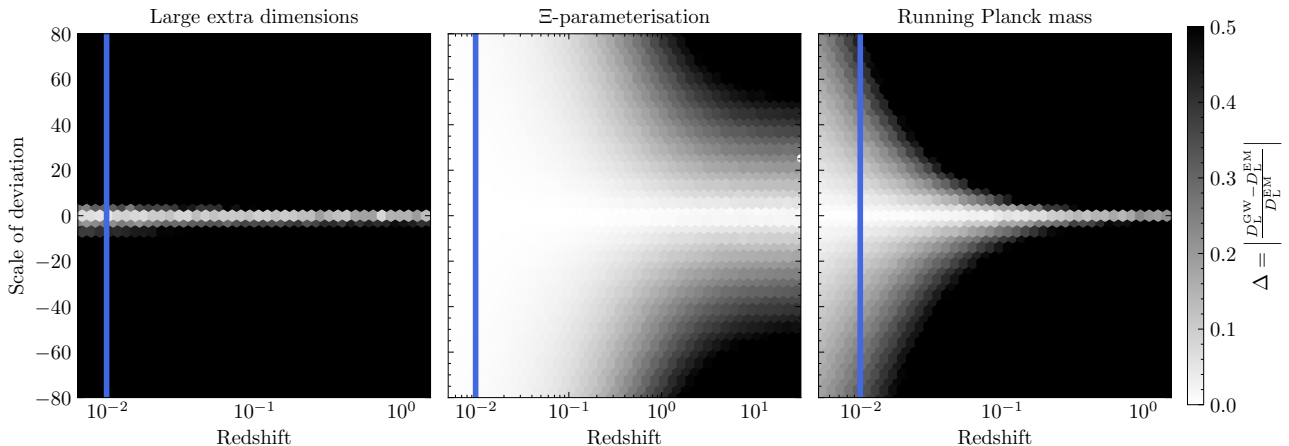


Figure 6.2: Imprint on the observable quantity (Δ) as a function of source redshift (x-axis) and scale of deviation (y-axis). For the large extra dimension model and Ξ -parametrisation, the y-axis shows percentage deviation with respect to the general relativistic value. The 0 on the y-axis corresponds to the GR value. For time-varying Planck mass, the y-axis shows the absolute deviation since the general relativistic value is 0 for the model parameter. The blue vertical line marks the redshift measurement of the GW170817 signal. For the Ξ -parametrisation and varying Planck mass, at the redshift of GW170817, the Δ is quite small even for large amounts of deviations from GR (grey region), suggesting that these models may be poorly constrained. Access to the high-redshift regime is likely to lead to better constraints on these deviations. On the other hand, the effect of extra dimensions is less sensitive to redshift, and measurements of D are already quite stringent at the redshift of GW170817 and are not expected to improve as much as for the other two cases when going to a higher redshift.

only a negligible imprint from any deviation from GR that may be present. Therefore, the constraints obtained from the neutron star merger remain poor. In the context of modified propagation theories, the imprint of the deviation tends to accumulate with the distance travelled by the signals. Due to magnification, GWs from *lensed* BBH events can potentially be seen out to redshifts $z \sim 6$ [93]; this feature leads to further increases in the imprints of any anomaly in the propagation, consequently improving our bounds on the anomaly. Therefore, the ability of a strongly lensed GW signal to probe the high-redshift regime makes it an invaluable probe to test modified propagation theories. We also note that modified propagation theories which predict a dephasing of GW signals compared to GR are routinely performed using BBH signal, however these are not the type of theories we are considering. We restrict our selves to the that predict a modified distance-amplitude relationship.

6.4 Measurements of model parameters

We want to estimate the posterior probability distribution on deviation parameters given the GW data and EM data, i.e.,

$$p(\vec{\theta}_{\text{MGR}}, H_0 | \vec{d}_{\text{GW}}, \vec{d}_{\text{EM}}), \quad (6.5)$$

where we use $\vec{\theta}_{\text{MGR}}$ to denote the model parameters in all generality (see Table 6.1), the notations \vec{d}_{GW} and \vec{d}_{EM} represent the GW and EM data of a quadruply lensed event whose host galaxy has been identified. The parameter H_0 denotes the Hubble constant.

Using Bayes' theorem, we can write

$$p(\vec{\theta}_{\text{MGR}}, H_0 | \vec{d}_{\text{GW}}, \vec{d}_{\text{EM}}) = \frac{\pi(\vec{\theta}_{\text{MGR}}, H_0) p(\vec{d}_{\text{GW}}, \vec{d}_{\text{EM}} | \vec{\theta}_{\text{MGR}}, H_0)}{Z}, \quad (6.6)$$

where $\pi(\vec{\theta}_{\text{MGR}}, H_0)$ is the prior probability distribution on $\vec{\theta}_{\text{MGR}}$ and H_0 ; the factor $p(\vec{d}_{\text{GW}}, \vec{d}_{\text{EM}} | \vec{\theta}_{\text{MGR}}, H_0)$ represents the likelihood function; and Z the evidence, whose value follows from the requirement that the posterior probability distribution is normalised. The prior distributions for $\vec{\theta}_{\text{MGR}}$ are specified in Table 6.1. We have chosen uninformative priors on each of the $\vec{\theta}_{\text{MGR}}$ parameters to not favour any specific value.

Prior choice H_0

For H_0 , we could in principle choose a relatively narrow prior range based on the Planck [107], SHoES [108], or other existing measurements [109]. Instead, we make a more conservative choice, i.e., a wider prior. Specifically, we use a measurement of H_0 that is obtained from the differences in time of arrival of the lensed images together with lens reconstruction through electromagnetic means. We use the measurement obtained in such a way as the prior on H_0 . This prior is relatively wider than any of the previous measurements; therefore, we argue that our measurements on $\vec{\theta}_{\text{MGR}}$ are on the conservative side.

The Hubble constant measurement can be determined by observing the delays in the arrival time of the lensed images [110]. The theory of strong lensing provides the relationship between the time delay (Δt) between two images and the difference in the Fermat potential ($\Delta\Phi$),

$$\Delta t = D_{\Delta t}(1 + z_l)\Delta\Phi, \quad (6.7)$$

where $D_{\Delta t}$ is called the time delay distance and z_l is the redshift of the lens. We can simultaneously obtain the $D_{\Delta t}$ and $\Delta\Phi$ by solving the equation above for a quadruple lensed system [66]. The remaining quantity, time delay distance $D_{\Delta t}$, is related to the Hubble constant in the following way:

$$D_{\Delta t}(z_l, z_s, H_0) = \frac{\int_0^{z_s} dz'/E(z')}{\int_{z_l}^{z_s} dz'/E(z')} D_{\text{L}}^{\text{EM}}(z_s, H_0), \quad (6.8)$$

where z_l and z_s are respectively the lens and the source redshift, and $E(z) \equiv \sqrt{\Omega_m(1+z)^3 + \Omega_\Lambda}$. Here, Ω_m is the matter density parameter and Ω_Λ is the dark energy density parameter. If $D_{\Delta t}$ is measured, we can estimate D_{L}^{EM} since we assume that z_l and z_s are known from the EM follow-up observations. In this work, for definiteness, we assume a flat Friedmann-Lemaître-Robertson-Walker universe, in which case one has

$$D_{\text{L}}^{\text{EM}} = \frac{(1 + z_s)}{H_0} \int_0^{z_s} \frac{dz'}{E(z')}. \quad (6.9)$$

Using the D_{L}^{EM} measurement, H_0 can be estimated through Eq. (6.9). $D_{\Delta t}$ can be measured after reconstructing the Fermat potential; However, owing to the computational complexity and cost, we skip the reconstruction step. We assume that the observed value of $D_{\Delta t}$ follows a Gaussian distribution with a 10% standard deviation [66]. To allow for an offset in the observation, we pick the mean of this distribution from another Gaussian distribution with a 10% standard deviation, which is centred at

the true value. We translate the measurement of $D_{\Delta t}$ into the measurement of D_L^{EM} using Eq. (6.8). Using the value of D_L^{EM} together with Eq. (6.9), we construct the prior for H_0 . Throughout the analysis, we keep the other cosmological parameters, Ω_m and Ω_Λ , fixed assuming that they are known to a few per cent accuracy [2].

Computing the joint likelihood

To calculate the likelihood $p(\vec{d}_{\text{GW}}, \vec{d}_{\text{EM}} | \vec{\theta}_{\text{MGR}}, H_0)$, we first express it as

$$p(\vec{d}_{\text{GW}}, \vec{d}_{\text{EM}} | \vec{\theta}_{\text{MGR}}, H_0) = \int d\vec{\theta} dz_s p(\vec{d}_{\text{GW}} | \vec{\theta}) p(\vec{d}_{\text{EM}} | z_s) \pi(\vec{\theta} | z_s, \vec{\theta}_{\text{MGR}}, H_0) \pi(z_s | \vec{\theta}_{\text{MGR}}, H_0), \quad (6.10)$$

where $\vec{\theta}$ denotes the GW source parameters, the factors $p(\vec{d}_{\text{GW}} | \vec{\theta})$ and $p(\vec{d}_{\text{EM}} | z_s)$ are the likelihoods of the GW and EM data, respectively, and z_s is the source redshift. The factors $\pi(\vec{\theta} | z_s, \vec{\theta}_{\text{MGR}}, H_0)$ and $\pi(z_s | \vec{\theta}_{\text{MGR}}, H_0)$ are the priors on the GW source parameters and the redshift.

Since we assume that the host galaxy has been localised, the true source redshift z_s is known. Recent studies have shown that the spectroscopic redshift of the source can be measured to a sub-per cent accuracy [111]. Therefore, we neglect the error on the measurement of z_s so the factor $p(\vec{d}_{\text{EM}} | z_s)$ becomes a Dirac delta function centered on z_s , reducing Eq. (6.10) to

$$p(\vec{d}_{\text{GW}}, \vec{d}_{\text{EM}} | \vec{\theta}_{\text{MGR}}, H_0) = \int d\vec{\theta} p(\vec{d}_{\text{GW}} | \vec{\theta}) p(\vec{\theta} | z_s, \vec{\theta}_{\text{MGR}}, H_0) p(z_s | \vec{\theta}_{\text{MGR}}, H_0). \quad (6.11)$$

To estimate the GW likelihood $p(\vec{d}_{\text{GW}} | \vec{\theta})$, we have to perform joint parameter estimation on strongly lensed signals as described in chapter 5. In principle, we could use the relative binning framework to do the analysis. However, it was developed after this analysis concluded. For the purpose of this work, we use the method which was specifically developed to rapidly analyse lensed images, called GOLUM [84]. GOLUM method uses a subset of posterior samples of the first image as prior for the subsequent image analyses. One can also integrate the relative binning framework into GOLUM to gain additional speed-up.

Once the GW likelihood is estimated, we perform the integration over all parameters represented by $\vec{\theta}$ except the luminosity distance D_L^{GW} to obtain

$$p(\vec{d}_{\text{GW}}, \vec{d}_{\text{EM}} | \vec{\theta}_{\text{MGR}}, H_0) = \int dD_L^{\text{GW}} p(\vec{d}_{\text{GW}} | D_L^{\text{GW}}) p(D_L^{\text{GW}} | z_s, \vec{\theta}_{\text{MGR}}, H_0) p(z_s | \vec{\theta}_{\text{MGR}}, H_0). \quad (6.12)$$

The prior $p(D_L^{\text{GW}} | z_s, \vec{\theta}_{\text{MGR}}, H_0)$ reduces to a Dirac delta function as we exactly know D_L^{GW} given the values of z_s , $\vec{\theta}_{\text{MGR}}$, H_0 and the modified gravity model (Eqs. (6.2), (6.3) and (6.4)). Therefore, integrating with respect to D_L^{GW} leads to

$$p(\vec{d}_{\text{GW}}, \vec{d}_{\text{EM}} | \vec{\theta}_{\text{MGR}}, H_0) = p(\vec{d}_{\text{GW}} | D_L^{\text{GW}}) p(z_s | \vec{\theta}_{\text{MGR}}, H_0). \quad (6.13)$$

Substituting Eq. (6.13) into Eq. (6.6), we can obtain the posterior distributions for $\vec{\theta}_{\text{MGR}}$ and H_0 . This completes the estimation of the joint likelihood.

While simulating the lensed BBH signals, we sample the component masses from the POWER-LAW+PEAK distribution presented in [112]. We use the IMRPhenomXPHM waveform model [30], with black hole spin magnitudes distributed uniformly between 0 and 1, and spin directions uniformly

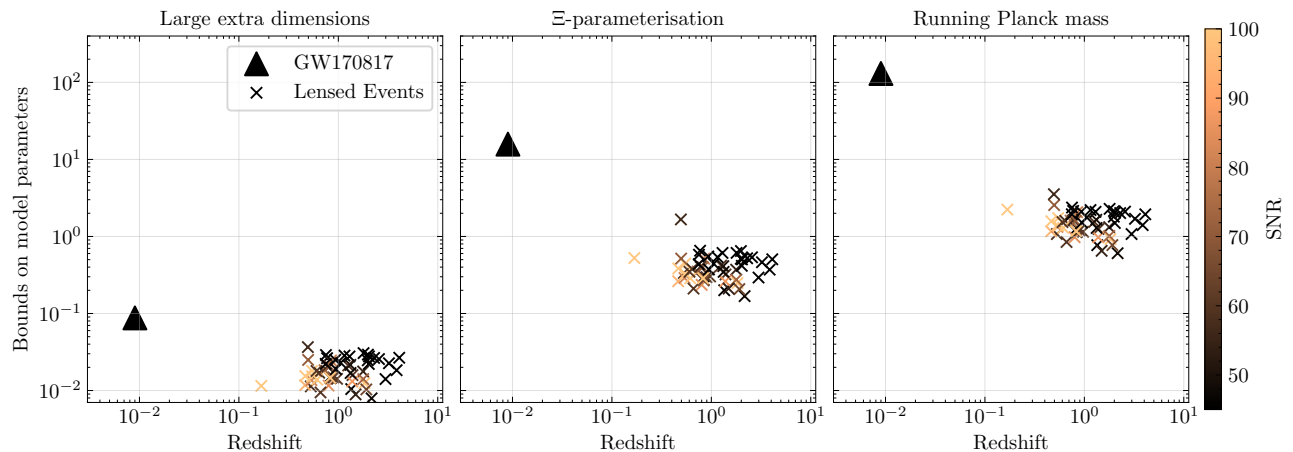


Figure 6.3: Bounds on the model parameters for the three models we considered. Each cross represents the bounds of the deviation parameter (y-axis) obtained by a quadruply lensed signal. The x-axis shows the corresponding redshift of the source, and the colourbar shows the quadrature sum of the SNR of the four images. The triangle shows the corresponding measurements obtained using the GW170817 signal and its electromagnetic counterpart. The y-axis shows relative error bars for the large extra dimensions ($\Delta D/D$) and Ξ -parametrisation ($\Delta \Xi/\Xi$). For time-varying Planck mass, we show the absolute error bars since the fiducial value is equal to zero. The error bars represent a 90% confidence interval. A strong lensing observation could improve the bounds on the large extra-dimensional model by a factor of ~ 5 , for Ξ -parametrisation by a factor of ~ 10 , and for time-varying Planck by a factor of $\sim 10^2$; consistent with inference drawn from Figure 6.2.

on the sphere. The distribution of the redshifts of the galaxy lenses, modelled as singular power law isothermal ellipsoids with external shear, follows the SDSS galaxy catalogue [113]. The fiducial values of $\vec{\theta}_{\text{MGR}}$ are equal to their GR values. The fiducial value of the Hubble constant is $H_0 = 67.4 \text{ km s}^{-1} \text{ Mpc}^{-1}$, and $\Omega_m = 0.315$. For the purpose of the simulation, we consider a network that consists of two LIGOs, Virgo, KAGRA, and the LIGO-India detectors, where the detection threshold on the network SNR is 8. Measurements of the deviation parameters made using the lensed GW signals will be compared to those made using the BNS merger GW170817, together with its host galaxy identification. For GW170817, we use the D_L^{GW} posterior sample from the corresponding data release [114]. For this event, we cannot construct the prior on H_0 for GW170817 using the method which we used for lensed events; therefore, we use Planck 2018 results when analysing it [115].

6.5 Results and conclusions

Figure 6.3 shows the bounds on the model parameters using strongly lensed BBH signals. We analyse a total of 55 signals. Note that we do not expect to see this many quadruply lensed events until the third-generation detector era, nor do we combine information from multiple simulated lensed events. Our aim here is to explore the diversity of scenarios one might encounter for a single quadruply lensed GW.

Each cross in Figure 6.3 corresponds to a simulated strongly lensed GW signal with four images. The x-axis shows the redshift of the source. The true values of model parameters are set equal to their GR values. The y-axis shows relative error bars for the large extra dimensions ($\Delta D/D$) and

Ξ -parametrisation ($\Delta\Xi/\Xi$). For time-varying Planck mass, we show the absolute error bar since the fiducial value is equal to zero. The error bars represent a 90% confidence interval. For the Ξ -parametrisation model, the parameter n is unconstrained when Ξ_0 equals its fiducial value of 1; we do not show results for it here, though it was treated as a free parameter in our measurements. Finally, the colourbar shows the combined SNR from the four images, i.e., the quadrature sum of the SNRs of the individual images. Also included are the results from GW170817.

The results are in qualitative agreement with plots presented in Figure 6.2. In particular, for Ξ_0 and c_M , the advantage of being able to access higher redshifts is evident, with bounds improving over those of GW170817 by factors of up to $\mathcal{O}(10)$ and $\mathcal{O}(10^2)$, respectively. By contrast, the bounds on D improve by up to a factor of ~ 5 . The differences in improvement can be explained by the qualitative predictions of Figure 6.2 where a given amount of deviation has a small imprint on the observable quantity (Δ) for Ξ -parameterisation (center) and time-varying Planck mass (right) but a large one for the large extra dimension model (left).

We note that for the strongly lensed events in our catalogue, the combined SNR from the four images tends to be higher than that of GW170817, which can also improve the measurement accuracy on D_L^{GW} and subsequently $\vec{\theta}_{\text{MGR}}$. However, Figure 6.3 shows that, using lensed events with SNR similar to GW170817 (which was $\simeq 32.4$ [12]), we can measure the deviation parameters more accurately compared to the latter, as the lensed events travel a longer distance. An increment in the distance made accessible by strong lensing is indeed the dominating factor in the improvement of measurement accuracies.

We also note that we did not directly perform lens reconstruction, but instead assumed Gaussian probability distributions for image magnification measurements used in the reconstruction of D_L^{GW} and reconstructed electromagnetic luminosity distances, with widths informed by current astrophysical expectations [65, 66]. We aim to treat this aspect in more depth in a future study. Similarly, the relation between D_L^{GW} and D_L^{EM} involves cosmological parameters. In this work, we only let H_0 be a free parameter, but the effect of uncertainties in the other parameters is also worth investigating. On the other hand, in this study, we used as a prior on H_0 the posterior density distribution obtained from time delay measurements and lens reconstruction, which is typically considerably wider than the ranges for H_0 obtained from either Planck or SHoES. Because of the degeneracy between H_0 and the deviation parameters, bounds on the latter are to a large extent set by the prior range of H_0 [2], which pushes our constraints on alternative theories towards the conservative side. We find that when analysing the lensed events with a prior from Planck 2018, we obtain bounds that are a factor of ~ 2 tighter.

Let us also make a comparison with existing bounds on the model parameters. For the Ξ -parametrisation, the bounds we obtain are consistent with the results of Finke *et al.* [116]. In Mastroianni *et al.* [1], bounds were obtained for the same three models considered here, by combining information from GW170817, its EM counterpart, and the information from the BBH signal GW190521, assuming that a particular EM flare observed by the Zwicky Transient Factory was associated with the GW190521 merger [117]. Since GW190521 originated at a redshift of $\simeq 0.8$ [118], adding this event brings the bounds on deviation parameters closer to what we find for lensed events. For example, they report $\delta\Xi_0/\Xi_0 \lesssim 3 - 10$, comparable to the bounds of our simulations. However, it should be noted

that the association of GW190521 with the EM flare is by no means conclusive; see e.g. [119]. Studies based on the cosmic microwave background and large structure formation can lead to bounds on c_M that are similar to the ones for lensed events; see e.g. [120]. Finally, methods have been developed that exploit the observed population properties of binary black hole coalescences using gravitational wave data only, in terms of e.g., redshift and mass distributions [121–123].

In summary, the previous gravitational wave-based measurements on anomalous propagation models have relied on GW170817 with its EM counterpart. Until third-generation detectors such as the Einstein Telescope and Cosmic Explorer are operational, gravitational waves from binary neutron star mergers will only be seen to a relatively small redshift. Moreover, a definitive identification of transient electromagnetic counterparts to a GW signal may remain elusive. What we have demonstrated here is that a single fortuitous discovery of a lensed signal in conjunction with a dedicated electromagnetic follow-up may help us probe the high-redshift regime, enabling significantly stronger bounds on models of anomalous gravitational wave propagation.



Public summary

What are gravitational waves? Imagine sitting by the Oudegracht (old canal in Utrecht) on a quiet sunny day. If someone throws a stone in the canal, it will generate ripples in the water. Things like the stone's weight, shape, and how fast it was thrown may determine the properties of the ripples (amplitude and frequency mainly). Let's assume, for some reason (which will become clear later), we could not see the stone falling in the water. We could only see the ripples. In this situation, is it possible to tell something about the properties of the stone (weight, shape, speed) simply by looking at the ripples? Indeed, if we have a physical theory that predicts the properties of the ripples given the properties of the stone, we may be able to deduce a few things.

Similarly, the gravitational waves (GWs) are ripples in spacetime caused by movements of heavy objects. We cannot see these objects with the naked eye from Earth since they are too far and/or do not emit any light. However, we could still deduce a few things about these objects if we could detect the ripples they produce *and* if we have a theory that can predict the properties of the waves given on the properties of the object. In fact, we do have such a theory, and it is Einstein's theory of relativity. However, nearly a 100 years after Einstein published the theory of relativity, we still did not have instruments sensitive enough to detect the gravitational waves. Einstein also believed them to be too weak to have any consequence.

How do we detect them? When a gravitational wave passes by, it moves the objects in its surroundings. The instruments to detect gravitational waves measure relative movements between two test masses (mirrors). On 14th September 2015, two LIGO detectors made the first direct observation of a gravitational wave signal, GW150914, from the merger of two black holes (massive objects with gravity so strong that even light cannot escape). Specifically, they observed the last few cycles of two black holes orbiting around each other, coming closer with each cycle, and merging to create a bigger black hole. The merger released a tremendous amount of energy into the space, which reached the Earth in the form of ripples in spacetime – gravitational waves. The GW150914 signal moved the test masses by around 10^{-18} meters, and the detectors indeed measured such tiny movements. To give an example, the measurement accuracy here amounts to observing the second nearest star (nearest being the sun) from Earth move by the width of a human hair. Between 2015 and 2025, the network of two LIGOs, located in Hanford and Louisiana, and the Virgo detector located in Pisa, has detected

around 300 gravitational wave signals. Such detections have enabled us to probe exciting new physics.

What is a glitch? Why is it problematic? Recalling the water-ripple analogy, besides the sources we want to observe (stones), there may be many other unwanted disturbances (like a bike falling in the canal). Similarly, besides an astrophysical gravitational wave signal, there are several terrestrial sources which may make the test masses of the detector move, creating a false impression of a GW passing by. We refer to such terrestrial sources as the *noise* sources. Specifically, the short-lived (up to a few seconds or minutes) noise sources are known as *glitches*.

Glitches are problematic. Sometimes they can masquerade as GW signals. Sometimes they occur exactly at the same time as when a gravitational wave reaches the detector, which corrupts the signal. Glitches deteriorate the quality of the data, hindering the transition to precision science. Especially for the next generation of GW detectors, such as the Einstein Telescope, it is crucial to develop a methodology to remove glitches from the data. In chapter 4 of my thesis, we developed such a method exploiting the triangle design to remove glitches overlapping with the signal, taking an important first step towards doing precision science. Also, such analyses quantify the advantage of the triangular geometry of the Einstein Telescopes over the alternative geometries for the first time.

What can we learn from GW signals? Once we establish that the GW signal is “clean”, i.e. without any glitches, we can estimate several properties of the objects that produced them. Indeed, we could estimate the properties of the black hole merger, GW150914. Among other things, we estimated that the GW signal travelled 1.3 billion light-years to reach the Earth, and it was primarily located in the southern hemisphere. We estimated that the two black holes were around 36 and 29 times the mass of the sun, and their merger created a black hole 62 times heavier than the sun. The remaining mass is released in the form of energy carried away by GWs. We also estimated how fast the black holes were spinning and their orientations.

While measuring the source parameters is the key to several downstream analyses (an example below), it is a computationally expensive. The state-of-the-art methods require about a few days to a week per signal. To address the growing computational cost of LIGO and Virgo and to create a stepping stone for the transition to the Einstein Telescope era, faster parameter estimation techniques are required. To that end, we developed a methodology to make parameter estimation faster and extensively tested it for various configurations in Chapter 5.

Can the predictions of general relativity be tested with gravitational lensing of gravitational waves? The last chapter concerns testing the general relativity using strongly lensed gravitational waves – a phenomenon where the GWs suffer a deflection and may split into multiple *images*, due to a heavy object in their path. Strong lensing helps observe the same GW signal multiple times, i.e., if we have 3 detectors (two LIGOs and the Virgo) and if we detect 4 lensed images, we virtually have observed the signal 12 times, resulting in accurate sky-location and distance measurement. Through simulations, we show that this feature of strongly lensed GWs can be exploited to test the predictions of (beyond) general relativistic theories, highlighting the importance of the searches for strongly lensed gravitational waves.



Openbare samenvatting

Wat zijn zwaartekrachtgolven? Stel je voor dat je op een rustige, zonnige dag aan de Oudegracht zit. Als iemand een steen in de gracht gooit, ontstaan er rimpelingen in het water. Zaken als het gewicht en de vorm van de steen en de snelheid waarmee deze is gegooid, kunnen bepalend zijn voor de eigenschappen van de rimpelingen (voornamelijk de amplitude en frequentie). Laten we aannemen dat we om een of andere reden (die later duidelijk zal worden) de steen niet in het water konden zien vallen. We konden alleen de rimpelingen zien. Is het in deze situatie mogelijk om iets te zeggen over de eigenschappen van de steen (gewicht, vorm, snelheid) door alleen naar de rimpelingen te kijken? Als we een natuurkundige theorie hebben die de eigenschappen van de rimpelingen voorspelt op basis van de eigenschappen van de steen, kunnen we inderdaad een aantal dingen afleiden.

Op dezelfde manier zijn zwaartekrachtgolven (ZG's) rimpelingen in de ruimtetijd die worden veroorzaakt door bewegingen van zware objecten. We kunnen deze objecten niet met het blote oog vanaf de aarde zien, omdat ze te ver weg zijn en/of geen licht uitstralen. We zouden echter toch een aantal dingen over deze objecten kunnen afleiden als we de rimpelingen die ze produceren zouden kunnen detecteren *en* als we een theorie zouden hebben die de eigenschappen van de golven kan voorspellen op basis van de eigenschappen van het object. We hebben inderdaad zo'n theorie, namelijk Einsteins relativiteitstheorie. Maar bijna 100 jaar nadat Einstein de relativiteitstheorie publiceerde, hadden we nog steeds geen instrumenten die gevoelig genoeg waren om zwaartekrachtgolven te detecteren. Einstein geloofde ook dat ze te zwak waren om enige gevolgen te hebben.

Hoe detecteren we ze? Wanneer er een zwaartekrachtgolf voorbij komt, beweegt deze de objecten in zijn omgeving. De instrumenten om zwaartekrachtgolven te detecteren meten relatieve bewegingen tussen twee testmassa's (spiegels). Op 14 september 2015 hebben twee LIGO-detectoren voor het eerst rechtstreeks een zwaartekrachtgolfsignaal waargenomen, GW150914, afkomstig van de samensmelting van twee zwarte gaten (massieve objecten met een zo sterke zwaartekracht dat zelfs licht er niet aan kan ontsnappen). Ze observeerden met name de laatste paar cycli van twee zwarte gaten die om elkaar heen draaiden, bij elke cyclus dichterbij elkaar kwamen en samensmolten tot een groter zwart gat. Door de samensmelting kwam een enorme hoeveelheid energie vrij in de ruimte, die de aarde bereikte in de vorm van rimpelingen in de ruimtetijd: zwaartekrachtgolven. Het ZG150914-signaal verplaatste de testmassa's met ongeveer 10^{-18} meter, en de detectoren hebben inderdaad zulke kleine bewegingen

gemeten. Om een voorbeeld te geven: de meetnauwkeurigheid komt hier neer op het waarnemen van de op één na dichtstbijzijnde ster (de dichtstbijzijnde is de zon) vanaf de aarde, die zich verplaatst met de breedte van een menselijke haar. Tussen 2015 en 2025 heeft het netwerk van twee LIGO's, gelegen in Hanford en Louisiana, en de Virgo-detector in Pisa, ongeveer 300 zwaartekrachtsignalen gedetecteerd. Dankzij deze detecties hebben we spannende nieuwe fysica kunnen onderzoeken.

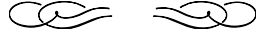
Wat is een storing? Waarom is dat problematisch? Als we terugdenken aan de analogie met de rimpelingen in het water, kunnen er naast de bronnen die we willen observeren (stenen) nog veel andere ongewenste verstoringen zijn (zoals een fiets die in het kanaal valt). Op dezelfde manier zijn er naast een astrofysisch zwaartekracht signaal verschillende aardse bronnen die de testmassa's van de detector kunnen doen bewegen, waardoor een valse indruk wordt gewekt dat er een ZG voorbijgaat. We noemen dergelijke aardse bronnen *ruisbronnen*. Meer specifiek worden kortstondige (tot enkele seconden of minuten) ruisbronnen *glitches* genoemd.

Glitches zijn problematisch. Soms kunnen ze zich voordoen als ZG-signalen. Soms treden ze precies op hetzelfde moment op als wanneer een zwaartekrachtgolf de detector bereikt, waardoor het signaal wordt verstoord. Glitches verslechteren de kwaliteit van de gegevens en belemmeren de overgang naar precisiewetenschap. Vooral voor de volgende generatie ZG-detectoren, zoals de Einstein Telescope, is het cruciaal om een methodologie te ontwikkelen om glitches uit de gegevens te verwijderen. In hoofdstuk 4 van mijn proefschrift hebben we een dergelijke methode ontwikkeld waarbij gebruik wordt gemaakt van het driehoekontwerp om glitches te verwijderen die het signaal overlappen, waarmee een belangrijke eerste stap is gezet in de richting van precisiewetenschap. Bovendien kwantificeren dergelijke analyses voor het eerst het voordeel van de driehoekige geometrie van de Einstein Telescopes ten opzichte van de alternatieve geometrieën.

Wat kunnen we leren van ZG-signalen? Zodra we hebben vastgesteld dat het ZG-signaal “zuiver” is, d.w.z. zonder storingen, kunnen we verschillende eigenschappen van de objecten die ze hebben geproduceerd, schatten. We konden inderdaad de eigenschappen van de fusie van zwarte gaten, GW150914, schatten. We hebben onder andere geschat dat het ZG-signaal 1,3 miljard lichtjaar heeft afgelegd om de aarde te bereiken en dat het zich voornamelijk op het zuidelijk halfrond bevond. We hebben geschat dat de twee zwarte gaten ongeveer 36 en 29 keer de massa van de zon hadden en dat hun fusie een zwart gat heeft gecreëerd dat 62 keer zwaarder is dan de zon. De resterende massa wordt vrijgegeven in de vorm van energie die door ZG's wordt meegevoerd. We hebben ook geschat hoe snel de zwarte gaten draaiden en wat hun oriëntatie was.

Hoewel het meten van de bronparameters de sleutel is tot verschillende downstream-analyses (zie voorbeeld hieronder), is het een rekenintensief proces. De modernste rekenpakketten hebben ongeveer een paar dagen tot een week nodig om één signaal te analyseren. Om de stijgende rekenkosten van LIGO en Virgo aan te pakken en een springplank te creëren voor de overgang naar het Einstein Telescope-tijdperk, zijn snellere technieken voor parameterraming nodig. Daartoe hebben we een methodologie ontwikkeld om parameterraming te versnellen en deze uitgebreid getest voor verschillende configuraties in hoofdstuk 5.

Kunnen we de voorspellingen van de algemene relativiteitstheorie testen met zwaartekrachtlenzen? Het laatste hoofdstuk van mijn proefschrift gaat over het testen van de algemene relativiteitstheorie met behulp van sterk gelenseerde zwaartekrachtgolven – een fenomeen waarbij de ZG's een afbuiging ondergaan en zich kunnen splitsen in meerdere *beelden*, als gevolg van een zwaar object in hun pad. Sterke lensing helpt om hetzelfde ZG-sigitaal meerdere keren waar te nemen. Als we bijvoorbeeld drie detectoren hebben (twee LIGO's en de Virgo) en we detecteren vier gelenseerde beelden, dan hebben we het signaal in feite twaalf keer waargenomen, wat resulteert in een nauwkeurige meting van de locatie aan de hemel en de afstand. Door middel van simulaties laten we zien dat deze eigenschap van sterk gelenseerde ZG's kan worden benut om de voorspellingen van (meer dan) algemene relativistische theorieën te testen, wat het belang van het zoeken naar sterk gelenseerde zwaartekrachtgolven onderstreept.



Curriculum vitae

Personal information

Name Harsh Narola
Nationality Indian
Date of birth 24 July 1998
Email h.b.narola@uu.nl

Education

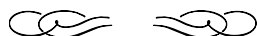
2021-2025 PhD in Physics
GRASP, Utrecht University; Prof. dr. C. Van Den Broeck

2015-2020 BS-MS Dual Degree
Indian Institute of Science Education and Research (IISER), Tirupati.
Master's thesis advisor: Prof. dr. Anand S. Sengupta;
Indian Institute of Technology (IIT), Gandhinagar.

Selected publications

- H. Narola, T. Wouters, *et al.*. “Null-stream-based third-generation-ready glitch mitigation for gravitational wave measurements”. In: *Phys. Rev. D* 112.2 (2025). DOI: 10.1103/l6tp-ykxp.
- H. Narola, J. Janquart, *et al.*. “Relative binning for complete gravitational-wave parameter estimation with higher-order modes and precession, and applications to lensing and third-generation detectors”. In: *Phys. Rev. D* 110.8 (2024). DOI: 10.1103/PhysRevD.110.084085.
- H. Narola, J. Janquart, *et al.*. “How well can modified gravitational wave propagation be constrained with strong lensing?”. In: *Phys. Rev. D* 109.8 (2024). DOI: 10.1103/PhysRevD.109.084064.

- T. Dooney, H. Narola, *et al.*. “Time-domain reconstruction of signals and glitches in gravitational wave data with deep learning”. Accepted in: *Phys. Rev. D* (2025). DOI: 10.1103/s91m-c2jw.
- T. Baka, H. Narola, *et al.*. “Overlapping signals in next-generation gravitational wave observatories: A recipe for selecting the best parameter estimation technique”. Accepted in: *Phys. Rev. D* (2025). arXiv:2507.10304v2.



Acknowledgments

While I cannot possibly thank everyone for everything that has made this journey possible, I will still make an attempt.

I want to start by thanking my promoter, Chris. I am thankful for the freedom you gave me during the first half of my PhD, which allowed me to work on a variety of topics. I want to thank you for teaching me how to take criticism and think objectively about my work, especially in the latter half. I must also thank you since it would have taken me a few more years to discover Westmalle Tripel if it weren't for you.

I want to thank my co-promoter, Anuradha. Some of our earlier discussions inspired me to think about glitches in the Einstein Telescope era. I am grateful for your support when working within the large collaborations. I also want to thank you for taking the time to hear me complain.

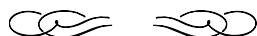
I want to thank the admins of the Stoomboot cluster at Nikhef. I want to thank Monique and Marie-Thérèse at GRASP and the admins at the international service desk at Utrecht University.

My master's thesis advisors, Soumen and Anand, deserve many thanks for getting me started on this topic. I appreciate the support from the collaborators in Leuven. Tjonnie, thank you for your insights on various occasions and for reminding me to slow down every time I feel like I am talking too slow. I am thankful to Otto and the colleagues in Hong Kong.

I want to thank my colleagues at GRASP: Sumit, Mick, Fabian, Haris, Martin, Luca, Olaf, Johanna, Gijs, Quirijn, Justus, Nick, Rick, Noor, Suzanne, Rene, Marcel, Marta, Alessandro, Thomas, and Raimond. I thank Tomek for cakes and cookies, Stefano for the promises to stay in touch, Anna for actually staying in touch, Justin for the travels to conferences, and Bas for the good vibes. Thibaud and Peter, I look forward to working with you and more importantly to our next visit to the dim sum restaurant. Tom, I have learnt a great deal from our collaboration and I am looking forward to more. Marc, it was a pleasure sharing the office with you until you abandoned me.

I want to thank my friends in Utrecht: Anam, Rajat, Melissa, Antoni, Anushree, and Shridhar. I want to thank Marijn for facing all the headwind on our biking trips. My former landlords and landladies around Utrecht have been a part of this adventure. Without their interventions, I might have completed my PhD a few months earlier.

I am indebted to my parents, big brother, and sister-in-law. I thank Suze's family for making me feel at home and Suze for her love.



Bibliography

- [1] S. Mastrogiovanni, L. Haegel, C. Karathanasis, I. Magaña Hernandez, and D. A. Steer. Gravitational wave friction in light of GW170817 and GW190521. *JCAP*, 02:043, 2021.
- [2] Macarena Lagos, Maya Fishbach, Philippe Landry, and Daniel E. Holz. Standard sirens with a running Planck mass. *Phys. Rev. D*, 99(8):083504, 2019.
- [3] Kris Pardo, Maya Fishbach, Daniel E. Holz, and David N. Spergel. Limits on the number of spacetime dimensions from GW170817. *JCAP*, 07:048, 2018.
- [4] Isaac Newton. *Philosophiæ Naturalis Principia Mathematica*. England, 1687.
- [5] Charles W. Misner, K. S. Thorne, and J. A. Wheeler. *Gravitation*. W. H. Freeman, San Francisco, 1973.
- [6] James Gleick. *Isaac Newton*. Pantheon Books, New York, 2003.
- [7] A. Einstein. Die grundlage der allgemeinen relativitätstheorie. *Annalen der Physik*, 354(7):769–822, 1916.
- [8] Michele Maggiore. *Gravitational Waves. Vol. 1: Theory and Experiments*. Oxford University Press, 2007.
- [9] J. Aasi et al. Advanced LIGO. *Class. Quant. Grav.*, 32:074001, 2015.
- [10] Bernard F. Schutz. Networks of gravitational wave detectors and three figures of merit. *Class. Quant. Grav.*, 28:125023, 2011.
- [11] F. Acernese et al. Advanced Virgo: a second-generation interferometric gravitational wave detector. *Class. Quant. Grav.*, 32(2):024001, 2015.
- [12] B. P. Abbott et al. GW170817: Observation of Gravitational Waves from a Binary Neutron Star Inspiral. *Phys. Rev. Lett.*, 119(16):161101, 2017.
- [13] Yoichi Aso, Yuta Michimura, Kentaro Somiya, Masaki Ando, Osamu Miyakawa, Takanori Sekiguchi, Daisuke Tatsumi, and Hiroaki Yamamoto. Interferometer design of the KAGRA gravitational wave detector. *Phys. Rev. D*, 88(4):043007, 2013.

- [14] M. Saleem et al. The science case for LIGO-India. *Class. Quant. Grav.*, 39(2):025004, 2022.
- [15] David Reitze et al. Cosmic Explorer: The U.S. Contribution to Gravitational-Wave Astronomy beyond LIGO. *Bull. Am. Astron. Soc.*, 51(7):035, 2019.
- [16] M. Punturo et al. The Einstein Telescope: A third-generation gravitational wave observatory. *Class. Quant. Grav.*, 27:194002, 2010.
- [17] Michele Maggiore et al. Science Case for the Einstein Telescope. *JCAP*, 03:050, 2020.
- [18] Tania Regimbau et al. A Mock Data Challenge for the Einstein Gravitational-Wave Telescope. *Phys. Rev. D*, 86:122001, 2012.
- [19] B. Sathyaprakash et al. Scientific Objectives of Einstein Telescope. *Class. Quant. Grav.*, 29:124013, 2012. [Erratum: *Class.Quant.Grav.* 30, 079501 (2013)].
- [20] Marica Branchesi et al. Science with the Einstein Telescope: a comparison of different designs. 3 2023.
- [21] J. Veitch et al. Parameter estimation for compact binaries with ground-based gravitational-wave observations using the LALInference software library. *Phys. Rev. D*, 91(4):042003, 2015.
- [22] I. M. Romero-Shaw et al. Bayesian inference for compact binary coalescences with bilby: validation and application to the first LIGO–Virgo gravitational-wave transient catalogue. *Mon. Not. Roy. Astron. Soc.*, 499(3):3295–3319, 2020.
- [23] Vitor Cardoso, Leonardo Gualtieri, Carlos Herdeiro, and Ulrich Sperhake. Exploring New Physics Frontiers Through Numerical Relativity. *Living Rev. Relativity*, 18:1, 2015.
- [24] P. Ajith et al. Inspiral-merger-ringdown waveforms for black-hole binaries with non-precessing spins. *Phys. Rev. Lett.*, 106:241101, 2011.
- [25] L. Santamaria et al. Matching post-Newtonian and numerical relativity waveforms: systematic errors and a new phenomenological model for non-precessing black hole binaries. *Phys. Rev. D*, 82:064016, 2010.
- [26] S. Khan et al. Frequency-domain gravitational waves from nonprecessing black-hole binaries. II. A phenomenological model for the advanced detector era. *Phys. Rev. D*, 93(4):044007, 2016.
- [27] S. Husa et al. Frequency-domain gravitational waves from nonprecessing black-hole binaries. I. New numerical waveforms and anatomy of the signal. *Phys. Rev. D*, 93(4):044006, 2016.
- [28] Alessandra Buonanno, Gregory B. Cook, and Frans Pretorius. Inspiral, merger and ring-down of equal-mass black-hole binaries. *Phys. Rev. D*, 75:124018, 2007.
- [29] Anna Puecher, Chinmay Kalaghatgi, Soumen Roy, Yoshinta Setyawati, Ish Gupta, B. S. Sathyaprakash, and Chris Van Den Broeck. Testing general relativity using higher-order modes of gravitational waves from binary black holes. *Phys. Rev. D*, 106(8):082003, 2022.

-
- [30] G. Pratten et al. Computationally efficient models for the dominant and subdominant harmonic modes of precessing binary black holes. *Phys. Rev. D*, 103(10):104056, 2021.
- [31] John Skilling. Nested sampling for general Bayesian computation. *Bayesian Analysis*, 1(4):833–859, 2006.
- [32] J. Veitch and A. Vecchio. Bayesian coherent analysis of in-spiral gravitational wave signals with a detector network. *Phys. Rev. D*, 81:062003, 2010.
- [33] J. S. Speagle. dynesty: a dynamic nested sampling package for estimating Bayesian posteriors and evidences. *Mon. Not. Roy. Astron. Soc.*, 493(3):3132–3158, 2020.
- [34] G. Ashton et al. BILBY: A user-friendly Bayesian inference library for gravitational-wave astronomy. *Astrophys. J. Suppl.*, 241(2):27, 2019.
- [35] B P Abbott et al. Effects of data quality vetoes on a search for compact binary coalescences in Advanced LIGO’s first observing run. *Class. Quant. Grav.*, 35(6):065010, 2018.
- [36] Derek Davis et al. LIGO detector characterization in the second and third observing runs. *Class. Quant. Grav.*, 38(13):135014, 2021.
- [37] F. Acernese et al. Virgo Detector Characterization and Data Quality during the O3 run. 5 2022.
- [38] S. Soni et al. LIGO Detector Characterization in the first half of the fourth Observing run. 9 2024.
- [39] S. A. Usman et al. The PyCBC search for gravitational waves from compact binary coalescence. *Class. Quant. Grav.*, 33(21):215004, 2016.
- [40] S. Sachdev et al. The GstLAL Search Analysis Methods for Compact Binary Mergers in Advanced LIGO’s Second and Advanced Virgo’s First Observing Runs. 1 2019.
- [41] L. K. Nuttall. Characterizing transient noise in the LIGO detectors. *Phil. Trans. Roy. Soc. Lond. A*, 376(2120):20170286, 2018.
- [42] D. Davis and M. Walker. Detector Characterization and Mitigation of Noise in Ground-Based Gravitational-Wave Interferometers. *Galaxies*, 10(1):12, 2022.
- [43] N J. Cornish and T. B. Littenberg. BayesWave: Bayesian Inference for Gravitational Wave Bursts and Instrument Glitches. *Class. Quant. Grav.*, 32(13):135012, 2015.
- [44] P. J. Green. Reversible jump Markov chain Monte Carlo computation and Bayesian model determination. *Biometrika*, 82(4):711–732, 1995.
- [45] N. J. Cornish et al. BayesWave analysis pipeline in the era of gravitational wave observations. *Phys. Rev. D*, 103(4):044006, 2021.
- [46] R. Abbott et al. GWTC-3: Compact Binary Coalescences Observed by LIGO and Virgo during the Second Part of the Third Observing Run. *Phys. Rev. X*, 13(4):041039, 2023.

- [47] R. Udall et al. The anti-aligned spin of GW191109: glitch mitigation and its implications. 9 2024.
- [48] Miriam Cabero et al. Blip glitches in Advanced LIGO data. *Class. Quant. Grav.*, 36(15):15, 2019.
- [49] S. Hild et al. Sensitivity Studies for Third-Generation Gravitational Wave Observatories. *Class. Quant. Grav.*, 28:094013, 2011.
- [50] M Lopez et al. Simulating transient noise bursts in LIGO with generative adversarial networks. *Phys. Rev. D*, 106(2):023027, 2022.
- [51] M. Lopez et al. Simulating Transient Noise Bursts in LIGO with gengli. 5 2022.
- [52] K. Chatziioannou et al. Modeling compact binary signals and instrumental glitches in gravitational wave data. *Phys. Rev. D*, 103(4):044013, 2021.
- [53] S. Hourihane et al. Accurate modeling and mitigation of overlapping signals and glitches in gravitational-wave data. *Phys. Rev. D*, 106(4):042006, 2022.
- [54] Bernard F. Schutz. Determining the Hubble Constant from Gravitational Wave Observations. *Nature*, 323:310–311, 1986.
- [55] Walter Del Pozzo. Inference of the cosmological parameters from gravitational waves: application to second generation interferometers. *Phys. Rev. D*, 86:043011, 2012.
- [56] Hsin-Yu Chen, Maya Fishbach, and Daniel E. Holz. A two per cent Hubble constant measurement from standard sirens within five years. *Nature*, 562(7728):545–547, 2018.
- [57] M. Fishbach et al. A Standard Siren Measurement of the Hubble Constant from GW170817 without the Electromagnetic Counterpart. *Astrophys. J. Lett.*, 871(1):L13, 2019.
- [58] Rachel Gray et al. Cosmological inference using gravitational wave standard sirens: A mock data analysis. *Phys. Rev. D*, 101(12):122001, 2020.
- [59] R. Abbott et al. Constraints on the cosmic expansion history from GWTC-3. 11 2021.
- [60] Antonella Palmese, Clecio R. Bom, Sunil Mucesh, and William G. Hartley. A Standard Siren Measurement of the Hubble Constant Using Gravitational-wave Events from the First Three LIGO/Virgo Observing Runs and the DESI Legacy Survey. *Astrophys. J.*, 943(1):56, 2023.
- [61] Kipp Cannon et al. Toward Early-Warning Detection of Gravitational Waves from Compact Binary Coalescence. *Astrophys. J.*, 748:136, 2012.
- [62] B. P. Abbott et al. Multi-messenger Observations of a Binary Neutron Star Merger. *Astrophys. J. Lett.*, 848(2):L12, 2017.
- [63] R. Abbott et al. Search for gravitational-lensing signatures in the full third observing run of the LIGO-Virgo network. 4 2023.

-
- [64] Jason S. C. Poon, Stefano Rinaldi, Justin Janquart, Harsh Narola, and Otto A. Hannuksela. Galaxy lens reconstruction based on strongly lensed gravitational waves: similarity transformation degeneracy and mass-sheet degeneracy. 6 2024.
- [65] Ewoud Wempe, Léon V. E. Koopmans, A. Renske A. C. Wierda, Otto Akseli Hannuksela, and Chris van den Broeck. A lensing multi-messenger channel: Combining LIGO-Virgo-Kagra lensed gravitational-wave measurements with Euclid observations. 4 2022.
- [66] Otto A. Hannuksela, Thomas E. Collett, Mesut Çalışkan, and Tjonnie G. F. Li. Localizing merging black holes with sub-arcsecond precision using gravitational-wave lensing. *Mon. Not. Roy. Astron. Soc.*, 498(3):3395–3402, 2020.
- [67] R. Abbott et al. Tests of General Relativity with GWTC-3. 12 2021.
- [68] Tom Dooney, Harsh Narola, Stefano Bromuri, R. Lyana Curier, Chris Van Den Broeck, Sarah Caudill, and Daniel Stanley Tan. DeepExtractor: Time-domain reconstruction of signals and glitches in gravitational wave data with deep learning. 1 2025.
- [69] R. Abbott et al. GW190412: Observation of a Binary-Black-Hole Coalescence with Asymmetric Masses. *Phys. Rev. D*, 102(4):043015, 2020.
- [70] R. Abbott et al. GW190814: Gravitational Waves from the Coalescence of a 23 Solar Mass Black Hole with a 2.6 Solar Mass Compact Object. *Astrophys. J. Lett.*, 896(2):L44, 2020.
- [71] N. Leslie, L. Dai, and G. Pratten. Mode-by-mode relative binning: Fast likelihood estimation for gravitational waveforms with spin-orbit precession and multiple harmonics. *Phys. Rev. D*, 104(12):123030, 2021.
- [72] Anuradha Samajdar, Justin Janquart, Chris Van Den Broeck, and Tim Dietrich. Biases in parameter estimation from overlapping gravitational-wave signals in the third-generation detector era. *Phys. Rev. D*, 104(4):044003, 2021.
- [73] Jose María Ezquiaga, Daniel E. Holz, Wayne Hu, Macarena Lagos, and Robert M. Wald. Phase effects from strong gravitational lensing of gravitational waves. *Phys. Rev. D*, 103(6):064047, 2021.
- [74] Rico K. L. Lo and Ignacio Magaña Hernandez. A Bayesian statistical framework for identifying strongly-lensed gravitational-wave signals. 4 2021.
- [75] J. Lin. Divergence measures based on the shannon entropy. *IEEE Transactions on Information Theory*, 37(1):145–151, 1991.
- [76] S. Kullback and R. A. Leibler. On Information and Sufficiency. *The Annals of Mathematical Statistics*, 22(1):79–86, 1951.
- [77] P. Virtanen et al.

- [78] B. P. Abbott et al. Prospects for observing and localizing gravitational-wave transients with Advanced LIGO, Advanced Virgo and KAGRA. *Living Rev. Rel.*, 21(1):3, 2018.
- [79] J. Janquart et al. Follow-up Analyses to the O3 LIGO-Virgo-KAGRA Lensing Searches. 6 2023.
- [80] The LIGO Scientific Collaboration, the Virgo Collaboration, and the KAGRA Collaboration. GWTC-3 Data Release, 2021.
- [81] The LIGO Scientific Collaboration, the Virgo Collaboration, and the KAGRA Collaboration. GWTC-2.1 Data Release, 2022.
- [82] Exploring the sensitivity of next generation gravitational wave detectors. <https://dcc.ligo.org/LIGO-P1600143/public>. Accessed: 2023-08-02.
- [83] J. Janquart et al. The Return of GOLUM: Improving Distributed Joint Parameter Estimation for Strongly-Lensed Gravitational Waves. 4 2023.
- [84] Justin Janquart, Otto A. Hannuksela, Haris K., and Chris Van Den Broeck. A fast and precise methodology to search for and analyse strongly lensed gravitational-wave events. *Mon. Not. Roy. Astron. Soc.*, 506(4):5430–5438, 2021.
- [85] Narola H. Janquart, J. and Baka T. Relativebilbying: a package for relative binning with bilby. <https://github.com/lemnis12/relativebilbying>, 2022.
- [86] Tomasz Baka, Harsh Narola, Justin Janquart, Anuradha Samajdar, Tim Dietrich, and Chris Van Den Broeck. Overlapping signals in next-generation gravitational wave observatories: A recipe for selecting the best parameter estimation technique. 7 2025.
- [87] B. P. Abbott et al. Gravitational Waves and Gamma-rays from a Binary Neutron Star Merger: GW170817 and GRB 170817A. *Astrophys. J. Lett.*, 848(2):L13, 2017.
- [88] B. P. Abbott et al. Tests of General Relativity with GW170817. *Phys. Rev. Lett.*, 123(1):011102, 2019.
- [89] Harsh Narola, Justin Janquart, Leïla Haegel, K. Haris, Otto A. Hannuksela, and Chris Van Den Broeck. How well can modified gravitational wave propagation be constrained with strong lensing? *Phys. Rev. D*, 109(8):084064, 2024.
- [90] B. P. Abbott et al. A Gravitational-wave Measurement of the Hubble Constant Following the Second Observing Run of Advanced LIGO and Virgo. *Astrophys. J.*, 909(2):218, 2021.
- [91] M. Soares-Santos et al. First Measurement of the Hubble Constant from a Dark Standard Siren using the Dark Energy Survey Galaxies and the LIGO/Virgo Binary–Black-hole Merger GW170814. *Astrophys. J. Lett.*, 876(1):L7, 2019.
- [92] Shun-Sheng Li, Shude Mao, Yuetong Zhao, and Youjun Lu. Gravitational lensing of gravitational waves: A statistical perspective. *Mon. Not. Roy. Astron. Soc.*, 476(2):2220–2229, 2018.

-
- [93] A. Renske A. C. Wierda, Ewoud Wempe, Otto A. Hannuksela, L. éon V. E. Koopmans, and Chris Van Den Broeck. Beyond the Detector Horizon: Forecasting Gravitational-Wave Strong Lensing. *Astrophys. J.*, 921(2):154, 2021.
- [94] Masamune Oguri. Effect of gravitational lensing on the distribution of gravitational waves from distant binary black hole mergers. *Mon. Not. Roy. Astron. Soc.*, 480(3):3842–3855, 2018.
- [95] David W. Hogg. Distance measures in cosmology. 5 1999.
- [96] B. P. Abbott et al. Observation of Gravitational Waves from a Binary Black Hole Merger. *Phys. Rev. Lett.*, 116(6):061102, 2016.
- [97] G. R. Dvali, Gregory Gabadadze, and Massimo Porrati. 4-D gravity on a brane in 5-D Minkowski space. *Phys. Lett. B*, 485:208–214, 2000.
- [98] Gianluca Calcagni, Sachiko Kuroyanagi, Sylvain Marsat, Mairi Sakellariadou, Nicola Tamanini, and Gianmassimo Tasinato. Gravitational-wave luminosity distance in quantum gravity. *Phys. Lett. B*, 798:135000, 2019.
- [99] Vitor Cardoso, Oscar J. C. Dias, and Jose P. S. Lemos. Gravitational radiation in D-dimensional space-times. *Phys. Rev. D*, 67:064026, 2003.
- [100] Enis Belgacem, Yves Dirian, Stefano Foffa, and Michele Maggiore. Modified gravitational-wave propagation and standard sirens. *Phys. Rev. D*, 98(2):023510, 2018.
- [101] Enis Belgacem et al. Testing modified gravity at cosmological distances with LISA standard sirens. *JCAP*, 07:024, 2019.
- [102] Gregory Walter Horndeski. Second-order scalar-tensor field equations in a four-dimensional space. *Int. J. Theor. Phys.*, 10:363–384, 1974.
- [103] David Langlois. Dark energy and modified gravity in degenerate higher-order scalar-tensor (DHOST) theories: A review. *Int. J. Mod. Phys. D*, 28(05):1942006, 2019.
- [104] Michele Maggiore. Phantom dark energy from nonlocal infrared modifications of general relativity. *Phys. Rev. D*, 89(4):043008, 2014.
- [105] Michele Maggiore and Michele Mancarella. Nonlocal gravity and dark energy. *Phys. Rev. D*, 90(2):023005, 2014.
- [106] Enis Belgacem, Yves Dirian, Stefano Foffa, and Michele Maggiore. Nonlocal gravity. Conceptual aspects and cosmological predictions. *JCAP*, 03:002, 2018.
- [107] The Scientific programme of Planck. 4 2006.
- [108] Adam G. Riess et al. *Astrophys. J. Lett.*, 934(1):L7, 2022.
- [109] Kenneth C. Wong et al. *Mon. Not. Roy. Astron. Soc.*, 498(1):1420–1439, 2020.

- [110] Kai Liao, Xi-Long Fan, Xu-Heng Ding, Marek Biesiada, and Zong-Hong Zhu. Precision cosmology from future lensed gravitational wave and electromagnetic signals. *Nature Commun.*, 8(1):1148, 2017. [Erratum: *Nature Commun.* 8, 2136 (2017)].
- [111] Xingchen Zhou, Yan Gong, Xian-Min Meng, Xin Zhang, Ye Cao, Xuelei Chen, Valeria Amaro, Zuhui Fan, and Liping Fu. Spectroscopic and Photometric Redshift Estimation by Neural Networks For the China Space Station Optical Survey (CSS-OS). *Astrophys. J.*, 909(1):53, 2021.
- [112] R. Abbott et al. Population of Merging Compact Binaries Inferred Using Gravitational Waves through GWTC-3. *Phys. Rev. X*, 13(1):011048, 2023.
- [113] Thomas E Collett. The population of galaxy-galaxy strong lenses in forthcoming optical imaging surveys. *Astrophys. J.*, 811(1):20, 2015.
- [114] The LIGO Scientific Collaboration and the Virgo Collaboration. Parameter estimation sample release for GWTC-1, 2020.
- [115] N. Aghanim et al. Planck 2018 results. VI. Cosmological parameters. *Astron. Astrophys.*, 641:A6, 2020. [Erratum: *Astron. Astrophys.* 652, C4 (2021)].
- [116] Andreas Finke, Stefano Foffa, Francesco Iacovelli, Michele Maggiore, and Michele Mancarella. Probing modified gravitational wave propagation with strongly lensed coalescing binaries. *Phys. Rev. D*, 104(8):084057, 2021.
- [117] M. J. Graham et al. Candidate electromagnetic counterpart to the binary black hole merger gravitational-wave event s190521g. *Phys. Rev. Lett.*, 124:251102, Jun 2020.
- [118] R. Abbott et al. GW190521: A Binary Black Hole Merger with a Total Mass of $150M_{\odot}$. *Phys. Rev. Lett.*, 125(10):101102, 2020.
- [119] Gregory Ashton, Kendall Ackley, Ignacio Magaña Hernandez, and Brandon Piotrkowski. Current observations are insufficient to confidently associate the binary black hole merger GW190521 with AGN J124942.3 + 344929. *Class. Quant. Grav.*, 38(23):235004, 2021.
- [120] Johannes Noller and Andrina Nicola. Cosmological parameter constraints for Horndeski scalar-tensor gravity. *Phys. Rev. D*, 99(10):103502, 2019.
- [121] Jose María Ezquiaga. Hearing gravity from the cosmos: GWTC-2 probes general relativity at cosmological scales. *Phys. Lett. B*, 822:136665, 2021.
- [122] Konstantin Leyde, Simone Mastrogiovanni, Danièle A. Steer, Eric Chassande-Mottin, and Christos Karathanasis. Current and future constraints on cosmology and modified gravitational wave friction from binary black holes. *JCAP*, 09:012, 2022.
- [123] Ignacio Magana Hernandez. Constraining the number of spacetime dimensions from GWTC-3 binary black hole mergers. *Phys. Rev. D*, 107(8):084033, 2023.

